



**Impact of Atmospheric CO<sub>2</sub> and Atlantic-Arctic Gateway  
Evolution on Miocene Climate and Ocean Circulation Changes**

By

**Akil Hossain**

**DISSERTATION**

submitted to the University of Bremen  
in accordance with the requirements of the degree of  
DOCTOR OF NATURAL SCIENCES.

Department of Physics  
UNIVERSITY OF BREMEN and  
Alfred-Wegener-Institute for Polar and Marine Research

**Submitted: March 30, 2022**

Reviewers: Prof. Dr. Gerrit Lohmann  
Prof. Dr. Wilfried Jokat

Date of PhD defense: July 13, 2022



## Abstract

The Miocene (23.03–5.33 Ma) was a time period with a warmer climate than today. During this period, changes in ocean gateways and atmospheric CO<sub>2</sub> levels largely control ocean circulation and climate changes. However, the underlying ocean processes and dynamics are poorly understood and it remains a challenge to simulate Miocene climate key characteristics such as pronounced polar warming and a reduced meridional temperature gradient. By applying state-of-the-art fully coupled atmosphere-ocean-sea-ice model approaches Miocene climate conditions at different atmospheric CO<sub>2</sub> concentrations are simulated and thermohaline changes in response to the subsidence of Atlantic-Arctic gateways for various Greenland-Scotland Ridge (GSR) and Fram Strait (FS) configurations are investigated.

For a singular subsidence of the GSR, warming and a salinity increase in the Nordic Seas and the Arctic Ocean is detected. As convection sites shift to the north of Iceland, North Atlantic Deep Water (NADW) is formed at cooler temperatures. The associated deep ocean cooling and upwelling of deep waters to the Southern Ocean surface can cause a cooling in the southern high latitudes. These characteristic responses to the GSR deepening are independent of the FS being shallow or deep. An isolated subsidence or widening of the FS gateway for a deep GSR shows less pronounced warming and salinity increase in the Nordic Seas. Arctic temperatures remain unaltered, but a stronger salinity increase is detected, which further increases the density of NADW. The increase in salinity enhances the contribution of NADW to the abyssal ocean at the expense of the colder southern source water component. These relative changes cause a negligible warming in the upwelling regions of the Southern Ocean. For a sill depth of ~1500 m, ventilation of the Arctic Ocean is achieved due to enhanced import of saline Atlantic water through a FS width of ~105 km. Moreover, at this width and depth, a modern-like three-layer stratification in the Arctic Ocean is detected. The exchange flow through FS is characterized by vertical separation of a low salinity cold outflow from the Arctic Ocean confined to a thin upper layer, an intermediate saline inflow from the Atlantic Ocean below and a cold bottom Arctic outflow. These characteristics are comparable to the present-day hydrography, in spite of significantly shallower and narrower FS configurations during the early Miocene, suggesting that the ventilation mechanisms and stratification in the Arctic Ocean have been similar.

In simulations with different CO<sub>2</sub> levels (280, 450 and 720 ppm) surface temperatures show the best fit to proxy reconstructions for atmospheric CO<sub>2</sub> concentrations of 720 ppm, since in particular the high latitude cooling bias becomes least pronounced. For a CO<sub>2</sub> increase from 280 to 450 ppm polar amplification is simulated in the northern high latitudes, which is stronger than for the same radiative CO<sub>2</sub> forcing from 450 to 720 ppm. At higher CO<sub>2</sub> levels the Miocene climate also shows a reduced climate sensitivity, since the warmest Miocene climate scenario with a CO<sub>2</sub> level of 720 ppm is characterized by a seasonality breakdown in the Arctic Ocean. A pronounced warming in boreal winter is detected for a CO<sub>2</sub> increase from 450 to 720 ppm, in contrast to a moderate boreal summer temperature increase. This change in the seasonal temperature signature is accompanied by a strong sea-ice concentration decline and enhanced moisture availability promotes cloud formation in the summer months. As a consequence the planetary albedo increases and dampens the temperature response to the CO<sub>2</sub> forcing at a warmer Miocene background climate.



# Acknowledgments

Firstly, I would like to thank my supervisor, Dr. Gregor Knorr for his sincere guidance and continuous support throughout my PhD project. His constructive advice, convincing logic on scientific aspects and encouragement always helps me.

I also would like to thank my supervisors Prof. Dr. Gerrit Lohmann and Prof. Dr. Wilfried Jokat for their invaluable academic support and great encouragement throughout my PhD research. Their guidance, suggestions, useful comments help me to structure the thesis work. Their clear and broad perspectives on my research topics guide me into an interesting and enjoyable science world.

Furthermore, I would like to thank my colleagues in the Geophysics group, in particular Prof. Dr. Karsten Gohl, for his supports and Dr. Katharina Hochmuth for providing the bathymetry grid. I would also like to thank my colleagues in the Paleoclimate Dynamics group, in particular Dr. Michael Stärz, Dr. Christian Stepanek, Dr. Paul Gierz, Dr. Christopher Danek, Yuchen Sun and many others for the numerous helps and supports.

Finally, I would like to thank my wife, Dilruba Peya and family, without whose support I probably wouldn't have gotten this far.



# Author's Declaration

I hereby affirm that: (1) I wrote the thesis without the help of others, (2) I used only those sources and aids cited in the text, and (3) All passages taken from the sources used, whether quoted literally or in context, have been indicated as such.

DATE: 29.03.2022, Bremen.

Akil Hossain



# Table of Contents

Abstract.....	iii
Acknowledgments.....	v
Author’s Declaration.....	vii
List of Tables .....	xiii
List of Figures .....	xv
Abbreviation .....	xix
<b>Chapter 1: Introduction .....</b>	<b>1</b>
1.1 Background .....	1
1.2 Effect of Atlantic-Arctic Gateways Opening on Ocean Circulation and Climate .....	4
1.2.1 The relative timing of the Atlantic-Arctic gateways subsidence .....	5
1.3 Impact of Atmospheric CO <sub>2</sub> on Meridional Temperature Changes.....	6
1.4 Scientific Questions .....	7
<b>Chapter 2: Model Description .....</b>	<b>11</b>
2.1 The Climate Model COSMOS.....	11
2.2 AWI Earth System Model (AWI-ESM2.1) .....	12
<b>Chapter 3: Simulated Thermohaline Fingerprints in Response to Different Greenland-Scotland Ridge and Fram Strait Subsidence Histories .....</b>	<b>15</b>
3.1 Model setup and experimental design.....	16
3.2 Results.....	19
3.2.1 Singular effect of GSR deepening for a shallow FS ( $\Delta\text{GSR\_FS}_{\text{shallow}}$ ) .....	19

3.2.2 Singular effect of FS deepening for a deep GSR ( $\Delta FS\_GSR_{deep}$ ) .....	23
3.2.3 Effect of $\Delta GSR\_FS_{deep}$ , $\Delta FS\_GSR_{shallow}$ and $\Delta GSR\_ \Delta FS$ .....	25
3.3 Discussion .....	28
3.3.1 Geological constraints and model scenarios .....	29
3.4 Conclusions of Chapter Three .....	30
3.5 Appendix .....	31
Text S1: Effect of GSR and FS deepening at different sill depths (Sub-scenarios) .....	31

**Chapter 4: Opening of the Fram Strait Led to the Establishment of a Modern-Like Three-Layer Stratification in the Arctic Ocean during the Miocene.....43**

4.1 Model setup and experimental design.....	44
4.2 Results.....	45
4.2.1 Ventilation of the Arctic Ocean .....	45
4.2.2 Stratification in the Arctic Ocean .....	50
4.2.3 Effect of CO <sub>2</sub> concentrations on Arctic Ocean stratification.....	50
4.2.4 Effect of FS widening on the climate .....	53
4.3 Discussion.....	56
4.4 Conclusions of Chapter Four .....	60
4.5 Appendix.....	61

**Chapter 5: The Impact of Different Atmospheric CO<sub>2</sub> Concentrations on Large Scale Miocene Temperature Signatures .....65**

5.1 Model setup and experimental design.....	66
5.1.1 Paleobathymetry and Paleotopography.....	66
5.1.2 Experimental design.....	66
5.2 Results.....	68
5.2.1 Effect of Miocene boundary conditions.....	68
5.2.2 Impact of atmospheric CO <sub>2</sub> and synergetic effects.....	70

5.2.3 Data-model comparison .....	72
5.2.4 Meridional temperature changes at elevated CO <sub>2</sub> concentration .....	76
5.3 Discussion .....	78
5.4 Conclusions of Chapter Five .....	80
5.5 Appendix .....	82
<b>Chapter 6: Summary and Conclusions .....</b>	<b>87</b>
<b>Chapter 7: Outlook .....</b>	<b>93</b>
Bibliography .....	95
Author Contributions .....	111



# List of Tables

Table 1: List of key sensitivity experiments which serve as a basis for key scenarios. ....	17
Table 2: List of key scenarios .....	18
Table 3: List of sensitivity experiments including relevant model parameters. ....	44
Table 4: List of sensitivity experiments including relevant model parameters. ....	68
Table S3.1: List of additional sensitivity experiments.....	40
Table S3.2: List of Sub-scenarios. ....	41
Table S3.3: Key Diagnostics of different model simulations. ....	41
Table S4.1: Key Diagnostics of different model simulations. ....	63
Table S4.2: Compilation of sea surface temperatures of Miocene time interval from marine records in the Arctic Ocean.....	63
Table S5.1: Key Diagnostics of different model simulations. ....	84
Table S5.2: The correlation and RMSE between the simulated annual mean SAT/SST and annual mean Middle Miocene SAT/SST, MCO SST and Late Miocene proxies. ....	84
Table S5.3: The correlation and RMSE between the annual mean SAT of different Early to Middle Miocene simulations and the Middle Miocene annual mean SAT proxy records. ....	85



# List of Figures

Figure 1.1. A compilation of Middle Miocene (~14 Ma) paleobathymetry and paleotopography (in m) in the Northern high latitudes, comprising northern North Atlantic, subpolar Arctic. ...	3
Figure 2.1. (left) ECHAM6 at T63 spectral resolution and (right) FESOM COREII mesh...	12
Figure 2.2. The ocean model FESOM CORE2 mesh resolution (in km) .....	13
Figure 3.1. Global topography/bathymetry reconstruction. ....	16
Figure 3.2. Salinity and ocean velocity maps at the water depths of 50 m. ....	19
Figure 3.3. The effect of $\Delta\text{GSR\_FS}_{\text{shallow}}$ on (a) SST and (b) SSS anomalies. ....	20
Figure 3.4. a) Sea ice concentration changes and b) zonal mean temperature anomalies in the Atlantic Ocean for scenario $\Delta\text{GSR\_FS}_{\text{shallow}}$ . ....	20
Figure 3.5. Evolution of temperature, salinity and density profiles in the Arctic as a consequence of gateways changes. ....	21
Figure 3.6. Ocean velocity at the surface (6 m water depth, m/s). ....	22
Figure 3.7. Change of annual mean wind (m/s) in the Southern Hemisphere for a) $\Delta\text{GSR\_FS}_{\text{shallow}}$ and b) $\Delta\text{FS\_GSR}_{\text{deep}}$ . ....	22
Figure 3.8. Same as Figure 3.3, but for $\Delta\text{FS\_GSR}_{\text{deep}}$ . ....	23
Figure 3.9. Sea ice concentration changes and zonal mean temperature anomalies and zonal mean salinity anomalies in the Atlantic Ocean for $\Delta\text{FS\_GSR}_{\text{deep}}$ . ....	23
Figure 3.10. Atlantic Meridional Overturning Circulation. ....	24
Figure 3.11. Same as Figure 3.3, but for $\Delta\text{GSR\_FS}_{\text{deep}}$ . ....	26
Figure 3.12. Same as Figure 3.3, but for $\Delta\text{FS\_GSR}_{\text{shallow}}$ . ....	26
Figure 3.13. Same as Figure 3.3, but for $\Delta\text{GSR\_}\Delta\text{FS}$ (a, b) and the application of a synergy analysis between gateways changes (c, d). ....	27

Figure S3.1. The effect of (a) $\Delta\text{GSR}_{100\_FS_{\text{shallow}}}$ , (b) $\Delta\text{GSR}_{300\_FS_{\text{shallow}}}$ and (c) $\Delta\text{GSR}_{500\_FS_{\text{shallow}}}$ on SST and SSS anomalies. ....	32
Figure S3.3. The effect of $\Delta\text{FS}_{100\_GSR_{\text{deep}}}$ and $\Delta\text{FS}_{300\_GSR_{\text{deep}}}$ on SST/SSS anomalies. ....	33
Figure S3.3. The effect of (a) $\Delta\text{GSR}_{100\_FS_{\text{deep}}}$ , (b) $\Delta\text{GSR}_{300\_FS_{\text{deep}}}$ and (c) $\Delta\text{GSR}_{500\_FS_{\text{deep}}}$ on SST and SSS anomalies. ....	34
Figure S3.4. The effect of (a) $\Delta\text{FS}_{100\_GSR_{\text{shallow}}}$ , (b) $\Delta\text{FS}_{300\_GSR_{\text{shallow}}}$ and (c) $\Delta\text{FS}_{500\_GSR_{\text{shallow}}}$ on SST and SSS anomalies. ....	35
Figure S3.5 The effect of (a) $\Delta\text{GSR}_{100\_}\Delta\text{FS}_{100}$ , (b) $\Delta\text{GSR}_{300\_}\Delta\text{FS}_{300}$ and (c) $\Delta\text{GSR}_{500\_}\Delta\text{FS}_{500}$ on SST and SSS anomalies. ....	36
Figure S3.6. Annual mean SST for different experiments.....	37
Figure S3.7. Annual mean SSS for different experiments.....	37
Figure S3.8. GSR ocean velocity for different experiments.....	38
Figure S3.9. Fram Strait ocean velocity at 79.5°N for different experiments. ....	39
Figure S3.10. The spin-up trends in temperature and salinity for the deep Atlantic (a, b) and deep Arctic Ocean (c, d) for MIO_450. ....	39
Figure 4.1. Impact of gateway width on vertical salinity characteristics in the Arctic Ocean.	46
Figure 4.2. A cross-section of the Arctic Ocean annual mean temperature. ....	47
Figure 4.3. Ocean velocity at the surface for different experiments.....	48
Figure 4.4. Salinity and ocean velocity (cm/s) at the water depths of 50 m. ....	49
Figure 4.5. A cross-section of the Arctic Ocean annual mean temperature. ....	51
Figure 4.6. Annual mean sea-ice cover for different experiments.....	52
Figure 4.7. The effect of a) $\Delta\text{FW}_{105-50}$ , b) $\Delta\text{FW}_{222-50}$ , c) $\Delta\text{FW}_{286-50}$ , d) $\Delta\text{FW}_{352-50}$ and e) $\Delta\text{FW}_{500-50}$ on SST anomalies.....	53
Figure 4.8. The effect of a) $\Delta\text{FW}_{105-50}$ , b) $\Delta\text{FW}_{222-50}$ , c) $\Delta\text{FW}_{286-50}$ , d) $\Delta\text{FW}_{352-50}$ and e) $\Delta\text{FW}_{500-50}$ on SSS anomalies. ....	54
Figure 4.9. The effect of a) $\Delta\text{FW}_{105-50}$ , b) $\Delta\text{FW}_{222-50}$ , c) $\Delta\text{FW}_{286-50}$ , d) $\Delta\text{FW}_{352-50}$ and e) $\Delta\text{FW}_{500-50}$ on sea ice concentration anomalies (SIC; in K). ....	55

Figure 4.10. Atlantic Meridional Overturning Circulation for different experiments.....	57
Figure S4.1. Ocean velocity at the Fram Strait (79.5°N) for different experiments.....	61
Figure S4.2. A cross-section of the Arctic Ocean annual mean salinity for different experiments.....	62
Figure S4.3. The SST anomalies for CO <sub>2</sub> changes from 280 to 450 ppm.....	62
Figure 5.1. Global compilation of Middle Miocene paleobathymetry and paleotopography..	67
Figure 5.2. Annually averaged differences of a) surface air temperature, b) surface albedo and c) sea ice fraction between the Middle Miocene and the pre-industrial climate state.....	69
Figure 5.3. Application of a synergy analysis between non-CO <sub>2</sub> boundary conditions and atmospheric CO <sub>2</sub> .....	71
Figure 5.4. a) Zonal-annual-mean land surface temperature for all Miocene experiments.....	73
Figure 5.5. The global annual mean SST of different Miocene experiment outputs compared with the Middle Miocene age mean annual terrestrial and sea surface temperature reconstructions.....	74
Figure 5.6. Model fit: Comparison of reconstructed temperature changes of the annual mean Miocene experiment output vs. the Miocene temperature reconstructions.....	75
Figure 5.7. Annual mean SST of MIO_450 compared with reconstructions for the Late Miocene and MCO.....	76
Figure 5.8. The zonal annual, DJF and JJA mean surface temperature change of Miocene experiments (relative to the PI) and zonal annual, DJF and JJA mean sea-ice cover.....	77
Figure 5.9. DJF and JJA mean total cloud cover for the experiments of MIO_720.....	77
Figure 5.10. Summer mean sea-ice cover for different experiments.....	79
Figure S5.1. The timeseries of a) surface air temperature, b) sea surface temperature and c) sea surface salinity for different experiments.....	82
Figure S5.2. Annual mean surface air temperature, sea surface temperature and sea surface salinity for different experiments.....	83
Figure S5.3. Winter and Summer zonal mean total cloud cover for different experiments.....	83
Figure 6.1. Zonal-annual mean SAT for the Miocene at different CO <sub>2</sub> concentrations.....	91



# Abbreviation

<b>Abbreviation</b>	<b>Definition</b>
AABW	Antarctic Bottom Water
AMOC	Atlantic Meridional Overturning Circulation
DJF	December-January-February
EGC	East Greenland Current
ESM	Earth System Model
FS	Fram Strait
GSR	Greenland-Scotland Ridge
IODP	International Ocean Discovery Program
JJA	June-July-August
MCO	Miocene Climatic Optimum
MMCT	Middle Miocene Climatic Transition
NAC	North Atlantic Current
NADW	North Atlantic Deep Water
NH	Northern Hemisphere
NHG	Northern Hemisphere Glaciations
PI	Pre-Industrial
SAT	Surface Air Temperature
SH	Southern Hemisphere
SIC	Sea Ice Concentration
SST	Sea Surface Temperature
SSS	Sea Surface Salinity



Chapter



# Introduction

## 1.1 Background

The Miocene was a time period of global warmth, relative to today. During this time, the configuration of continents, oceans as well as main orographies were only moderately different from those at present. With moderately higher atmospheric CO<sub>2</sub> and higher temperatures, the Miocene, in particular the Miocene Climatic Optimum (MCO; around 16.9–14.7 Ma), has been suggested as a partial analog for the Earth's future greenhouse climate (Steinthorsdottir et al., 2021). Studying this period provides us with unique perspectives that can help to anticipate the impacts and patterns of future warming (Lawrence et al., 2021).

Throughout the Miocene, the general long-term climate trend was characterized by a gradual global cooling, major ice sheet growth, stabilization of Antarctic ice sheets, large-scale regional aridification, the reduction of forests and expansion of grasslands (Bradshaw, 2021). Earth's systems and life forms on land and in the ocean, from the cryosphere to the atmosphere, experienced dynamic changes (Lawrence et al., 2021). The middle Miocene (~15.97–11.63; particularly MCO) was characterized by greenhouse conditions, whereas in the early Miocene (~23.03–15.97 Ma) and late Miocene (~11.63–5.33), extensive glaciations prevailed at high latitudes of the Southern Hemisphere (Steinthorsdottir et al., 2021; Lawrence et al., 2021).

## *1. Introduction*

There is limited evidence for the large ice sheets existence in the higher northern latitudes during the entire Miocene, although isolated glaciers might have been occurred with glaciation intensifying during the late Miocene (Holbourn et al., 2018; Steinhorsdottir et al., 2021). By the late Miocene, various key elements of the Earth System had developed, including strong monsoon systems, the El Niño–Southern Oscillation, perennial Arctic sea-ice, modern-type coral reefs, the tundra-permafrost biome, modern forests with associated ecosystems and widespread grasslands (Lawrence et al., 2021; Steinhorsdottir et al., 2021). However, many of these systems are now considered as vulnerable to forthcoming climate change if typical middle Miocene conditions (temperature/atmospheric CO<sub>2</sub>) recur. It is therefore of huge interest to study this period as a potential future climate analog (Lawrence et al., 2021; Steinhorsdottir et al., 2021).

CO<sub>2</sub> is one of the primary factors influencing climate over geological past, associated with global warming and decreased ice volume (Steinhorsdottir et al., 2021). During the entire Miocene most proxy records reveal that atmospheric CO<sub>2</sub> was near or only moderately higher than preindustrial (PI) values (Beerling & Royer, 2011; Pagani, et al., 2013; Super et al., 2018; Sosdian et al., 2020; Steinhorsdottir et al., 2021). Typical proxy estimates indicate that CO<sub>2</sub> concentrations were in the range of 300–600 ppm during the Miocene (Foster et al., 2017; Sosdian et al., 2018). For the MCO, a similar range of 400–600 ppm has been reported (Royer, 2001; K rschner et al., 2008; Beerling et al., 2009; Steinhorsdottir et al., 2021), although some reconstructions suggest that CO<sub>2</sub> levels may have been up to 1,100 ppm (Sosdian et al., 2018; Stoll et al., 2019).

Previous modeling studies targeting the Miocene suggest a substantial high-latitude (> 60 °N and 60 °S) warming (~0–18 °C in the Northern Hemisphere; NH and ~0–38 °C in the Southern Hemisphere; SH), while the temperature increase in the tropics (~0–8 °C) is less pronounced (Burls et al., 2021). During the MCO, different proxy reconstructions suggest that SSTs were ~10–15 °C warmer in the high latitudes of the NH (Super et al., 2020) and ~8–10 °C warmer than PI in the SH (Shevenell et al., 2004), leading to a global mean surface warming of ~7.6–2.3 °C compared to PI (Goldner et al., 2014). Furthermore, a meridional temperature gradient of ~17 °C during Miocene is estimated by Goldner et al. (2014). The polar amplified warming is a robust feature and therefore the meridional temperature gradient is weaker during the Miocene than today (Knorr et al., 2011; Burls et al., 2021).

Furthermore, several modelling studies have explored the role of different potential mechanisms on the climate of the Miocene. The global temperature and climatic changes are

believed to have been primarily related to increased CO<sub>2</sub> concentrations, paleogeographic changes (including bathymetry, orography and ocean gateways; Mikolajewicz and Crowley 1997; von der Heydt and Dijkstra, 2006; Micheels et al., 2009; Hossain et al., 2020; 2021), changes in the vegetation (Bradshaw et al., 2015; Knorr et al., 2011) and the sea ice-albedo feedback mechanism. The radiative forcing including an atmospheric CO<sub>2</sub> doubling reveals a potentially dominant control on global-scale temperature changes (Steinthorsdottir et al., 2021). Miocene boundary conditions (paleogeography and ice sheets) other than CO<sub>2</sub> can raise the mean global temperature by ~2 °C (Burls et al., 2021). On the other hand, the vegetation and paleogeographic variations together caused a +1.5 °C warming (Herold et al., 2011) during the Middle Miocene. Higher atmospheric CO<sub>2</sub> and more effective ocean mixing could have contributed to a reduced summer-to-winter range of temperature (Valdes et al., 1996; Spicer et al. 2004). While these mechanisms have been identified to enable warmer temperatures in the models, it is still difficult to reconcile the Miocene polar amplified warmth observed in the proxy data with the simulations (Steinthorsdottir et al., 2021; Burls et al., 2021).

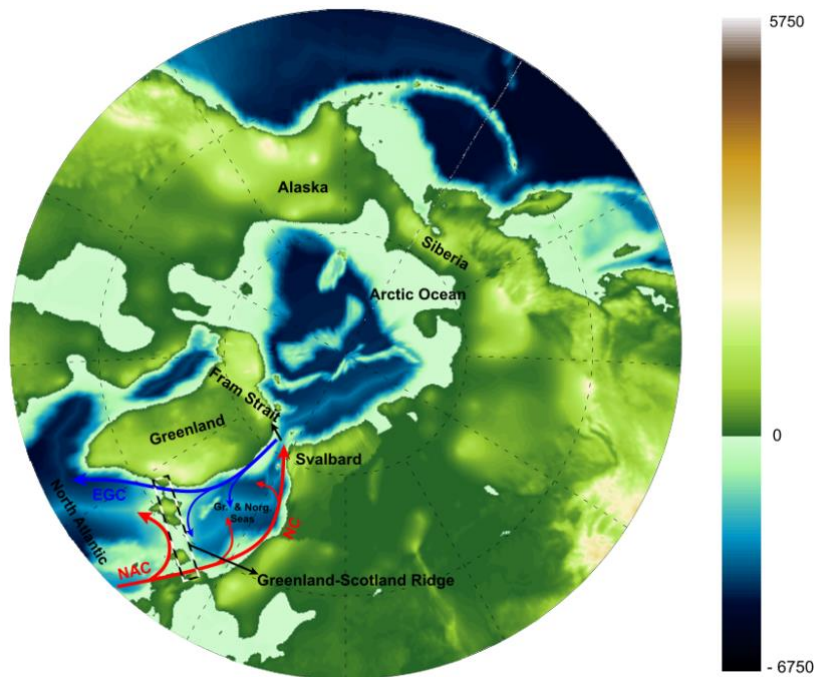


**Figure 1.1:** A compilation of Middle Miocene (~14 Ma) paleobathymetry and paleotopography (in m; Straume et al., 2020) in the Northern high latitudes, comprising the northern North Atlantic, subpolar Arctic (Greenland and Norwegian Seas) and the Eurasian Basin in the Arctic Ocean. The schematic circulation shows pathways of the North Atlantic Current (NAC), the Norwegian Current (NC) and the East Greenland Current (EGC).

## *1. Introduction*

Tectonics played a vital role in shaping the Miocene climate, with mountain building occurring in many regions, a more southward Australia and key ocean gateways restricting or opening up (Bradshaw, 2021). During this time, several ocean gateways were gradually closing such as Tethys Gateway (connected the Atlantic and Indian oceans), Indonesian Seaway (connected the Pacific and Indian oceans), and the Panama Gateway (connected the Atlantic and Pacific oceans), whilst the Drake Passage (located between South America and Antarctica) and the Atlantic-Arctic gateways were opening up (Steinthorsdottir et al., 2021). Changes in ocean gateway geometry play a key role in global climate evolution and oceanic circulation (Haug and Tiedemann, 1998; Bartoli et al., 2005; Elsworth et al., 2017; Stürz et al., 2017). The formation of Atlantic-Arctic gateways (i.e., Fram Strait, Greenland-Scotland Ridge) drives northward directed oceanic heat transport (Stürz et al., 2017).

## **1.2 Effect of Atlantic-Arctic Gateways Opening on Ocean Circulation and Climate**

The geometrical widening/subsidence of the northern gateway configuration drove water-mass and large-scale circulation changes (Wright and Miller, 1996; Jakobsson et al., 2007). In this context a threshold in ocean gateway depth, that is linked to the effect of wind mixing (Stürz et al., 2017), is an important parameter. Intensive glaciations at the Earth's polar region during the Cenozoic (65 Myr ago to present) have been linked to the opening of the ocean gateways (Knies and Gaina 2008). In the critical time period during Oligocene/Miocene transition, Fram Strait (FS), located between Svalbard and Greenland, was the only deep-water connection of the Arctic with the World Oceans (Ehlers and Jokat, 2013; von Appen et al., 2015). Consequently, the continuous opening of the FS played a crucial role in ocean dynamics of the Arctic Ocean and therefore in the evolution of the northern polar region (Jakobsson et al., 2007; Ehlers and Jokat, 2013; Jokat et al., 2016). This also likely caused an intensification of the North Atlantic thermohaline circulation (Knies et al., 2014). The ventilation of the Arctic Ocean was established with the opening of FS to a critical width (about 40-50 km) that allowed entrance of saline Atlantic waters to the Arctic and supplied oxygen to intermediate/deep waters (Jakobsson et al., 2007). However, further south of the FS, the Greenland-Scotland Ridge (GSR), extends from Greenland to Scotland through Iceland, constitutes an ocean gateway between the Atlantic Ocean and the Nordic Seas (located between FS and GSR)

(Wright and Miller, 1996; Thiede and Myhre, 1996; Davies et al., 2001; Via and Thomas, 2006; Stärz et al., 2017). The subsidence of the GSR sill depth deeper than the wind mixed layer (~50 m) strengthens the entrainment of Atlantic waters and a bi-directional circulation across the ridge develops, creating a baseline for the final establishment of a modern prototype current system (Stärz et al., 2017). The formation of NADW releases heat to the atmosphere in the northern high latitudes (Broecker and Denton, 1989; Wright and Miller, 1996) and the progressive subsidence of GSR during the Miocene allowed increased export of NADW to the abyssal Ocean (Poore et al., 2006; Knies et al., 2014). Transformation of these water-masses associated with mixing and upwelling to the Southern Ocean surface is a key source of heat for summer sea ice melting around Antarctica (Gordon, 1981; Wright and Miller, 1996). Hence, changes in the relative timing of the North Atlantic gateway configuration are not only a key control for North Atlantic and Arctic environmental conditions, but also bear the potential to have far field bi-polar impacts.

### **1.2.1 The relative timing of the Atlantic-Arctic gateways subsidence**

The relative timing of the subsidence of gateways between the Arctic Ocean and the northern North Atlantic, providing deep-water exchange and ventilation of the Arctic Ocean, has been poorly constrained by scientific drilling. Only few data exist to describe the subsidence of the GSR in great detail. Before initial GSR subsidence (~36 Ma), lagoonal circulation in the Nordic Seas restricted export of polar freshwater towards the Atlantic (DSDP site 336; Talwani and Udintsev, 1976). Subsequently, drill samples indicate a progressive deepening of GSR around 36–31 Ma, which creates a semi-enclosed estuarine gateway exchange and brackish saline Nordic Seas. Around 20–24 Ma, the GSR sill is well below sea level and the wind-induced mixed layer establishing northward directed warm North Atlantic Current flowing to the east of Nordic Seas and a southward cold East Greenland Current to the west (Orvic and Niiler, 2002; Stärz et al., 2017). A paleo-bathymetric model shows that the first possibility for a deep-water exchange between the North Atlantic and the Nordic Seas through GSR could have been between 15 and 20 Ma (Ehlers and Jokat, 2013). The large knowledge gaps on the GSR subsidence, which formed by excess magma production of the Iceland plume, can only be filled by additional scientific drilling along the ridge. Standard subsidence models typical for oceanic crust cannot be applied. Plume pulsations, which might have caused a temporary uplift and/or slowed down the GSR subsidence, cannot be excluded.

## *1. Introduction*

The situation in the Fram Strait is different. It formed by seafloor spreading between Greenland and Svalbard. The timing for the opening of FS is much better constrained by geophysical data. Extensive seismic and magnetic data indicate that the FS was likely a shallow and narrow gateway close to 21 Ma (Jokat et al., 2016). Further, scientific drilling in the central Arctic indicates that the evolution of a poorly ventilated and land-locked sea to a ventilated Arctic Ocean initiated latest at ~18 Ma (Jakobsson et al., 2007; Ehlers and Jokat, 2013). The early Miocene opening of FS (Ehlers and Jokat, 2013; Jokat et al., 2016) allowed an increased water mass exchange between the Atlantic Ocean and the Arctic Ocean, with significant climatic impacts that strongly influenced the paleoceanographic conditions in the Arctic Ocean (Thompson et al., 2012), and likely caused enhanced contribution of the North Atlantic thermohaline circulation (Knies et al., 2014). During this period, saline Atlantic waters entered to the Arctic and supplied oxygen to intermediate/deep waters transforming the Arctic Ocean from a restricted to a fully ventilated Ocean at around 17.5 Ma (Jakobsson et al., 2007). Since then, the exchange of cold Arctic water and warm Atlantic water has been possible (Jakobsson et al., 2007). However, it remains a challenge to better constrain the relative timing, depth and width of both northern gateways in order to understand their potential climatic responses.

### **1.3 Impact of Atmospheric CO<sub>2</sub> on Meridional Temperature Changes**

During the Miocene, different proxy reconstructions estimate pronounced warming at high latitudes relative to today. In contrast, numerical simulations indicate lower high-latitudes and higher tropical temperatures than the proxies (Huber & Caballero, 2011; Knorr et al., 2011; Burls et al., 2021; Lohmann et al., 2022). However, the driving forces behind Miocene warm climate and its fluctuations remain ambiguous. Different modelling approaches simulated the Miocene climate at different atmospheric CO<sub>2</sub> concentrations (between 200 and 800 ppm; Huang et al. 2017; Knorr & Lohmann, 2014; Stärrz et al., 2017; Burls et al., 2021) but generally have difficulties to simulate the observed pronounced polar warmth at reconstructed Miocene CO<sub>2</sub> concentrations (typically 300–600 ppm; Burls et al., 2021). The weakening of the meridional temperature gradient and degree of polar amplified warming increases in the simulations with higher CO<sub>2</sub> levels (Burls et al., 2021).

Our understanding of Miocene climatic, oceanic, and biogeochemical changes on broad temporal and spatial scales is still developing. By comparing climate reconstructions from chemical and fossil data to Miocene climate simulations, we are able to test our understanding of the global climate under warmer conditions and higher atmospheric CO<sub>2</sub> than those of today. A recent study by Steinthorsdottir et al. (2021) reviewed the state-of-the-art in Miocene climate, ice sheet dynamics, ocean circulation and biogeochemical cycling as inferred through modeling studies and proxy observations. Burls et al. (2021) assesses the current range of model-data agreement and current advancement toward simulating Miocene warmth. Another recent study by Lohmann et al. (2022) reveals that, relatively moderate CO<sub>2</sub> levels (450 ppm) with enhanced ocean mixing can contribute to much warmer high latitudes and enable meridional temperature characteristics representative of MCO reconstructions. They find a moderate low-latitude and pronounced high-latitude warming in their numerical simulations. However, it remains a major challenge to successfully simulate the Miocene high-latitudes with fully coupled ocean-atmosphere model (Burls et al., 2021).

Using the mostly published atmospheric CO<sub>2</sub> level during the Miocene, no climate model experiment has so far reproduced the elevated proxy paleo temperatures (Steinthorsdottir et al., 2021). The model simulations cannot capture the full extent of the midlatitude and polar warmth of the Miocene and meridional temperature gradient observed in the proxies (Goldner et al., 2014; Burls et al., 2021). It is obvious that our understanding of important physical parameters or positive feedbacks is incomplete to explain the processes, which maintained the much weaker than PI equator-to-pole temperature difference.

### **1.4 Scientific Questions**

Based on this current knowledge, the following four key questions will be addressed in this thesis:

1. What are the thermohaline responses to the subsidence of Greenland-Scotland Ridge and Fram Strait during early to middle Miocene? (Chapter 3)
2. What are the minimum depth and width of Fram Strait that is required for ventilation of the Arctic Ocean? (Chapter 4)
3. How did the opening of the Fram Strait during early-to-middle Miocene influence the global ocean circulation/current system? (Chapter 4)

## *1. Introduction*

4. What are the impacts of atmospheric CO<sub>2</sub> changes on large scale Miocene temperature changes? To what extent can a climate model reproduce the temperature signals that are acquired from proxy records? (Chapter 5)

To answer these research questions, this thesis is organized as follows. In **Chapter Two**, the climate model applied for the studies is presented. **Chapter Three** is aimed to investigate the simulated thermohaline changes in response to the subsidence of Greenland-Scotland Ridge and Fram Strait during early to middle Miocene. In the numerical experiments, Miocene (~23–15 Ma) background climate conditions are applied (Stärz et al., 2017), as a basis and different GSR and FS sill depths representing different possible tectonic configurations during the early to middle Miocene are used. Based on tectonic constraints the most likely scenarios to provide fingerprints of characteristic thermohaline changes are interpreted. Thereafter, the stratification and ocean circulation in the Arctic Ocean in response to the opening of the FS during early to middle Miocene is presented in **Chapter Four**. The model simulation applies a Miocene-bathymetric reconstruction (Ehlers and Jokat, 2013), which is believed to capture the major bathymetric features, such as different sub-basins and sills. Furthermore, CO<sub>2</sub> changes are used relative to early-middle Miocene (about 23–15 Ma) boundary conditions. In the numerical experiments, several different opening geometries for the FS are investigated to constrain the regional and global climate impacts of this tectonic event. Subsequently, in **Chapter Five**, the impact of different atmospheric CO<sub>2</sub> concentrations on large scale Miocene temperature signatures is discussed. In these model simulations a high-resolution global Miocene bathymetric and topographic reconstruction (Paxman et al., 2019; Hochmuth et al., 2020a; Straume et al., 2020) is used, which captures major paleobathymetric features (such as ocean ridges, plateaus and margins) and mountain ranges in the paleotopography of the continents (e.g., the Andes). The simulated surface temperatures are compared against available proxy data estimates. Finally, common lessons learned and an overarching summary are presented in the summary and conclusions section in **Chapter Six**, which is complemented by an outlook in **Chapter Seven**. Chapters three, four and five are based on the following studies that have been either published (Hossain et al., 2020; 2021) or submitted (Hossain et al., 2022):

**Chapter 3:**

Hossain, A., Knorr, G., Lohmann, G., Stürz, M., & Jokat, W., (2020). Simulated thermohaline fingerprints in response to different Greenland-Scotland Ridge and Fram Strait subsidence histories. *Paleoceanography and Paleoclimatology*, 35(7), p.e2019PA003842. <https://doi.org/10.1029/2019PA003842>

**Chapter 4:**

Hossain, A., Knorr, G., Jokat, W., & Lohmann, G. (2021). Opening of the Fram Strait led to the establishment of a modern-like three-layer stratification in the Arctic Ocean during the Miocene. *arktos*, 1-12. <https://doi.org/10.1007/s41063-020-00079-8>

**Chapter 5:**

Hossain, A., Knorr, G., Jokat, W., Lohmann, G., Hochmuth, K., Gierz, P., & Gohl, K. (2022). The impact of different atmospheric CO<sub>2</sub> concentrations on large scale Miocene temperature signatures. *Paleoceanography and Paleoclimatology*, in revision.

Additionally, one further co-author publication has been published:

Lohmann, G., Knorr, G., Hossain, A. & Stepanek, C. (2022). Effects of CO<sub>2</sub> and ocean mixing on Miocene and Pliocene temperature gradients, *Paleoceanography and Paleoclimatology*, 35(7), <https://doi.org/10.1029/2020PA003953>.

## *1. Introduction*

Chapter  2

## Model Description

### 2.1 The Climate Model COSMOS

In this study (Chapter 3 and 4) the fully coupled Earth System Model COSMOS is used, which includes the atmosphere model ECHAM5 (Roeckner et al., 2003), the land-vegetation model JSBACH (Raddatz et al., 2007) and the ocean model MPI-OM (Marsland et al., 2003). The atmosphere model is used at T31 spherical horizontal resolution ( $\sim 3.75^\circ \times 3.75^\circ$ ) with 19 vertical layers. The land-vegetation model runs at the same horizontal resolution as the atmosphere model. The ocean model is resolved at 40 uneven vertical layers and has a resolution of GR30 ( $3^\circ \times 1.8^\circ$ ). The spatial resolution increases to  $\sim 30$  km towards the grid poles at Antarctica and Greenland. Such a better resolution close to the grid poles enhances the representation of physical processes for the deep-water formation in Nordic, Labrador and Weddell seas. The model dynamics are solved on a curvilinear Arakawa C-grid. The MPI-OM includes a Hibler-type dynamic-thermodynamic sea-ice model. The interactive exchange of fluxes of energy, momentum and mass between ocean and atmosphere is performed via the coupler OASIS3 (Jungclaus et al., 2006). The climate model has already been applied for scientific questions focusing on the last millennium (Jungclaus et al., 2010), the Holocene (Wei and Lohmann, 2012; Lohmann et al., 2013; Starz et al., 2016), the Last Glacial Maximum

## 2. Model Description

(Gong et al., 2013; Zhang et al., 2013; Starz et al., 2016), the Pliocene (Stepanek and Lohmann, 2012) and the Miocene (Knorr et al., 2011; Knorr and Lohmann, 2014; Stein et al., 2016; Huang et al., 2017; Starz et al., 2017, Hossain et al., 2020; 2021; Lohmann et al., 2022).

### 2.2 AWI Earth System Model (AWI-ESM2.1)

In Chapter 5, the AWI Earth System Model (AWI-ESM2.1) is applied, which consists of the atmosphere model ECHAM6 (version 6.3.05p2-concurrent\_radiation-paleodyn; Stevens et al., 2013), the land-vegetation model JSBACH (Raddatz et al., 2007) and the ocean model FESOM2 (version 2.0; Danilov et al. 2017; Scholz et al., 2019; Sidorenko et al., 2019). The coupling between ECHAM6 and FESOM2 is achieved via the OASIS3-MCT coupler (Valcke, 2013). AWI-ESM2.1 is based on the AWI Climate Model (AWI-CM) with the finite-volume formulation of FESOM2 (Danilov et al. 2017; Sidorenko et al., 2019). ECHAM6 is used at T63 spectral resolution ( $\sim 1.88^\circ \times 1.88^\circ$ ;  $\sim 180$  km horizontal resolution at the equator) with 47 vertical layers. JSBACH runs at the same horizontal resolution as ECHAM6. FESOM2 employs the COREII mesh or one of the paleo-derivates of COREII. The grid resolution for FESOM2 is high in critical areas (up to  $\sim 20$  km) where small scale processes influence ocean dynamics.

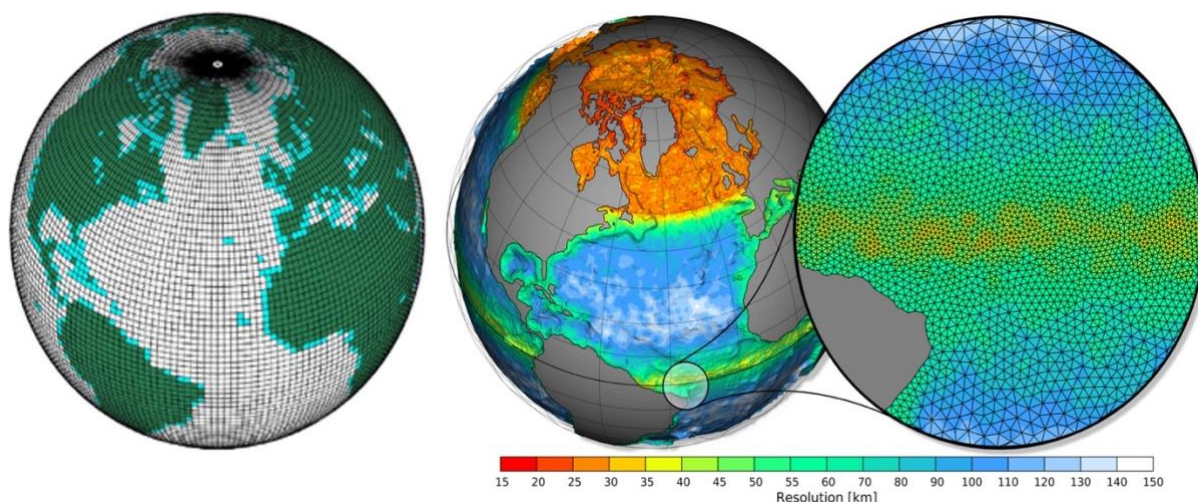


**Figure 2.1.** (left) ECHAM6 at T63 spectral resolution and (right) FESOM COREII mesh. Dark green regions of the T63 grid represent the area with more than 50% land fraction where areas with a land fraction less than 50% shown in light green (taken from Sidorenko et al., 2015).

## 2. Model Description

AWI-ESM2.1 includes JSBACH with interactive vegetation dynamics, which ensures that vegetation and climate are consistent with each other. The ocean communicates its surface state to the atmosphere and is driven by the atmospheric fluxes. Four ocean fields are sent to ECHAM6: sea ice concentration, sea ice thickness (SIT), sea surface temperature (SST), and snow on sea ice. ECHAM6 computes 12 air-sea fluxes (e.g., heat, momentum, freshwater fluxes) based on surface fields provided by FESOM2. The model AWI-ESM2 has been validated under modern climate conditions (Sidorenko et al., 2019) and has been applied for marine radiocarbon concentrations (Lohmann et al., 2020), the latest Holocene (Vorrath et al., 2020), the Last Interglacial (Otto-Bliesner et al., 2021) and the Last Glacial Maximum (Kageyama et al., 2021).

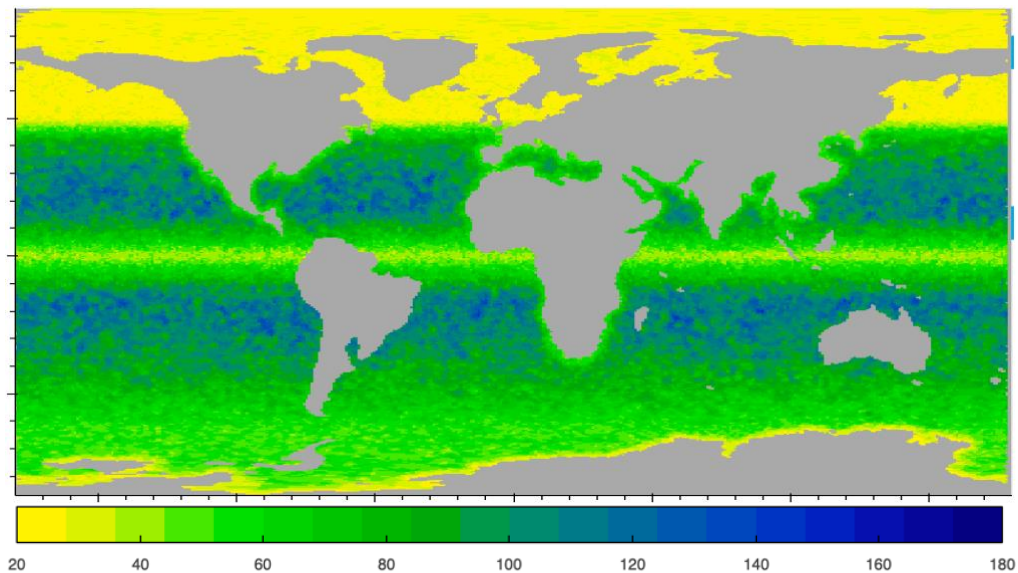


**Figure 2.2.** The ocean model FESOM CORE2 mesh resolution (in km).

### *3. Simulated Thermohaline Fingerprints*

Chapter  3

## Simulated Thermohaline Fingerprints in Response to Different Greenland-Scotland Ridge and Fram Strait Subsidence Histories

In this chapter several different cases for the relative subsidence of both the GSR and the FS are investigated. In the numerical experiments, the fully coupled atmosphere-ocean-sea ice model COSMOS is used to explore singular and combined effects of both gateways on ocean circulation and climate during a time interval between ~35 and 15 Ma. In the sensitivity studies, Miocene (~23–15 Ma) background climate conditions (Stärz et al., 2017) is applied, as a basis and use different GSR and FS sill depths representing different possible tectonic configurations during the early to middle Miocene. Based on tectonic constraints this study interpret which scenarios are the most likely ones to provide fingerprints of characteristic thermohaline changes.

*Declaration: this chapter was published in Hossain et al. (2020).*

### 3. Simulated Thermohaline Fingerprints

#### 3.1 Model setup and experimental design

The model setup is based on early to middle Miocene time period (~23–15 Ma) including orography, paleobathymetry, and ice sheet adjustments of Herold et al. (2008). Additionally, a regional high-resolution bathymetric reconstruction comprising the North Atlantic/Arctic Ocean (Ehlers and Jokat, 2013) is implemented in our approach. The original model setup of Stärz et al. (2017) is further refined by including a more realistic regional Weddell Sea bathymetry reconstruction in the Southern Ocean (Huang et al., 2017) (Figure 3.1). The ocean grid cells representing the Barents Sea region have been transferred to land cells. This assumption is in better agreement with geological data (Butt et al., 2002). Therefore, the FS represents a single gateway control towards the Arctic Ocean. Other ocean gateways like the Barents Sea, Canadian Archipelago and Bering Strait evolved after the middle Miocene. Furthermore, the Panama Seaway and Tethys still connect the ocean basins. In general the elevation of the Antarctic ice-sheet and the Miocene orography (Rocky Mountains, Tibetan Plateau, Andes, East Africa) are reduced compared to Pre-Industrial (PI) times, whereas the Greenland ice-sheet is absent in our Miocene setup.

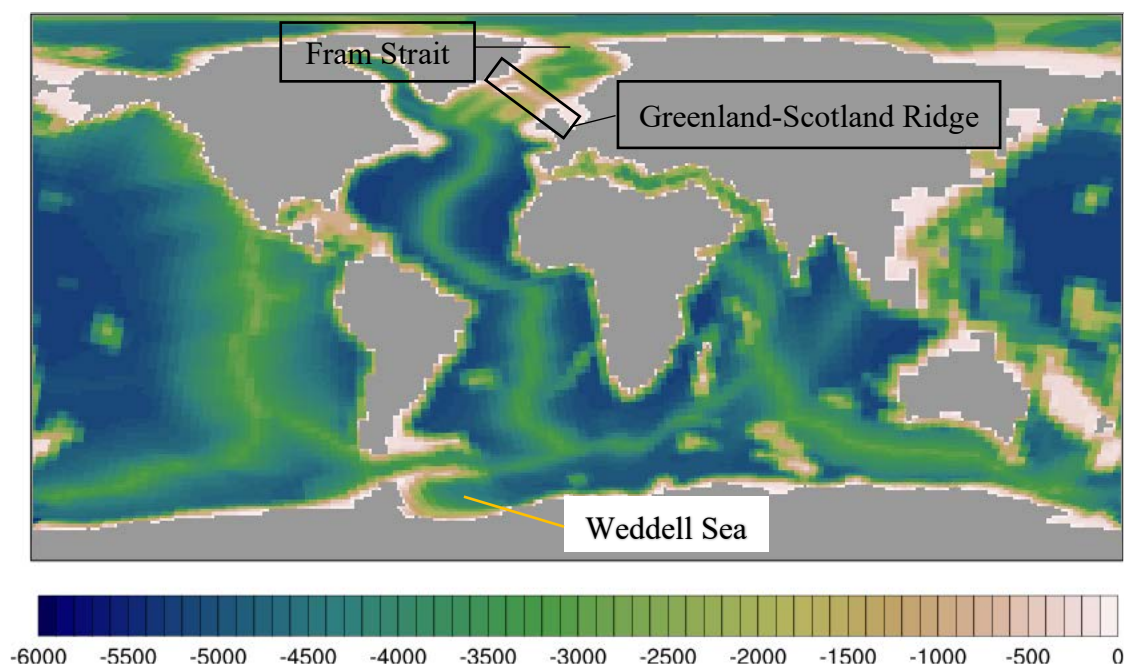


**Figure 3.1.** Global topography/bathymetry reconstruction (in m) (Herold et al., 2008) which is improved by high resolution bathymetry reconstructions comprising the Arctic/North Atlantic sector for 15 Ma (Ehlers and Jokat, 2013) and the Weddell Sea embayment for 15 Ma (Huang et al., 2014).

### 3. Simulated Thermohaline Fingerprints

In our reference simulation (MIO\_450) we prescribe an atmospheric CO<sub>2</sub> level of 450 ppm and both gateways are fully developed (GSR depth: ~960 m; width: ~1300 km and FS depth: ~2500 m; width: ~500 km, Table 1). The ocean gateways are wide enough to maintain rotationally controlled exchange flows across the gateways (Pratt and Spall 2008). We integrate the model for 4 kyrs to minimize temperature/salinity trends in the deep ocean (Figures S3.10) after initialisation of the ocean from present day conditions (Figures S3.6–S3.7). Based on this experiment the ocean gateway sensitivity experiments are performed at various height dimensions of the GSR and FS. A list of our key model experiments including relevant model characteristics are summarized in Table 1. After model integration of at least 2 kyrs, a climatological period of the final 100 yrs of model simulation is used for analysis.

**Table 1:** List of key sensitivity experiments which serve as a basis for key scenarios (listed in Table 2) but a set of 14 additional sensitivity experiments have been performed to collaborate our result are listed in Table S3.1.

Model Exp.	Fram Strait width (km)	Fram Strait depth (m)	GSR depth (m)	Atmos. CO <sub>2</sub> (ppm)	Length of simulation (kyrs)
MIO_450	~500 km	~2,500 m	~960 m	450	3.3
MIO_FS50	~500 km	50 m	~960 m	450	2.0
MIO_GSR40	~500 km	~2,500 m	40 m	450	2.0
MIO_FS50_GSR40	~500 km	50 m	40 m	450	2.0
PI	~670 km	~2,800 m	~1,100 m	280	5.9

A previous study by Starz et al. (2017) investigated the singular effect of GSR subsidence for a deep (~2500 m depth) and wide (~500 km) Fram Strait. They found a non-linear impact of sill depth on the Arctic Ocean circulation and water mass exchange that is mainly driven by the effect of gateway depth on mixed layer characteristics. In our study we apply different GSR and FS states as a representative for different tectonic settings that occur during the subsidence interval to explore singular/combined effects of both gateways on ocean circulation and climate ~35 and 15 Ma. For this study a shallow GSR means that it was subaerial or close to the surface (< 40 mbsl) for its entire length.

In comparison to PI, a stronger surface circulation is driven by more direct wind forcing due to a non-permanent (seasonal) sea ice cover and stronger stratification (baroclinic-geostrophic forcing) in the Arctic Ocean. From a Northern Hemisphere perspective these characteristics in

### 3. Simulated Thermohaline Fingerprints

MIO\_450 are similar to the modelled Miocene changes in Starz et al. (2017), although the Barents Sea region is subaerially exposed in our set-up. However, based on the implementation of an improved Weddell Sea bathymetry (Huang et al., 2014) there are fundamental changes in AABW formation. In particular the southerly placed shelf-break in the Weddell Sea causes an increase of AABW formation and enhanced gyre transport in the Southern Ocean in accordance with Huang et al. (2017).

Using a set of four key model simulations (Table 1), we examine the isolated impacts of the GSR and FS subsidence by changing the sill depth, starting from a shallow depth towards a deep Miocene bathymetric configuration. The different model scenarios are specified in Table 2 and the analysis is supported by fourteen additional sensitivity experiments (Table S3.1). In  $\Delta\text{GSR\_FS}_{\text{shallow}}$ , we consider a subsidence of GSR gateway depth from 40 to  $\sim 960$  mbsl when FS sill depth is shallow (50 mbsl) and in scenario  $\Delta\text{GSR\_FS}_{\text{deep}}$  the GSR is deepened to  $\sim 960$  mbsl for a deep FS sill ( $\sim 2500$  mbsl) to analyse the singular effect of GSR gateway subsidence. On the other hand, both model scenarios  $\Delta\text{FS\_GSR}_{\text{shallow}}$  and  $\Delta\text{FS\_GSR}_{\text{deep}}$  are characterized by subsidence of FS from 50 to  $\sim 2500$  mbsl for a shallow (40 mbsl)/deep ( $\sim 960$  mbsl) GSR sill to investigate the singular effect of FS gateway deepening. In an additional model scenario ( $\Delta\text{FS\_}\Delta\text{GSR}$ ), the FS is deepened from 50 mbsl to  $\sim 2500$  mbsl in parallel with the GSR that is deepened from 40 mbsl to  $\sim 960$  mbsl in order to test potential interaction and feedbacks between both gateways. To analyse the climate responses due to the relative timing of the subsidence histories of both ocean gateways, we primarily focus on the temperature/salinity changes.

**Table 2:** List of key scenarios

Title	Anomaly of experiments	GSR depth change (m)	FS depth change (m)
$\Delta\text{GSR\_FS}_{\text{shallow}}$	MIO_FS50 – MIO_FS50_GSR40	$\sim 960 - 40$	50
$\Delta\text{GSR\_FS}_{\text{deep}}$	MIO_450 – MIO_GSR40	$\sim 960 - 40$	$\sim 2500$
$\Delta\text{FS\_GSR}_{\text{shallow}}$	MIO_GSR40 – MIO_FS50_GSR40	40	$\sim 2500 - 50$
$\Delta\text{FS\_GSR}_{\text{deep}}$	MIO_450 – MIO_FS50	$\sim 960$	$\sim 2500 - 50$
$\Delta\text{GSR\_}\Delta\text{FS}$	MIO_450 – MIO_FS50_GSR40	$\sim 960 - 40$	$\sim 2500 - 50$

## 3.2 Results

### 3.2.1 Singular effect of GSR deepening for a shallow FS ( $\Delta\text{GSR\_FS}_{\text{shallow}}$ )

A singular subsidence of GSR from 40 mbsl towards a deep gateway configuration of  $\sim 960$  mbsl for a shallow FS ( $\Delta\text{GSR\_FS}_{\text{shallow}}$ ) enhances the entrance of Atlantic waters to the Nordic Seas (Figure 3.2a and 3.2b). In parallel with GSR subsidence, the corresponding salt water exchange across the gateway largely controls the overall salinity increase at the ocean surface in both the Nordic Seas and the Arctic Ocean (Figure 3.3b). We observe a cooling and unchanged salinity conditions south of Iceland. As more cold water from the polar and sub-polar Arctic is advected southward, the overflow and the deep water south of Iceland becomes cooler (up to  $-2$  °C).

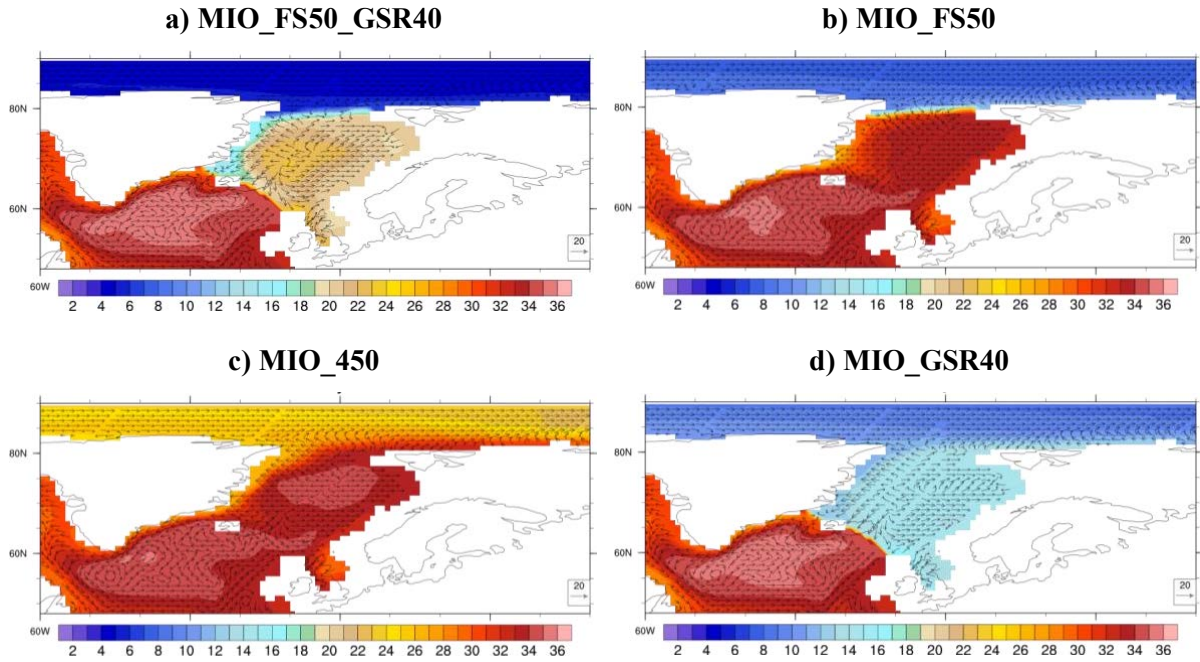


**Figure 3.2.** Salinity (in psu) and ocean velocity (cm/s) maps at the water depths of 50 m for the experiments of (a) *MIO\_FS50\_GSR40*, (b) *MIO\_FS50*, (c) *MIO\_450* and (d) *MIO\_GSR40*.

In the Nordic Seas a warming (up to  $+7$  °C) in combination with reduced sea-ice cover and a salinity increase (up to  $+14$  psu) is simulated as the GSR subsides. In the Arctic Ocean a salinity increase (up to  $+4$  psu) (Figure 3.3) and warming in sub-surface water (between 100 to 1000 m; up to  $+2$  °C) linked with reduced sea ice extent is detected (Figures 3.4 and 3.5). The convection sites shift to the north off Iceland. Therefore, deep water formation takes place at cooler temperatures. Across the GSR, relatively saline and warm water is transported north-

### 3. Simulated Thermohaline Fingerprints

eastwards in the near-surface/sub-surface layers (upper ~500 m), while cold but fresher water from the Arctic returns south-westwards (surface to bottom layers) along the Greenland coast and south-eastwards at deeper layers (below ~500 m) (Figures 3.2a, 3.2b and 3.6; Figures S3.8a, and S3.8b). This deep overflow of dense, cold-water results from newly established deep-water formation sites north of Iceland. Due to enhanced inflow of salty waters and enhanced freshwater export of Arctic origin across the GSR, the Arctic Ocean starts to become more saline. Nevertheless, there is a pronounced salinity difference between the Nordic Seas and the Arctic Ocean due to the restricted exchange across a shallow FS gateway.

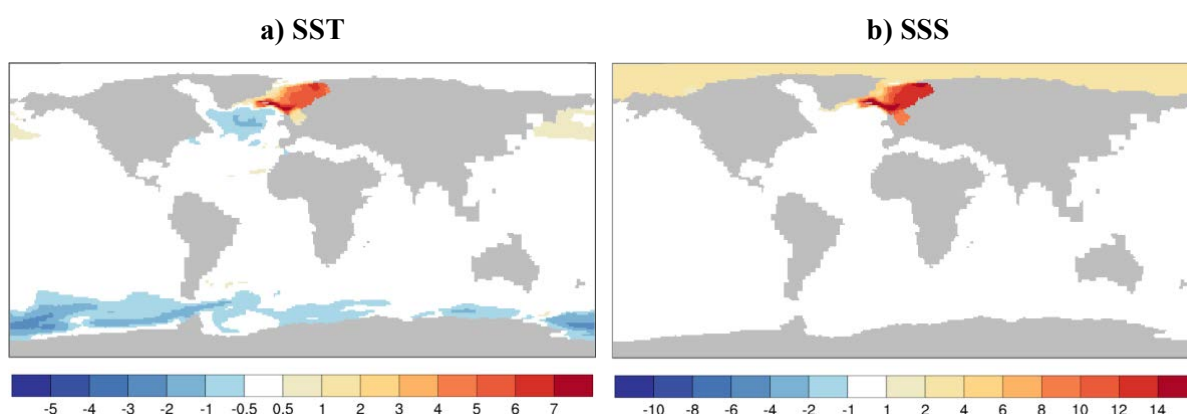


**Figure 3.3.** The effect of  $\Delta GSR\_FS_{shallow}$  on (a) sea surface temperature anomalies (SST; in  $^{\circ}C$ ) and (b) sea surface salinity anomalies (SSS; in psu).

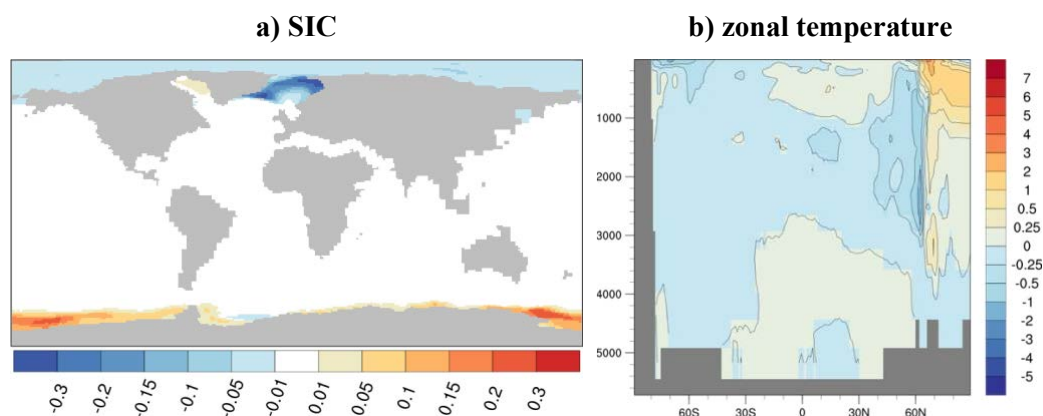


**Figure 3.4.** a) Sea ice concentration changes and b) zonal mean temperature anomalies (in  $^{\circ}C$ ) in the Atlantic Ocean for scenario  $\Delta GSR\_FS_{shallow}$ .

### 3. Simulated Thermohaline Fingerprints

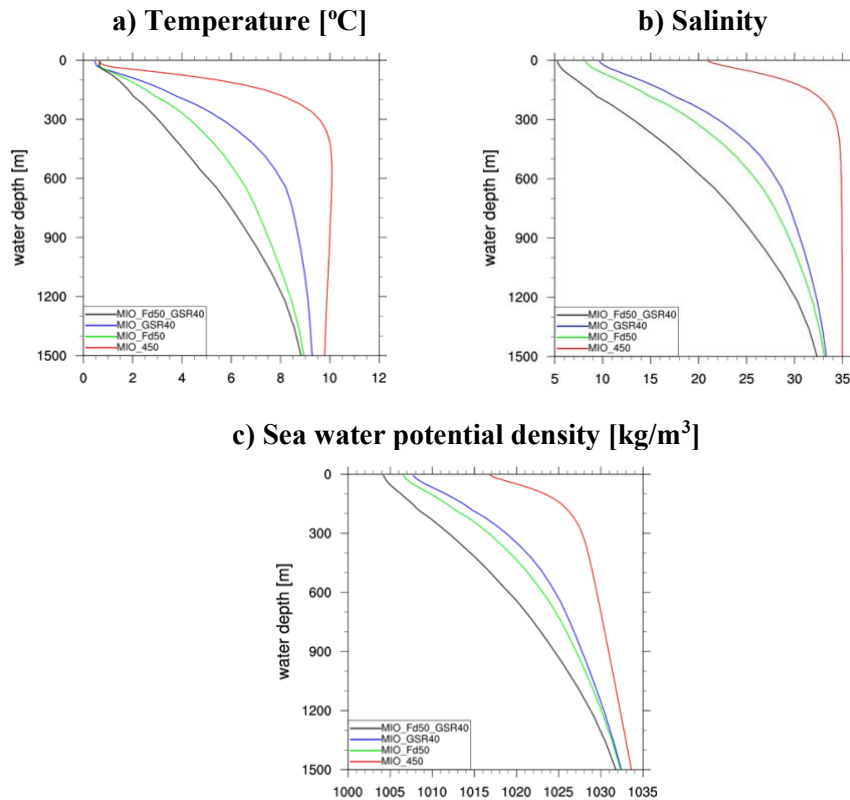


**Figure 3.5.** Evolution of a) temperature (in °C), b) salinity (in psu) and c) density (in kg/m<sup>3</sup>) profiles in the Arctic as a consequence of gateways changes.

As NADW is formed at cooler temperatures, the associated cooling in the deep ocean (Figure 3.4b) and upwelling of deep waters to the Southern Ocean surface causes a cooling in the southern high latitudes (Figures 3.3 and 3.4), which is additionally boosted by enhanced westerlies (Figure 3.7a). As a consequence, deepening the GSR sill generates a cooling of up to  $-3$  °C in the Southern Ocean. This is accompanied by increase in perennial sea-ice cover as detected in the Ross Sea (Figure 3.4a).

By means of three additional sensitivity experiments (listed in Table S3.1) we simulate the progressive deepening of GSR by stepwise changes from 40 mbsl to 500 mbsl for a shallow FS. The associated sub-scenarios to  $\Delta\text{GSR\_FS}_{\text{shallow}}$  ( $\Delta\text{GSR}_{100\_FS_{\text{shallow}}}$ ,  $\Delta\text{GSR}_{300\_FS_{\text{shallow}}}$  and  $\Delta\text{GSR}_{500\_FS_{\text{shallow}}}$ ; Table S3.2) show the same basic characteristics with stronger magnitudes of change for a deeper GSR sill (please see Appendix Text S1 for further details).

Similar to our scenario  $\Delta\text{GSR\_FS}_{\text{shallow}}$ , Stärz et al. (2017) found cooling (up to  $-2$  °C) south of the GSR. In the Nordic Seas a warming (up to  $+10$  °C) and a salinity increase (up to  $+18$  psu) is observed. Furthermore, an identical warming (up to  $+2$  °C) but stronger salinity increase (up to  $+14$  psu) is detected in the Arctic Ocean. In contrast to our scenarios  $\Delta\text{GSR\_FS}_{\text{shallow}}$ ,

### 3. Simulated Thermohaline Fingerprints

they found a warming (up to +4 °C) in the Southern Ocean while we observe a cooling (please see section 3.2.3 for further details).

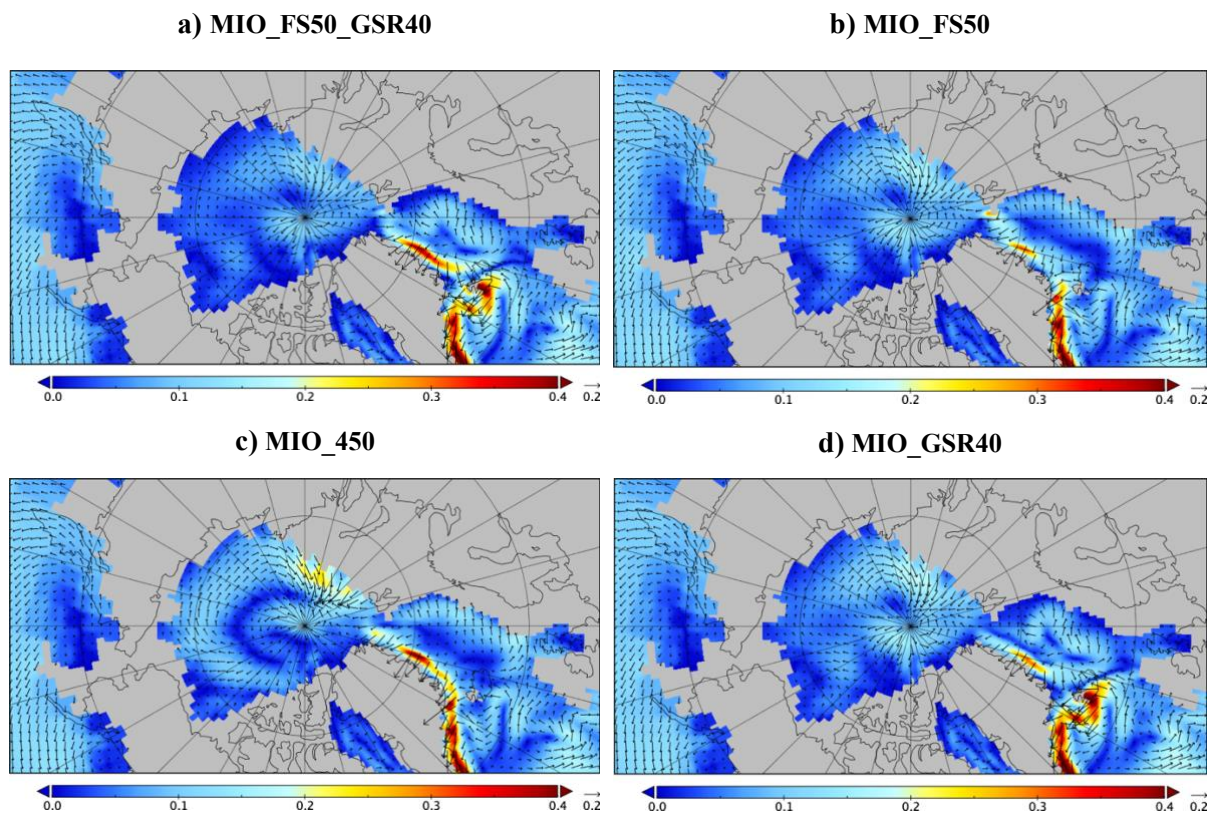


**Figure 3.6.** Ocean velocity at the surface (6 m water depth, m/s) for a) MIO\_FS50\_GSR40, b) MIO\_FS50, c) MIO\_450 and d) MIO\_GSR40.

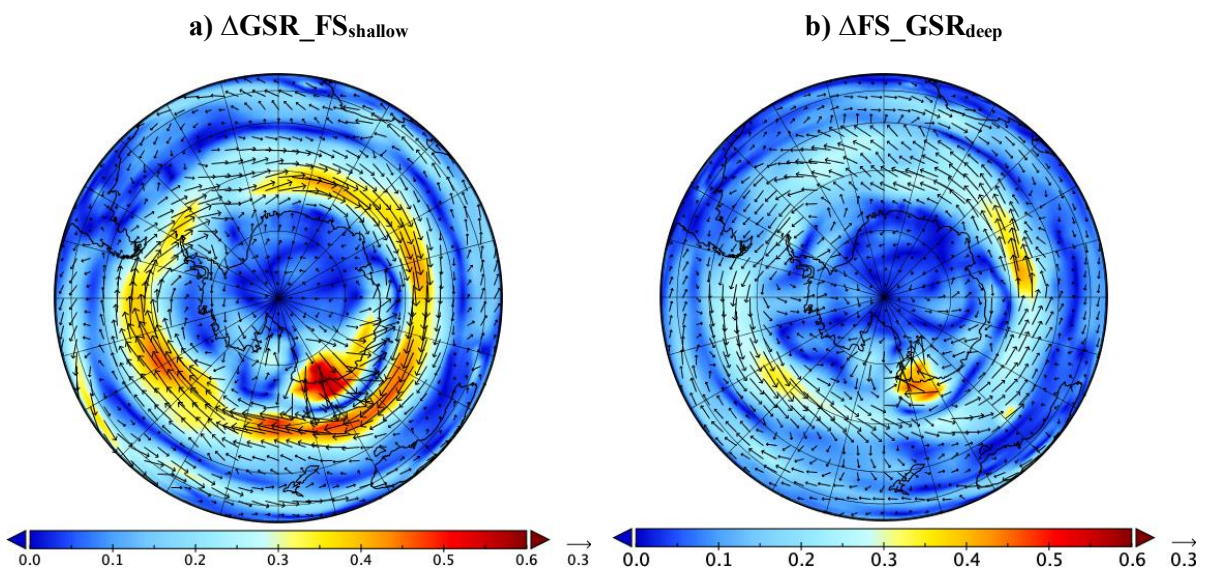


**Figure 3.7.** Change of annual mean wind (m/s) in the Southern Hemisphere for a)  $\Delta\text{GSR\_FS}_{\text{shallow}}$  and b)  $\Delta\text{FS\_GSR}_{\text{deep}}$ .

### 3.2.2 Singular effect of FS deepening for a deep GSR ( $\Delta FS\_GSR_{deep}$ )

An isolated subsidence of the FS from a shallow depth of 50 mbsl towards a fully developed FS depth of  $\sim 2,500$  mbsl for a deep GSR ( $\sim 960$  mbsl;  $\Delta FS\_GSR_{deep}$ ) provides enhanced Atlantic water inflow to the polar/sub-polar Arctic and unrestricted water exchange (Figure 3.2b and 3.2c). In the south of Iceland temperatures and salinity remain unchanged at the surface (Figure 3.8), but a subsurface cooling (up to  $-2$  °C) is observed (Figure 3.9b), linked with southward advection of cold water from the Arctic Ocean.

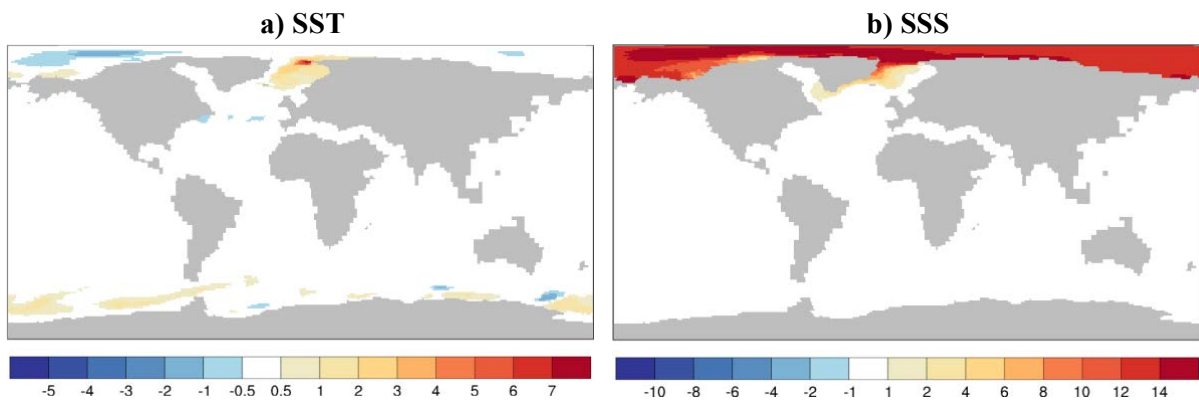


Figure 3.8. Same as Figure 3.3, but for  $\Delta FS\_GSR_{deep}$ .

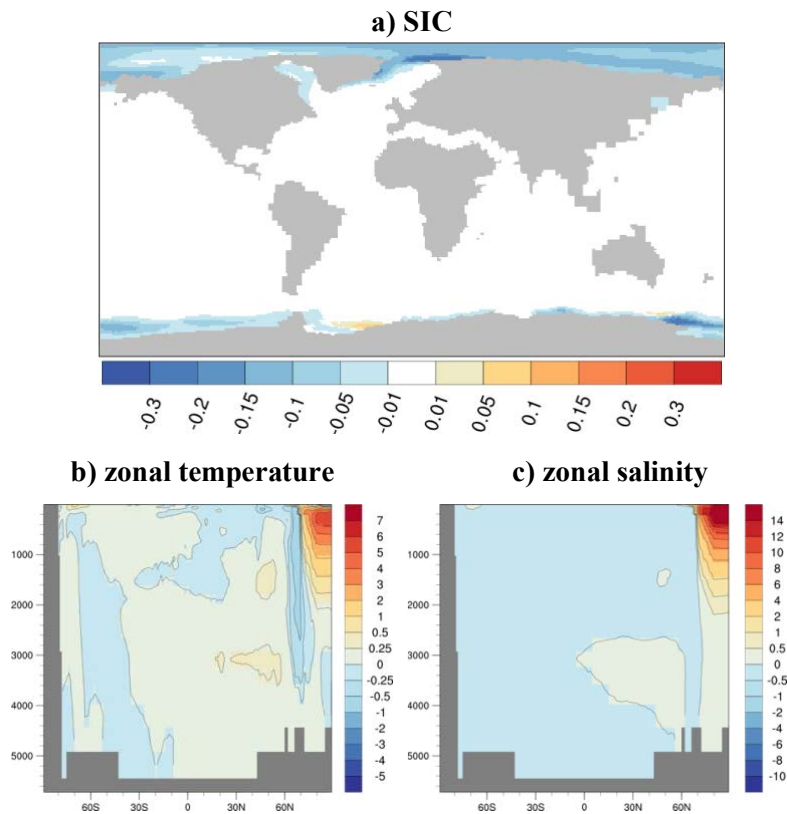
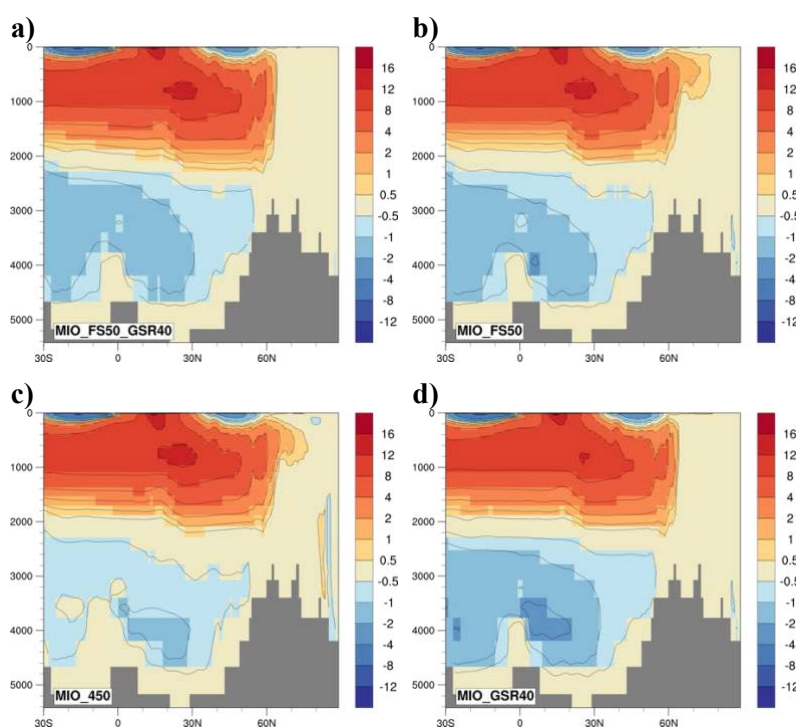


Figure 3.9. a) Sea ice concentration changes and b) zonal mean temperature anomalies (in °C) and c) zonal mean salinity anomalies (in psu) in the Atlantic Ocean for  $\Delta FS\_GSR_{deep}$ .

### 3. Simulated Thermohaline Fingerprints

Subsidence of the FS provides enhanced circulation (Figure 3.10b and 3.10c) of saltier and warmer water from the Atlantic Ocean into the Nordic Seas and Arctic Ocean. We detect a warming (up to +3 °C) and a salinity increase (up to +6 psu) in the Nordic Seas that is less pronounced than in  $\Delta\text{GSR\_FS}_{\text{shallow}}$ . In the Arctic, temperatures remain unaltered at the surface, but warming (up to +6 °C) in sub-surface water, associated with reduced sea-ice cover and a stronger salinity increase (up to +15 psu) is detected (Figures 3.8 and 3.9). The circulation across the FS is characterized by a relatively saline and warm water that is transported north-eastwards in the near-surface/sub-surface layers (upper ~900 m) and at the deepest layers (below ~1500 m). Cold but fresher water from the Arctic Ocean returns southwards in the near-surface layers (upper ~300 m) along the East Greenland coast and at deeper layers (between 900-1500 mbsl) (Figure 3.2b and 3.2c; Figure S3.9b and S3.9c). Due to the bulk inflow of southern source Atlantic water, the Arctic Ocean becomes more saline.



**Figure 3.10.** Atlantic Meridional Overturning Circulation (AMOC; in Sv) for a) *MIO\_FS50\_GSR40*, b) *MIO\_FS50*, c) *MIO\_450* and d) *MIO\_GSR40*.

The strong salinity increase in the Arctic Ocean increases the density of NADW by entrainment. This causes an enhanced contribution of NADW to the abyssal ocean (between 2500-5000 mbsl) (Figure 3.9c) and at the expense of the colder southern source water component (Figure 3.10b and 3.10c). The global AABW index, as defined by the meridional

### 3. Simulated Thermohaline Fingerprints

circulation in the Southern Ocean between 60 and 80°S, decreases by up to  $-0.72$  Sv (Figure 3.10b and 3.10c; Figure S3.9b and S3.9c; Table S3.3). A decrease in AABW formation linked with a weakening of westerlies (Figure 3.7b) decreases upwelling in the Antarctic coast (Figures 3.8a and 3.9b). These relative changes largely counteract each other and cause a negligible warming in the upwelling regions of the Southern Ocean (Figure 3.8a). By using two additional experiments (Table S3.1) we consider the gradual subsidence of FS from 50 mbsl to 300 mbsl while GSR is already deep. In the model sub-scenarios  $\Delta\text{FS}_{100\_}\text{GSR}_{\text{deep}}$  and  $\Delta\text{FS}_{300\_}\text{GSR}_{\text{deep}}$  (Table S3.2) similar basic characteristics as in scenario  $\Delta\text{FS\_}\text{GSR}_{\text{deep}}$  are detected (please see Appendix Text S1 for further details).

#### 3.2.3 Effect of $\Delta\text{GSR\_}\text{FS}_{\text{deep}}$ , $\Delta\text{FS\_}\text{GSR}_{\text{shallow}}$ and $\Delta\text{GSR\_}\Delta\text{FS}$

First, in comparison to the previous scenario  $\Delta\text{GSR\_}\text{FS}_{\text{shallow}}$  we alternatively consider the impact of the GSR deepening for a deep FS sill ( $\sim 2500$  mbsl) in scenario  $\Delta\text{GSR\_}\text{FS}_{\text{deep}}$  (Table 2). The deep FS sill in  $\Delta\text{GSR\_}\text{FS}_{\text{deep}}$  enables the inflow of saline Atlantic water to the Arctic Ocean (Figure 3.2c and 3.2d; Figure S3.8) upon the deepening of the GSR. Furthermore, a modern prototype circulation across the GSR as simulated in Stärz et al. (2017) is established in  $\Delta\text{GSR\_}\text{FS}_{\text{deep}}$ . Temperature and salinity changes south of Iceland are similar to  $\Delta\text{GSR\_}\text{FS}_{\text{shallow}}$ , but warming (up to  $+10$  °C) and salinity increase (up to  $+17$  psu) in the Nordic Seas (Figure 3.11) are more pronounced in  $\Delta\text{GSR\_}\text{FS}_{\text{deep}}$ . In the Arctic, temperature remains unaltered at the surface, but a stronger salinity increase (up to  $+14$  psu) is detected. These Northern Hemisphere thermohaline changes in  $\Delta\text{GSR\_}\text{FS}_{\text{deep}}$  are similar to Stärz et al. (2017), although the Barents Sea region is subaerially exposed in our set-up. By using three additional experiments (Table S3.1) we simulate the gradual subsidence of GSR by stepwise changes from 40 mbsl to 150 mbsl while FS is already deep. The associated sub-scenarios  $\Delta\text{GSR}_{50\_}\text{FS}_{\text{deep}}$ ,  $\Delta\text{GSR}_{80\_}\text{FS}_{\text{deep}}$  and  $\Delta\text{GSR}_{150\_}\text{FS}_{\text{deep}}$  (Table S3.2) show similar basic characteristics as in scenario  $\Delta\text{GSR\_}\text{FS}_{\text{deep}}$  (please see Appendix Text S1 for further details).

In the following we consider the impact of FS deepening for a shallow GSR sill depth (40 mbsl) ( $\Delta\text{FS\_}\text{GSR}_{\text{shallow}}$ ) as an alternative scenario to  $\Delta\text{FS\_}\text{GSR}_{\text{deep}}$ . Temperatures and salinity remain largely unaltered south of Iceland (Figure 3.12). In the Nordic Seas, a salinity decrease (up to  $-6$  psu) and cooling (up to  $-1$  °C) is detected, in contrast to the simulated salinity increase and warming in  $\Delta\text{FS\_}\text{GSR}_{\text{deep}}$ . In the Arctic Ocean temperature remains largely unaltered as in  $\Delta\text{FS\_}\text{GSR}_{\text{deep}}$ , but a less pronounced salinity increase (up to  $+5$  psu) is detected and an anomalous salinity dipole between the Arctic Ocean and Nordic Seas is established (Figure

### 3. Simulated Thermohaline Fingerprints

3.12). This salinity anomaly is linked to ingress of salty waters to the Arctic Ocean and enhanced freshwater export of Arctic origin across the FS. We simulate the gradual subsidence of FS from 50 mbsl to 500 mbsl while GSR is shallow by using three additional experiments (listed in Table S3.1). The associated sub-scenarios  $\Delta FS_{100\_GSR_{shallow}}$ ,  $\Delta FS_{300\_GSR_{shallow}}$  and  $\Delta FS_{500\_GSR_{shallow}}$  (Table S3.2) provide the same basic characteristics with stronger magnitudes of change for a deeper FS sill (please see Appendix Text S1 for further details).

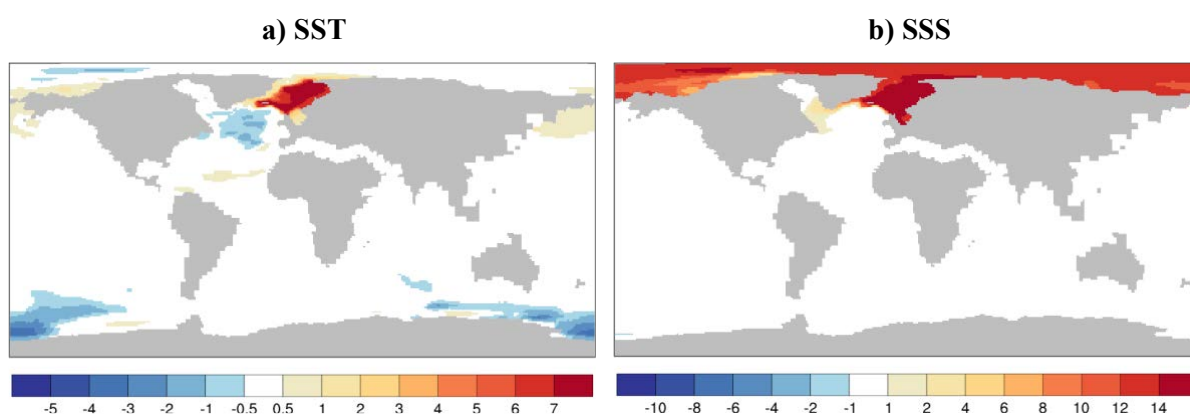


**Figure 3.11.** Same as Figure 3.3, but for  $\Delta GSR_{FS_{deep}}$ .

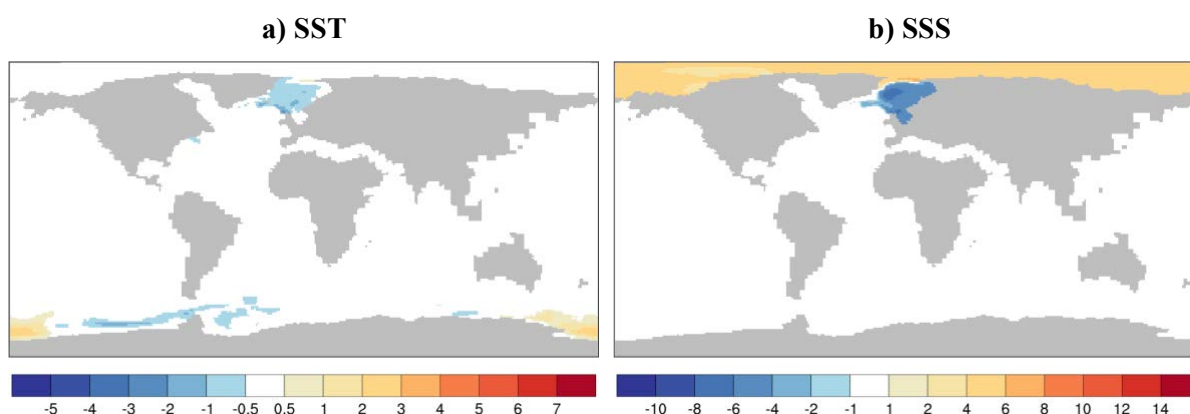


**Figure 3.12.** Same as Figure 3.3, but for  $\Delta FS_{GSR_{shallow}}$ .

Finally, we consider the combined FS deepening from 50 mbsl to  $\sim 2500$  mbsl and GSR deepening from 40 mbsl to  $\sim 960$  mbsl in model scenario  $\Delta GSR_{\Delta FS}$  (Figure 3.13a and 3.13b). The deep sills enable unrestricted ocean water exchange across both gateways at the same time. The resulting thermohaline characteristics have the strongest concurrence to  $\Delta GSR_{FS_{deep}}$ , which highlights the importance of the GSR deepening as the dominant control factor. In the Arctic, temperature remains unaltered, but a more pronounced salinity increase (up to +20 psu)

### 3. Simulated Thermohaline Fingerprints

than in  $\Delta\text{GSR\_FS}_{\text{shallow}}$  and  $\Delta\text{GSR\_FS}_{\text{deep}}$  is detected. Furthermore, the temperature change in the Nordic Seas (up to +8 °C) in  $\Delta\text{GSR\_}\Delta\text{FS}$  is within the range of these two scenarios. By means of three different model sensitivity experiments (Table S3.1) we examine the combined deepening of GSR from 40 mbsl to 500 mbsl and FS deepening from 50 mbsl to 500 mbsl at the same time by stepwise changes. The associated sub-scenarios to  $\Delta\text{GSR\_}\Delta\text{FS}$  ( $\Delta\text{GSR}_{100\_}\Delta\text{FS}_{100}$ ,  $\Delta\text{GSR}_{300\_}\Delta\text{FS}_{300}$ , and  $\Delta\text{GSR}_{500\_}\Delta\text{FS}_{500}$ ; Table S3.2) show the similar basic characteristics with stronger magnitudes of change for a deeper GSR and FS sill (please see Appendix Text S1 for further details).

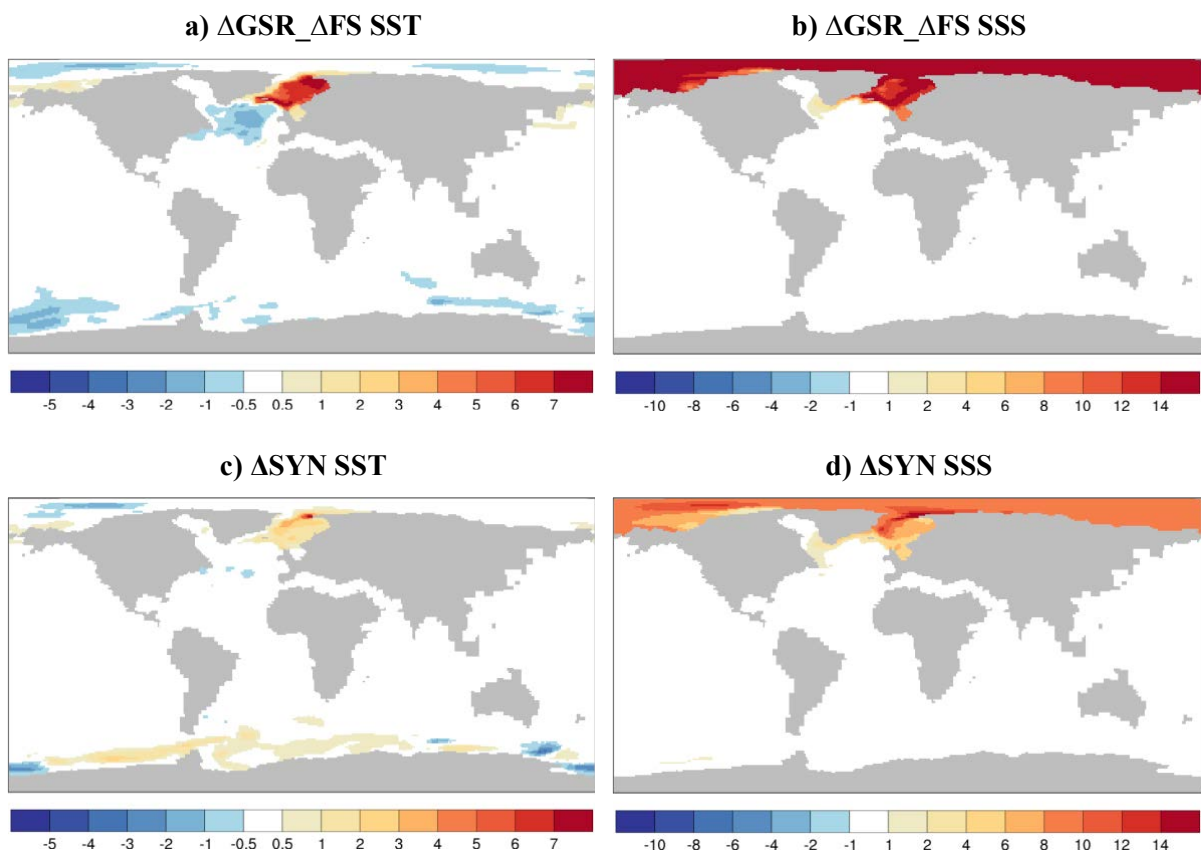


**Figure 3.13.** Same as Figure 3.3, but for  $\Delta\text{GSR\_}\Delta\text{FS}$  (a, b) and the application of a synergy analysis between gateway changes (c, d).

In order to analyse the synergy effect of combined GSR and FS deepening (from shallow conditions), we adapt a factor separation analysis (Stein and Alpert, 1993). According to this analysis the synergy ( $\Delta\text{SYN}$ ) can be expressed by the difference of the combined sill deepening effect ( $\Delta\text{GSR\_}\Delta\text{FS}$ ) and the singular effects  $\Delta\text{GSR}$  and  $\Delta\text{FS}$  (Figure 3.13c and 3.13d). The synergetic effects show a warming in the Nordic Seas, which in fact should be interpreted as cooling effect of FS deepening for a shallow GSR ( $\Delta\text{FS\_GSR}_{\text{shallow}}$ ; Figure 3.12a). However,

### 3. Simulated Thermohaline Fingerprints

this cooling effect turns into a warming signature for a FS deepening once the GSR is already deep ( $\Delta\text{FS\_GSR}_{\text{deep}}$ ; Figure 3.8a). Similarly, the salinity dipole with a Nordic Sea decrease and Arctic increase in  $\Delta\text{FS}$  (FS deepening) is only established while the GSR is shallow ( $\Delta\text{FS\_GSR}_{\text{shallow}}$ ; Figure 3.12b). In that sense, the dipole mainly represents a redistribution of salinity across the FS, but the combined mean salinity is almost constant ( $\sim 24$  psu). In contrast once the GSR is already deep the FS deepening enables a net salinity increase in the Nordic Seas and Arctic Ocean (up to +15 psu, Figure 3.8b), which explains the strong positive salinities in  $\Delta\text{SYN}$ .

## 3.3 Discussion

During the Cenozoic, the Arctic Ocean changes from a restricted freshwater regime towards a more saline modern ocean. These massive oceanographic changes are argued to be driven by the subsidence of the GSR (Stärz et al., 2017) and opening of FS (Jakobsson et al. 2007; Thompson et al., 2012). The evolution of a land-locked Arctic Ocean to a fully ventilated ocean regime, characterized by a warmer ocean with higher salinities (Waddell and Moore, 2008; Thompson et al., 2012) initiated at  $\sim 18.2$  Ma as a consequence of the opening/deepening of the FS (Moran et al., 2006; Jakobsson et al., 2007; Ehlers and Jokat, 2013). Previous studies (i.e., Jakobsson et al., 2007; Thompson et al., 2012) suggested that the FS was narrower than the width we have considered in order to induce ventilation of the Arctic Ocean. Given a rotational control for widths of a more than ca. 50 km (Thompson et al., 2012) we expect that the dynamic control for widths less than this, represents a hydraulic regime. Hence, from the point of ventilation, we do not expect a big difference to Jakobsson et al. (2007) and Thompson et al. (2012) if we would apply similar widths.

The progressive deepening of both Nordic gateways permits increased export of NADW to the abyssal ocean during the Miocene. This agrees with the findings of previous studies (Poore et al., 2006; Knies et al., 2014). Transformation of these water-masses associated with mixing and upwelling to the Southern Ocean surface cause a negligible warming in the southern high latitudes (Figure 3.8a) (Gordon, 1981; Wright and Miller, 1996). Warmer water temperatures and reduction of sea-ice cover along the Antarctic coast of Southern Ocean, leading to an overall reduction in AABW production (Huang et al., 2017) is detected in  $\Delta\text{FS\_GSR}_{\text{deep}}$  (FS deepening for a deep GSR sill depth). In contrast, during the mid-Miocene ( $\sim 15.6$  Ma), an

increase in AABW production is found in the oxygen and carbon isotopes retrieved from deep-sea drill sites (Flower and Kennett, 1995; Wright and Miller, 1996), which supports the results of  $\Delta\text{GSR\_FS}_{\text{shallow}}$  (GSR deepening for a shallow FS) (Figure 3.10a and 3.10b). Sea surface cooling around the Antarctic coastline is linked to an increase in sea-ice extent and the associated ice-albedo feedback (Huang et al., 2017). Previous investigation by von der Heydt and Dijkstra, (2006) using the Community Climate System Model (CCSM) version 1.4, simulated Miocene (~20 Ma) conditions with fresher Nordic Seas than the Arctic Ocean, in agreement with the salinity dipole found in our  $\Delta\text{FS\_GSR}_{\text{shallow}}$  (FS deepening for a shallow GSR) scenario.

#### 3.3.1 Geological constraints and model scenarios

Seismic reflection profiles of Reykjanes Ridge (south of Iceland) show the evolution of Icelandic mantle plume activity back to 55 Ma (Parnell-Turner et al., 2014). Seismic profiles indicate a strong decline (tectonic dormancy) in Icelandic mantle plume activity between ~55-36 Ma, but still with a subaerial Reykjanes Ridge at the end of this period. The GSR gateway started to form already around 36 Ma (Davies et al., 2001; Laberg et al., 2005; Stürz et al., 2017). At the time of GSR sill deepening, Svalbard was very close to North East Greenland (Ehlers and Jokat, 2013). With time, the FS gateways formed and widened as a consequence of a large strike slip movement between Greenland and Svalbard. The geophysical data in the FS (Jokat et al., 2016) provide sound constraints that at the time when GSR deepening initiated, the FS was shallow.

The subsequent opening of FS is relatively well constrained by magnetic data that show initial oceanic crust within the FS might have been formed between 24 to 21 Ma (Jokat et al., 2016). Seismic studies in the northern North Atlantic and Chukchi Plateau, central Arctic Ocean, support the scenario that a restricted shallow water exchange between the northern North Atlantic and the Arctic Ocean is likely in this time period (Jokat et al., 2008; Hegewald and Jokat, 2013). From ~24 Ma onwards, the FS becomes deeper and wider (Ehlers and Jokat, 2013).

Further south, GSR sill is already well below sea level (below ~300 m) between ~20-24 Ma (Stürz et al., 2017). In combination, geological evidence and our results suggest a singular subsidence of GSR towards a deep gateway configuration for a shallow FS ( $\Delta\text{GSR\_FS}_{\text{shallow}}$ ) is a likely scenario for the time period of around  $20\pm 3$  Ma (Jokat et al., 2008; Hegewald and Jokat, 2013; Jokat et al., 2016; Stürz et al., 2017).

### 3. Simulated Thermohaline Fingerprints

Jokat et al. (2008) suggest from analysing seismic data across the Yermak Plateau that a shallow water exchange between the Nordic Seas and the Arctic Ocean already existed well before establishment of a deep-water passage in the FS. The interpretation of magnetic and seismic data reveals that the formation of oceanic crust likely initiated in the FS at ~21 Ma (Jokat et al., 2016). A paleo-bathymetric model based on these regional seismic and magnetic data shows that a deep-water exchange between the Nordic Seas and the Arctic Ocean was likely between 17 and 20 Ma (Ehlers and Jokat, 2013). As the formation of oceanic crust initiated at ~21 Ma, the FS deepened to sill depths greater than 1,500 mbsl at around 17 Ma. Scientific drilling indicates a fully ventilated Arctic Ocean from 18.2 Ma onwards allowing an unrestricted exchange of deep Arctic water and warm Atlantic water (Moran et al., 2006; Jakobsson et al., 2007). Further, progressive deepening of the GSR sill allowed increased outflow of NADW to the Atlantic Ocean through late Miocene (Poore et al., 2006; Knies et al., 2014). Therefore, subsidence of the FS from a shallow depth towards a fully developed FS depth for a deep GSR ( $\Delta FS\_GSR_{deep}$ ) would be the likely scenario for time period younger than 18 Ma (Jokat et al., 2008; Ehlers and Jokat, 2013; Starz et al., 2017).

In summary, from the geophysical/geological data we deduce that the scenarios of  $\Delta GSR\_FS_{deep}$ ,  $\Delta FS\_GSR_{shallow}$  and  $\Delta GSR\_FS$  are three unlikely configurations from a tectonic point of view considering relative timing of subsidence of both gateways. Therefore, we suggest the most likely scenario that provide fingerprints of characteristic thermohaline changes based on geological evidence and tectonic constraints are: Phase 1: GSR sill gradually subsidence towards a deep gateway configuration for a shallow FS sill depth ( $\Delta GSR\_FS_{shallow}$ ) at around  $20 \pm 3$  Ma (Jokat et al., 2016), and Phase 2: the opening of FS initiated when GSR is already deeper than ~300 m ( $\Delta FS\_GSR_{deep}$ ) between ~20-24 Ma (Starz et al., 2017).

## 3.4 Conclusions of Chapter Three

By applying the climate model COSMOS, we have analysed the impact of GSR and FS subsidence on the ocean circulation and climate during early to middle Miocene in different model scenarios. The subsidence of GSR and FS enables enhanced circulation of saltier and warmer water from the Atlantic Ocean into the Nordic Seas and Arctic Ocean that induces a salinization process in this region. Deepening of the GSR causes warming and a salinity increase in the Nordic Sea/Arctic Ocean and cooling in the southern high latitudes. These

### 3. Simulated Thermohaline Fingerprints

fingerprints of characteristic thermohaline changes in response to the GSR deepening are independent of the FS state. Furthermore, deepening of the FS gateway for a deep GSR causes less pronounced warming and salinity increase in the Nordic Seas. In contrast unchanged temperatures and a stronger salinity increase in the Arctic and a negligible warming in the upwelling regions of the Southern Ocean are detected in our model simulations. Considering the impact of the gateways' subsidence, the GSR deepening is the dominant controlling factor for thermohaline changes.

Based on the geological/geophysical constraints we conjecture that a tectonic situation with a progressive GSR deepening for a shallow FS sill depth configuration is the most likely Eocene to Miocene scenario ( $\Delta\text{GSR\_FS}_{\text{shallow}}$ ). The deepening of FS initiated when GSR was already becoming deep ( $\Delta\text{FS\_GSR}_{\text{deep}}$ ). In contrast, deepening of the FS for a shallow GSR ( $\Delta\text{FS\_GSR}_{\text{shallow}}$ ) or GSR deepening while the FS is already deep ( $\Delta\text{GSR\_FS}_{\text{deep}}$ ), as well as the combined deepening of both gateways at the same time ( $\Delta\text{GSR\_}\Delta\text{FS}$ ) are unlikely scenarios.

Future data from up-coming drilling projects can use our scenarios and these characteristic thermohaline changes as basis for various interpretation models to test and further our understanding of the high-latitude climate evolution by superposed gateway changes.

## 3.5 Appendix

### **Text S1: Effect of GSR and FS deepening at different sill depths (Sub-scenarios)**

An isolated subsidence of GSR from 40 mbsl to 500 mbsl by stepwise changes for a shallow FS ( $\Delta\text{GSR}_{100\_}\text{FS}_{\text{shallow}}$ ,  $\Delta\text{GSR}_{300\_}\text{FS}_{\text{shallow}}$  and  $\Delta\text{GSR}_{500\_}\text{FS}_{\text{shallow}}$ ; Table S3.2) show the same basic characteristics in salinity as  $\Delta\text{GSR\_FS}_{\text{shallow}}$  with stronger magnitudes of change for a deeper GSR sill (Figure S3.1). The SST changes in the North Atlantic/Arctic appear to steadily become stronger with increasing sill depths. In the model sub-scenario  $\Delta\text{GSR}_{100\_}\text{FS}_{\text{shallow}}$ , we observe a strong cooling (up to  $-4\text{ }^{\circ}\text{C}$ ) in the Southern Ocean (Figure S3.1). On the other hand, in  $\Delta\text{GSR}_{300\_}\text{FS}_{\text{shallow}}$  and  $\Delta\text{GSR}_{500\_}\text{FS}_{\text{shallow}}$  we detect less pronounced cooling (up to  $-2\text{ }^{\circ}\text{C}$ ) in the Southern Ocean.

### 3. Simulated Thermohaline Fingerprints

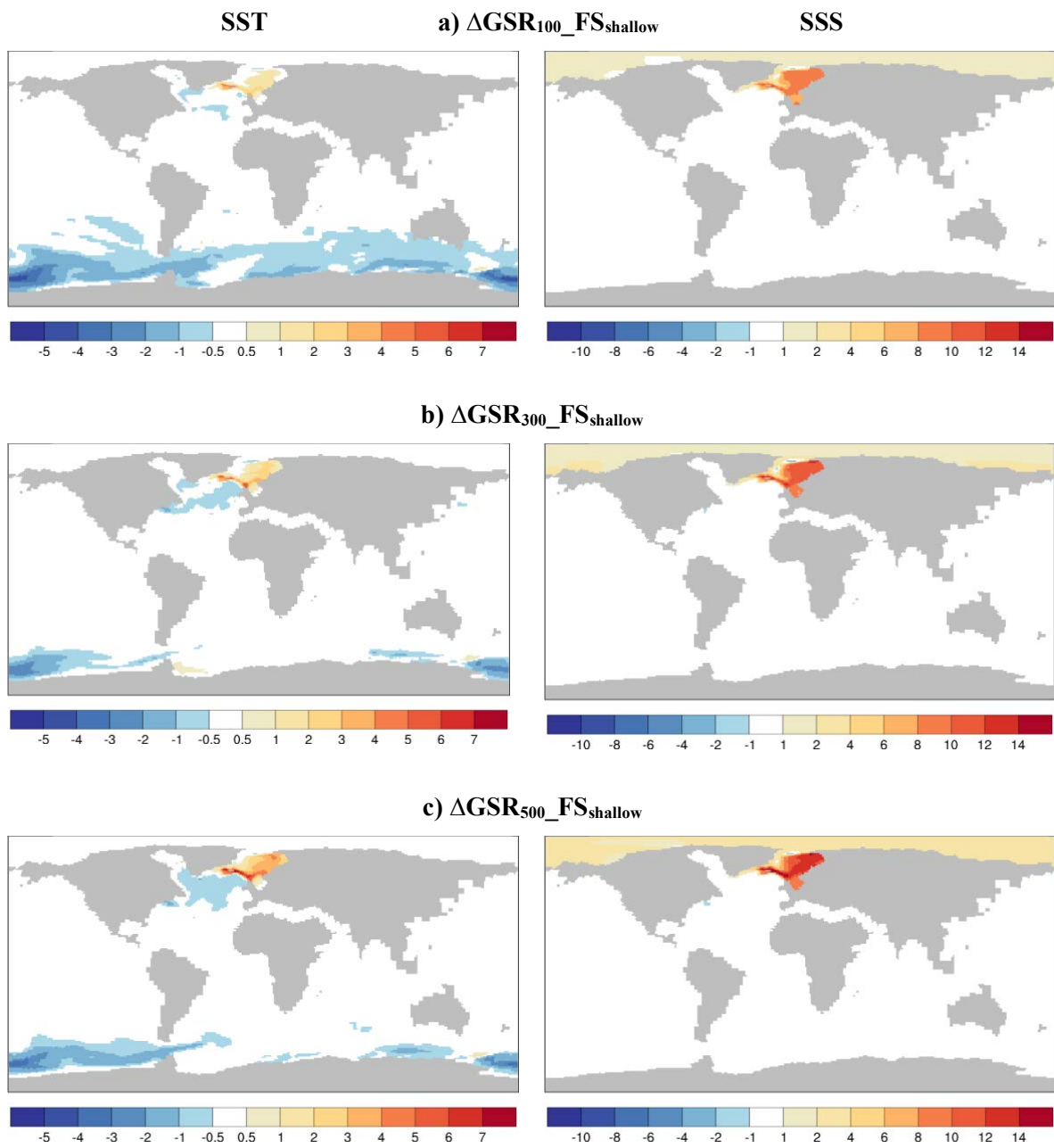


**Figure S3.1.** The effect of (a)  $\Delta GSR_{100\_FS_{shallow}}$ , (b)  $\Delta GSR_{300\_FS_{shallow}}$  and (c)  $\Delta GSR_{500\_FS_{shallow}}$  on sea surface temperature anomalies (SST; in  $^{\circ}\text{C}$ ) and sea surface salinity anomalies (SSS; in psu).

### 3. Simulated Thermohaline Fingerprints

By means of two different model sensitivity experiments (Table S3.1) we consider the gradual subsidence of FS from 50 mbsl to 300 mbsl while GSR is already deep. The associated sub-scenarios to  $\Delta FS\_GSR_{deep}$  ( $\Delta FS_{100\_GSR_{deep}}$  and  $\Delta FS_{300\_GSR_{deep}}$ ) show similar basic characteristics in salinity with stronger magnitudes of change for a deeper FS sill (Figure S3.2). In the model sub-scenario  $\Delta FS_{100\_GSR_{deep}}$ , we detect minor warming (up to +1 °C) in the Nordic Seas and cooling (up to -2 °C) in the Arctic Ocean. On the other hand, in  $\Delta FS_{300\_GSR_{deep}}$  we observe warming (up to +2 °C) in the Nordic Seas and a negligible cooling (up to -1 °C) in the Arctic Ocean. We also observe a negligible warming in the upwelling regions of the Southern Ocean (Figure S3.2).

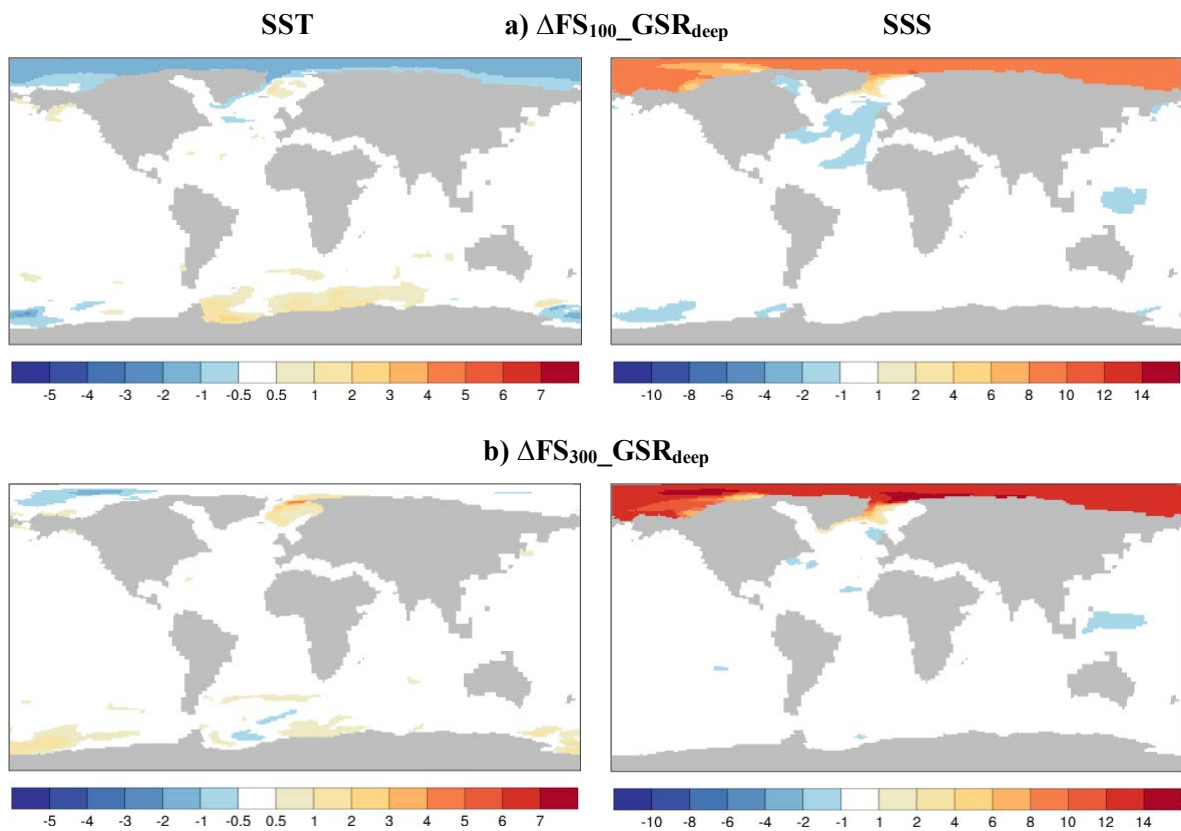


**Figure S3.2.** The effect of (a)  $\Delta FS_{100\_GSR_{deep}}$  and (b)  $\Delta FS_{300\_GSR_{deep}}$  on on sea surface temperature anomalies (SST; in °C) and sea surface salinity anomalies (SSS; in psu).

### 3. Simulated Thermohaline Fingerprints

We simulate the gradual subsidence of GSR by stepwise changes from 40 mbsl to 150 mbsl while FS is already deep in three sub-scenarios ( $\Delta\text{GSR}_{50\_FS_{\text{deep}}}$ ,  $\Delta\text{GSR}_{80\_FS_{\text{deep}}}$  and  $\Delta\text{GSR}_{150\_FS_{\text{deep}}}$ ). They show similar basic characteristics as in scenario  $\Delta\text{GSR\_FS}_{\text{deep}}$  discussed in Section 3.2.3 (Figures S3.3).

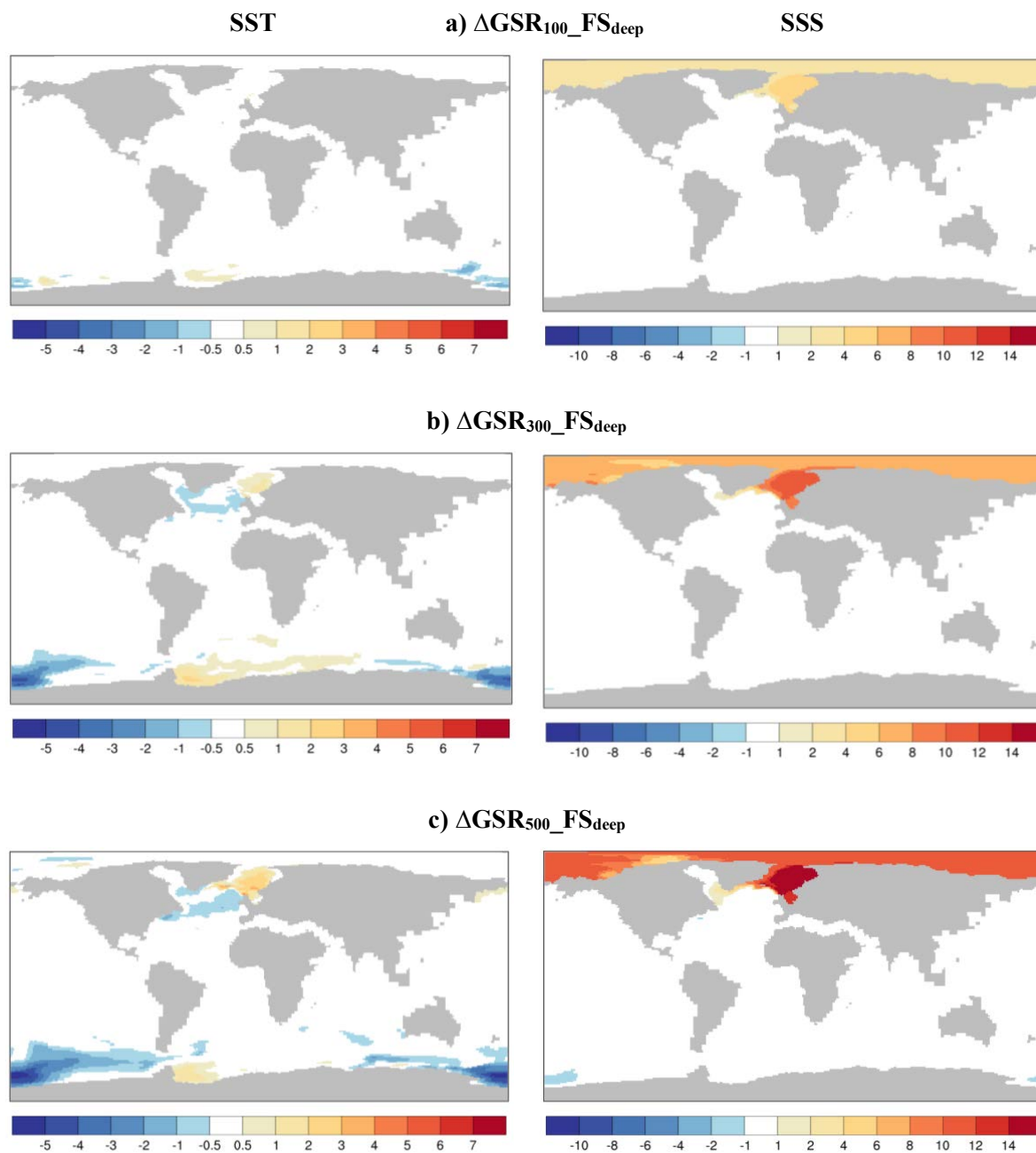


**Figure S3.3.** The effect of (a)  $\Delta\text{GSR}_{100\_FS_{\text{deep}}}$ , (b)  $\Delta\text{GSR}_{300\_FS_{\text{deep}}}$  and (c)  $\Delta\text{GSR}_{500\_FS_{\text{deep}}}$  on sea surface temperature anomalies (SST; in  $^{\circ}\text{C}$ ) and sea surface salinity anomalies (SSS; in  $\text{psu}$ ).

### 3. Simulated Thermohaline Fingerprints

The associated sub-scenarios to  $\Delta FS\_GSR_{shallow}$  (discussed in Section 3.2.3;  $\Delta FS_{100}\_GSR_{shallow}$ ,  $\Delta FS_{300}\_GSR_{shallow}$  and  $\Delta FS_{500}\_GSR_{shallow}$ ) provide the same basic characteristics with stronger magnitudes of change for a deeper FS sill (Figures S3.4).

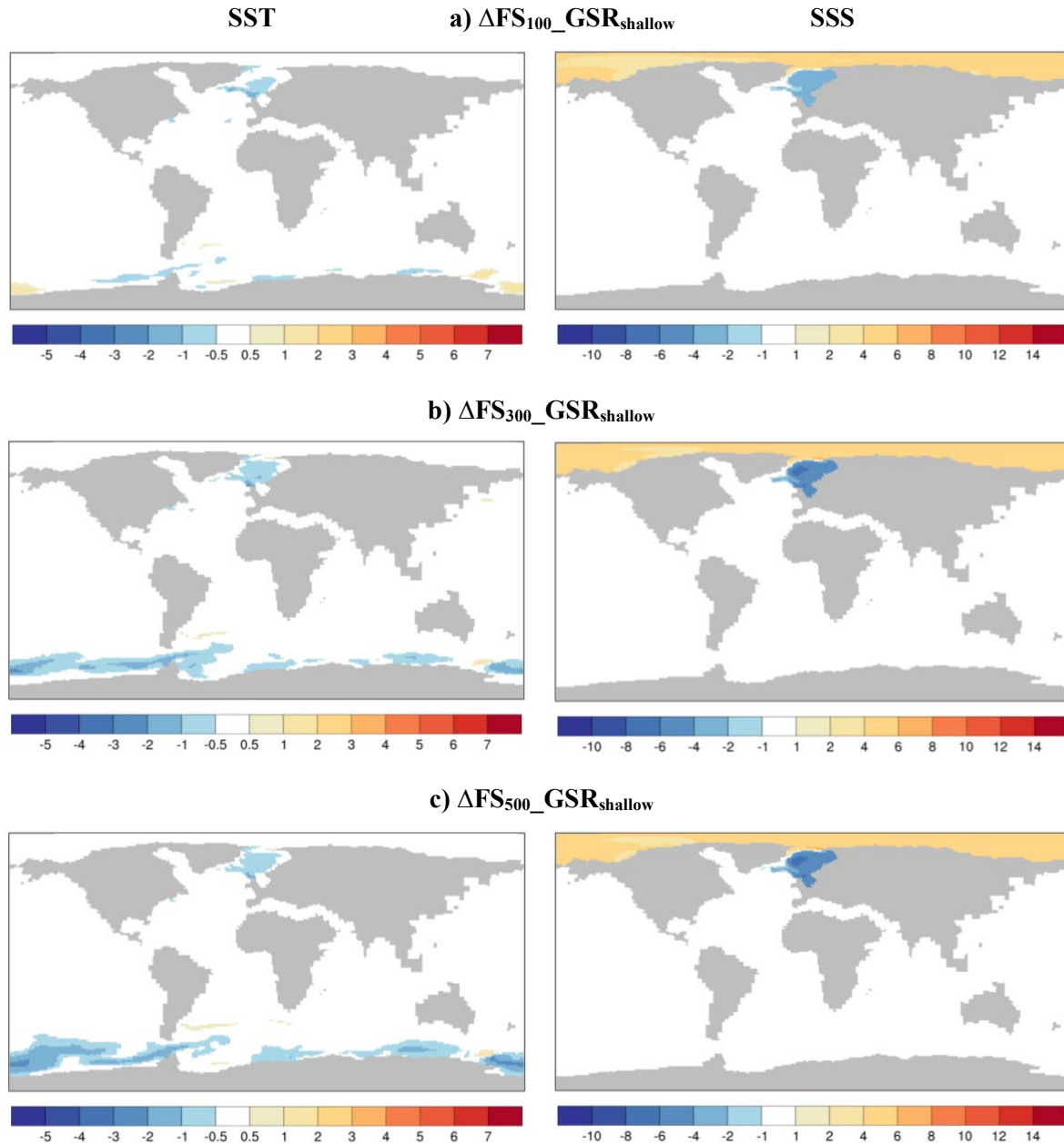


**Figure S3.4.** The effect of (a)  $\Delta FS_{100}\_GSR_{shallow}$ , (b)  $\Delta FS_{300}\_GSR_{shallow}$  and (c)  $\Delta FS_{500}\_GSR_{shallow}$  on sea surface temperature anomalies (SST; in °C) and sea surface salinity anomalies (SSS; in psu).

By using three different sub-scenarios ( $\Delta GSR_{100}\_AFS_{100}$ ,  $\Delta GSR_{300}\_AFS_{300}$ , and  $\Delta GSR_{500}\_AFS_{500}$ ) we examine the combined deepening of GSR from 40 mbsl to 500 mbsl and FS deepening from 50 mbsl to 500 mbsl at the same time by stepwise changes. They show the

### 3. Simulated Thermohaline Fingerprints

similar basic characteristics in salinity (Figure S3.5). In the model sub-scenario  $\Delta\text{GSR}_{100}\text{-}\Delta\text{FS}_{100}$ , we observe a weak warming (up to +1 °C) in the Nordic Seas and unaltered Arctic Ocean (Figure S3.5). On the other hand, in  $\Delta\text{GSR}_{300}\text{-}\Delta\text{FS}_{300}$  we detect warming (up to +4 °C) in the Nordic Seas and cooling (up to -1 °C) in the Arctic Ocean. We also observe a stronger cooling (up to -5 °C) in the Southern Ocean (Figure S3.5). Again, in  $\Delta\text{GSR}_{500}\text{-}\Delta\text{FS}_{500}$ , we observe a stronger warming (up to +6 °C) in the Nordic Seas and a little cooling in the Arctic Ocean. We detect a threshold in temperature for sub-scenario  $\Delta\text{GSR}_{300}\text{-}\Delta\text{FS}_{300}$  (Figure S3.5).

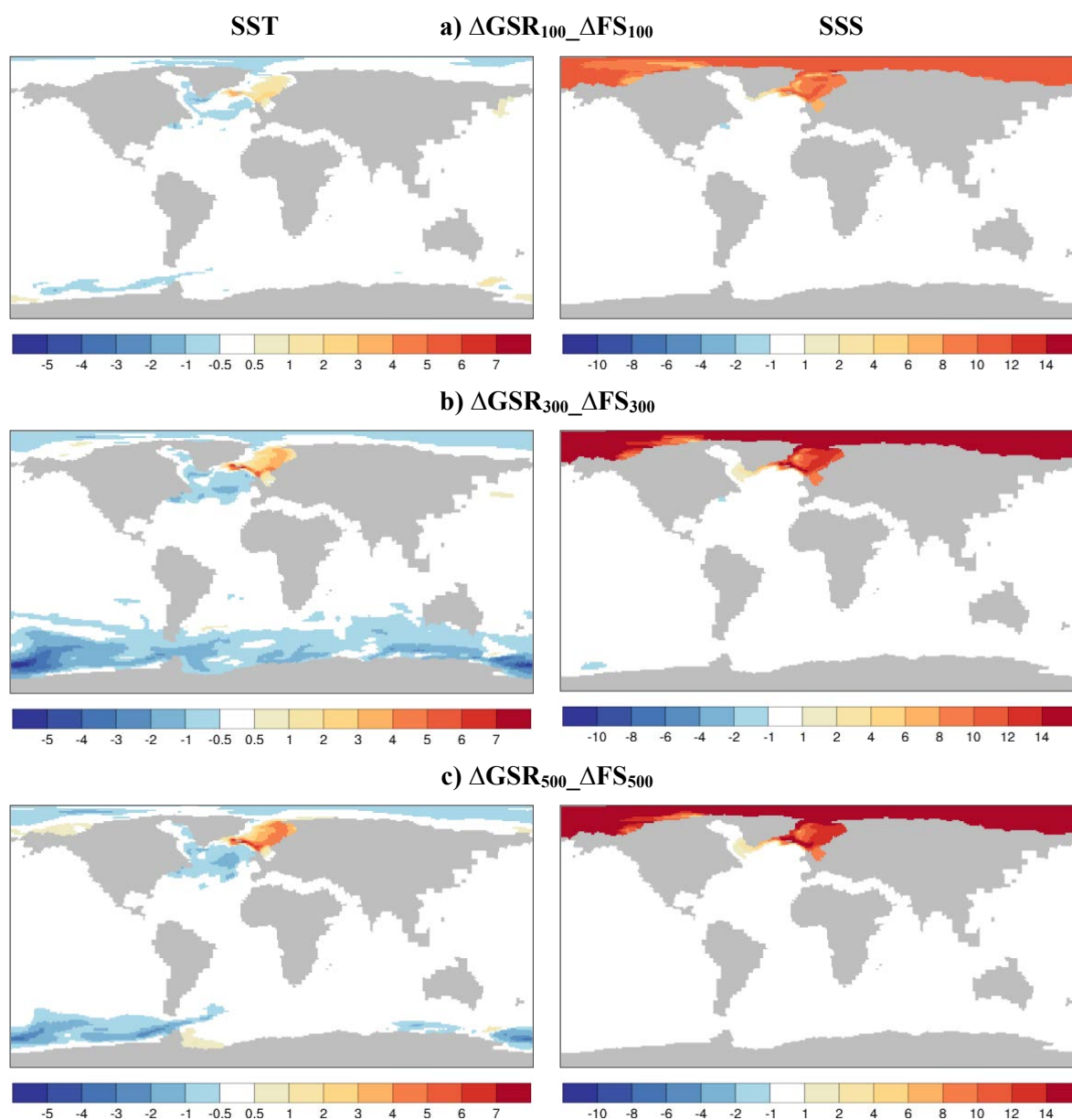


**Figure S3.5.** The effect of (a)  $\Delta\text{GSR}_{100}\text{-}\Delta\text{FS}_{100}$ , (b)  $\Delta\text{GSR}_{300}\text{-}\Delta\text{FS}_{300}$  and (c)  $\Delta\text{GSR}_{500}\text{-}\Delta\text{FS}_{500}$  on sea surface temperature anomalies (SST; in °C) and sea surface salinity anomalies (SSS; in psu).

### 3. Simulated Thermohaline Fingerprints

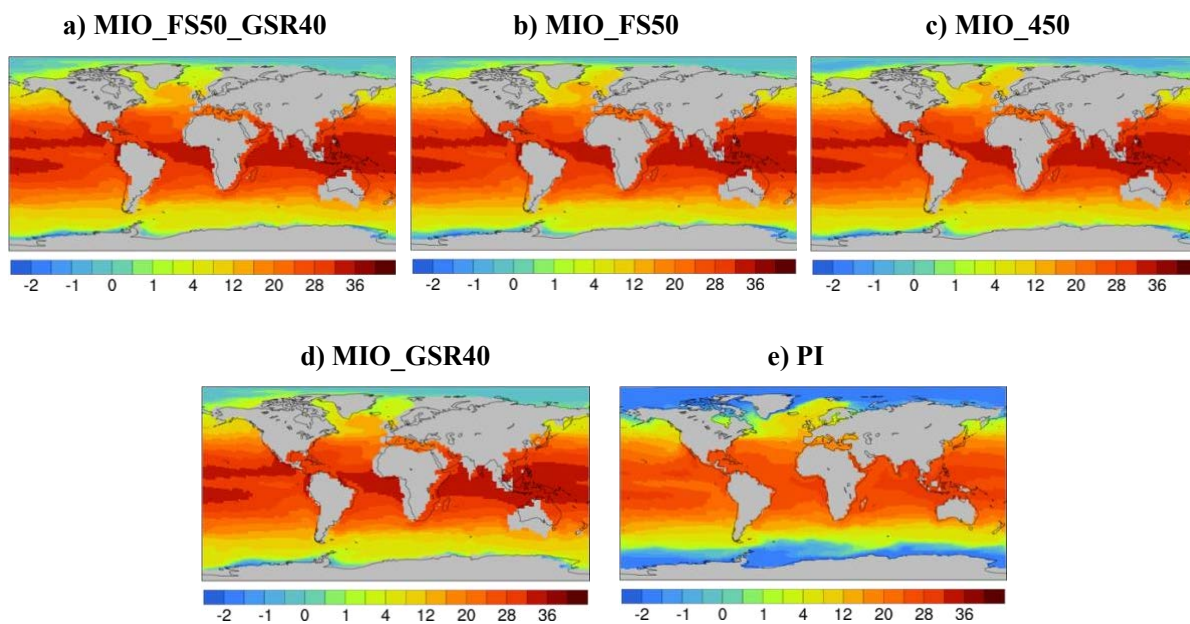


**Figure S3.6.** Annual mean SST (in °C) for a) MIO\_FS50\_GSR40, b) MIO\_FS50, c) MIO\_450 and d) MIO\_GSR40 and e) PI.

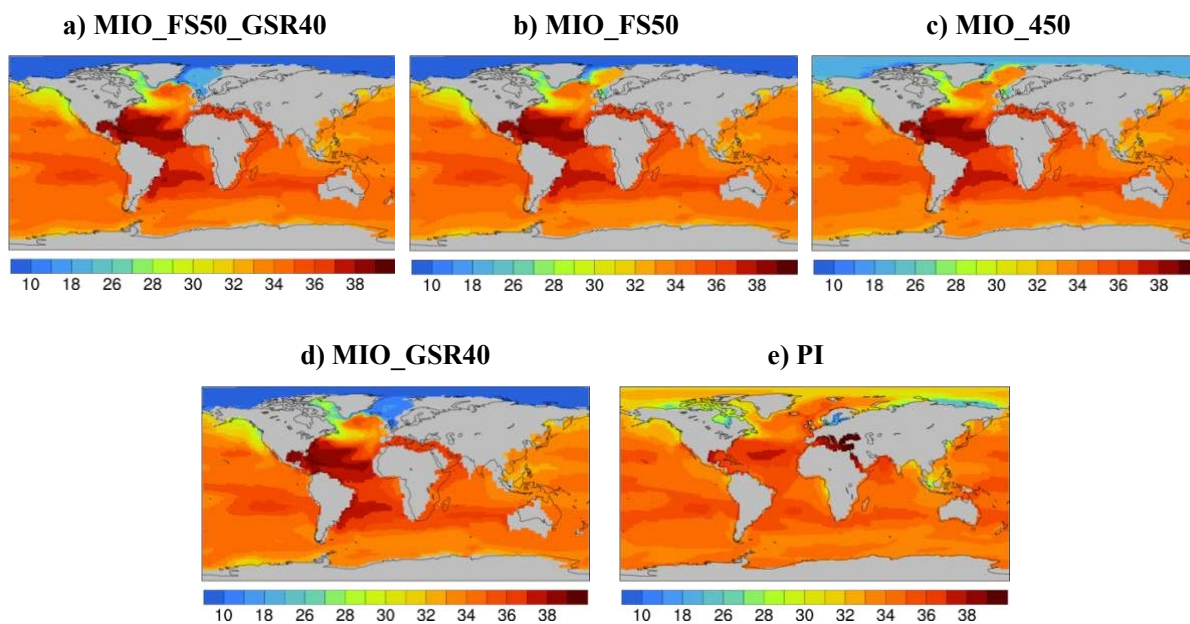


**Figure S3.7.** Annual mean SSS (in psu) for a) MIO\_FS50\_GSR40, b) MIO\_FS50, c) MIO\_450 and d) MIO\_GSR40 and e) PI.

### 3. Simulated Thermohaline Fingerprints

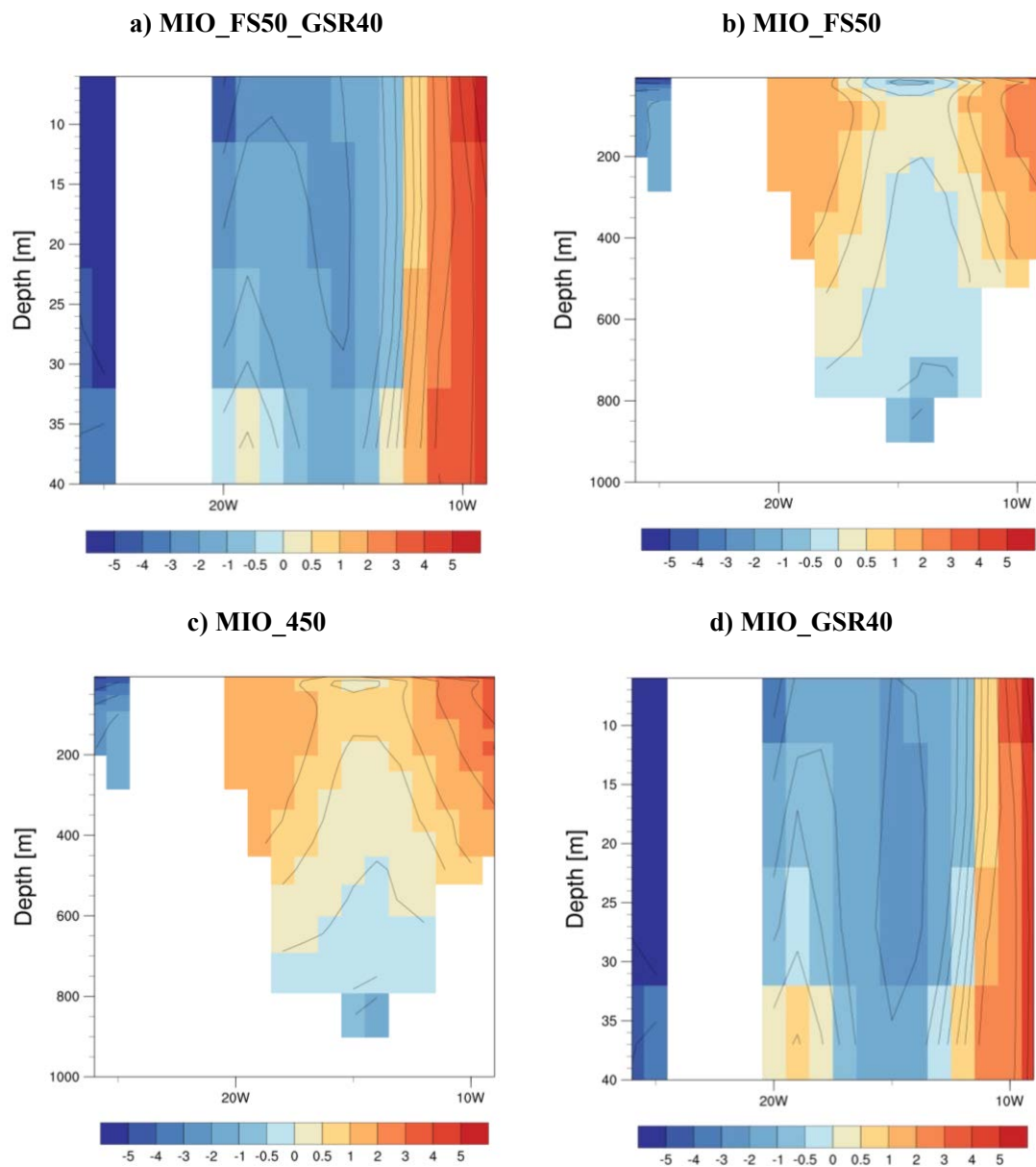


**Figure S3.8.** GSR ocean velocity (pos. northward, neg. southward, cm/s) for a) MIO\_FS50\_GSR40, b) MIO\_FS50, c) MIO\_450 and d) MIO\_GSR40.

### 3. Simulated Thermohaline Fingerprints

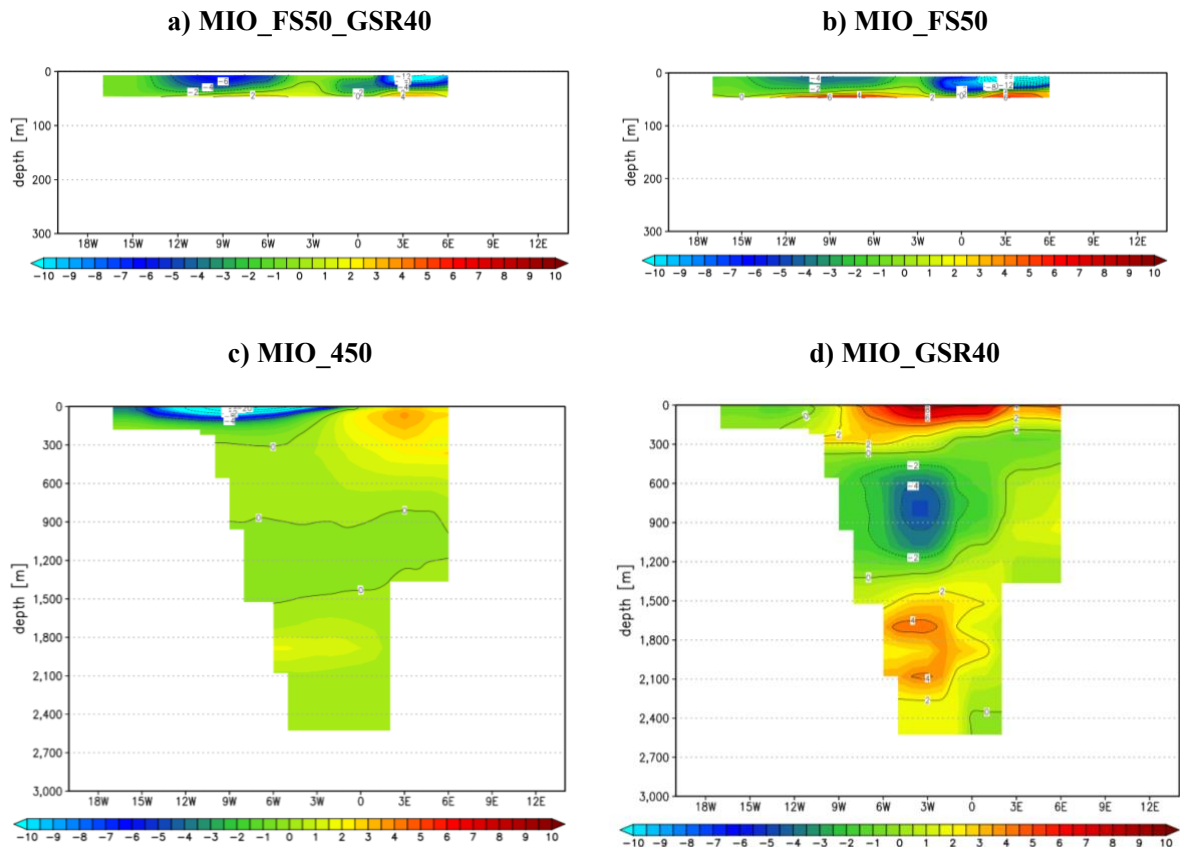


**Figure S3.9.** Fram Strait ocean velocity at 79.5°N (pos. northward, neg. southward, cm/s) for a) MIO\_FS50\_GSR40, b) MIO\_FS50, c) MIO\_450 and d) MIO\_GSR40.

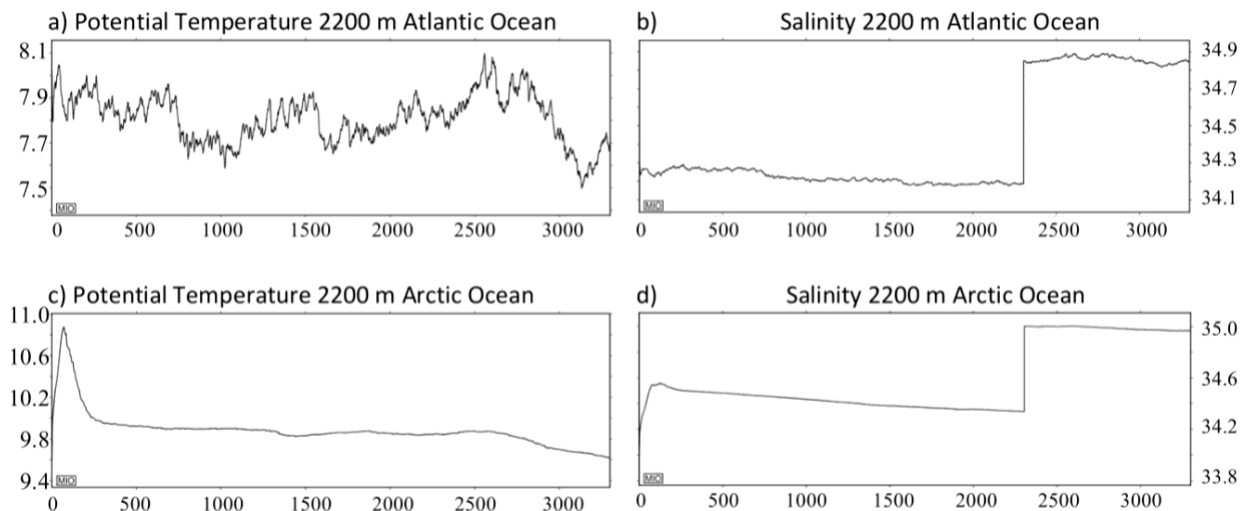


**Figure S3.10.** The spin-up trends in temperature (in °C) and salinity (in psu) for the deep Atlantic (a, b) and deep Arctic Ocean (c, d) for MIO\_450.

### 3. Simulated Thermohaline Fingerprints

**Table S3.1:** List of additional sensitivity experiments.

<b>Model Exp.</b>	<b>Fram depth (m)</b>	<b>GSR depth (m)</b>	<b>Atmos. CO<sub>2</sub> (ppm)</b>	<b>Length of simulation (kyrs)</b>
MIO_FS50_GSR100	50 m	100 m	450	2.0
MIO_FS50_GSR300	50 m	300 m	450	2.0
MIO_FS50_GSR500	50 m	500 m	450	2.0
MIO_FS100	100 m	~960 m	450	1.0
MIO_FS300	300 m	~960 m	450	1.0
MIO_FS100_GSR40	100 m	40 m	450	1.0
MIO_FS300_GSR40	300 m	40 m	450	1.0
MIO_FS500_GSR40	500 m	40 m	450	1.0
MIO_GSR50	~2500 m	50 m	450	1.0
MIO_GSR80	~2500 m	80 m	450	1.0
MIO_GSR150	~2500 m	150 m	450	1.0
MIO_FS100_GSR100	100 m	100 m	450	1.0
MIO_FS300_GSR300	300 m	300 m	450	1.0
MIO_FS500_GSR500	500 m	500 m	450	1.0

### 3. Simulated Thermohaline Fingerprints

**Table S3.2:** List of Sub-scenarios.

Name	Anomaly of experiments	GSR depth change (m)	FS depth change (m)
$\Delta\text{GSR}_{100\_}\text{FS}_{\text{shallow}}$	MIO_FS50_GSR100 – MIO_FS50_GSR40	100 – 40	50
$\Delta\text{GSR}_{300\_}\text{FS}_{\text{shallow}}$	MIO_FS50_GSR300 – MIO_FS50_GSR40	300 – 40	50
$\Delta\text{GSR}_{500\_}\text{FS}_{\text{shallow}}$	MIO_FS50_GSR500 – MIO_FS50_GSR40	500 – 40	50
$\Delta\text{GSR}_{50\_}\text{FS}_{\text{deep}}$	MIO_GSR50 – MIO_GSR40	50 – 40	~2500
$\Delta\text{GSR}_{80\_}\text{FS}_{\text{deep}}$	MIO_GSR80 – MIO_GSR40	80 – 40	~2500
$\Delta\text{GSR}_{150\_}\text{FS}_{\text{deep}}$	MIO_GSR150 – MIO_GSR40	150 – 40	~2500
$\Delta\text{FS}_{100\_}\text{GSR}_{\text{shallow}}$	MIO_FS100_GSR40 – MIO_FS50_GSR40	40	100 – 50
$\Delta\text{FS}_{300\_}\text{GSR}_{\text{shallow}}$	MIO_FS300_GSR40 – MIO_FS50_GSR40	40	300 – 50
$\Delta\text{FS}_{500\_}\text{GSR}_{\text{shallow}}$	MIO_FS500_GSR40 – MIO_FS50_GSR40	40	500 – 50
$\Delta\text{FS}_{100\_}\text{GSR}_{\text{deep}}$	MIO_FS100 – MIO_FS50	~960	100 – 50
$\Delta\text{FS}_{300\_}\text{GSR}_{\text{deep}}$	MIO_FS300 – MIO_FS50	~960	300 – 50
$\Delta\text{GSR}_{100\_}\Delta\text{FS}_{100}$	MIO_FS100_GSR100 – MIO_FS50_GSR40	100 – 40	100 – 50
$\Delta\text{GSR}_{300\_}\Delta\text{FS}_{300}$	MIO_FS300_GSR300 – MIO_FS50_GSR40	300 – 40	300 – 50
$\Delta\text{GSR}_{500\_}\Delta\text{FS}_{500}$	MIO_FS500_GSR500 – MIO_FS50_GSR40	500 – 40	500 – 50

**Table S3.3:** Key Diagnostics of different model simulations.

Model Exp.	Global mean SST (°C)	Global mean SSS (‰)	Arctic Ocean mean SST (°C)	Arctic Ocean mean SSS (‰)	Global AABW Index (60-80 °S, Sv)	AMOC Index (30-60 °N, Sv)
MIO_450	23.05	34.31	0.64	21.02	-1.43	12.37
MIO_FS50	23.03	34.12	0.70	8.21	-2.15	12.36
MIO_GSR40	23.07	33.97	0.46	9.66	-2.50	11.15
MIO_FS50_GSR40	23.03	33.97	0.64	5.27	-1.91	12.04

### *3. Simulated Thermohaline Fingerprints*

## Opening of the Fram Strait Led to the Establishment of a Modern-Like Three-Layer Stratification in the Arctic Ocean during the Miocene

This chapter provide an enhanced simulation with advanced oceanic and atmospheric boundary conditions at the Miocene/Oligocene boundary to understand how fast the oceanographic changes from a two-layer to present-day conditions are possible. Furthermore, the climate model COSMOS is applied to assess the sensitivity of stratification and circulation in the Arctic Ocean to the opening of FS and different levels of atmospheric CO<sub>2</sub> concentrations. The model simulation applies a Miocene-bathymetric reconstruction (Ehlers and Jokat, 2013), which is believed to capture the major bathymetric features, such as different sub-basins and sills. Furthermore, CO<sub>2</sub> changes are used relative to early-middle Miocene (about 23–15 Ma) boundary conditions. In the numerical experiments, several different opening geometries for the FS is investigated to constrain the regional and global climate impacts of this tectonic event.

## 4. Opening of the Fram Strait

*Declaration: this chapter was published in Hossain et al. (2021).*

### 4.1 Model setup and experimental design

In Chapter 3, the impact of single ocean gateway, FS and Greenland-Scotland Ridge (GSR), respectively, on the Arctic Ocean circulation and the combined effect of both is investigated. A non-linear impact of gateway depth on the water mass exchange and ocean circulation is found which is mainly driven by the effect of gateways subsidence and their interaction. This chapter investigates if and how different FS widths could have affected the global ocean circulation and climate between 23 and 15 Ma. The primary focus is on the sensitivity of Arctic Ocean stratification and circulation controlled by FS gateway configurations and CO<sub>2</sub> changes.

**Table 3:** List of sensitivity experiments including relevant model parameters.

Model Exp.	Fram Strait width (km)	max. Fram Strait depth (m)	GSR depth (m)	Atmos. CO <sub>2</sub> (ppm)	Length of simulation (kyrs)
MIO_FW50	~50 km	~1500 m	~960 m	450	2.0
MIO_FW105	~105 km	~1500 m	~960 m	450	2.0
MIO_FW222	~222 km	~1500 m	~960 m	450	2.0
MIO_FW286	~286 km	~1500 m	~960 m	450	2.0
MIO_FW352	~352 km	~1500 m	~960 m	450	2.0
MIO_FW500	~500 km	~1,500 m	~960 m	450	3.3
MIO_280	~500 km	~1,500 m	~960 m	280	1.0
MIO_600	~500 km	~1,500 m	~960 m	600	1.0
MIO_840	~500 km	~1,500 m	~960 m	840	1.0
PI	~670 km	~2,800 m	~1100m	280	5.9

In the reference simulation (MIO\_FW500) an atmospheric CO<sub>2</sub> concentration of 450 ppm is prescribed, with a FS width of ~500 km and fixed gateway depths of ~1500 mbsl. In the Arctic Ocean, the FS represents the only early Miocene gateway of the Arctic Ocean, since other shallow connections to the world's ocean like the Barents Sea, Canadian Archipelago and Bering Strait evolved only after the middle Miocene (Butt et al., 2002; Hutchinson et al., 2019).

Furthermore, the Panama Seaway is not yet closed and connects the Pacific and Atlantic oceans. Also, remnants of the Tethys exist (von der Heydt and Dijkstra, 2006). The model is integrated for 4 kyrs to minimize salinity/temperature trends in the deep ocean after initialisation with present-day conditions. Sensitivity experiments are performed for the FS by varying its width (Table 3). After model integration of 2 kyrs, the final 100 yrs of model simulation is used for analysis.

Starting from a narrow FS width of ~50 km, in a set of six model simulations the ocean gateway is gradually widened to 105, 222, 286, 352 and 500 km, respectively (Table 3). As deepening of the FS between ~2,000 and 1,500 mbsl might be important for the deep-water exchange (Ehlers and Jokat, 2013) the sill depth of FS is always fixed to 1500 mbsl. For minimum FS widths of ~50 km, in principle the ocean gateway is likely wide enough to allow rotationally controlled exchange flows (Pratt and Spall, 2008), as described by the Rossby radius of deformation. However, in the model experiments MIO\_FW50 and MIO\_FW105 with a FS width of ~50 km and ~105 km, its geometry is only represented by one and two zonal grid boxes respectively, owing to, spatial limits in the resolution of the ocean model component. Apart from the FS gateway sensitivity experiments we performed additional simulations at different levels of atmospheric CO<sub>2</sub> (280, 450, 600 and 840 ppm; Table 3) that are within a broad range of reported CO<sub>2</sub> levels representative for the Eocene–Miocene time period (Beerling and Royer, 2011; Pagani et al., 2005; 2011).

## 4.2 Results

### 4.2.1 Ventilation of the Arctic Ocean

For minimum FS widths of ~50 km, our simulation indicates a northward penetration of dense Atlantic waters across a narrow gateway. It establishes a hydraulically controlled outflow of relatively fresh water in the upper layer (Figure S4.1), and a deep inflow of saline and warm Atlantic water. As a result of saltwater exchange across the FS and net Arctic freshwater input (river runoff and net precipitation) via the atmospheric hydrological cycle, a vertical Arctic halocline and salinity gradient establishes. The formation of vertical and horizontal salinity gradients strengthens Arctic gyre circulation following isolines of salinity and causes poorly oxygenated conditions. An inflow of salty North Atlantic waters across the FS perturbs the Arctic stratification as reflected by excursions of the characteristic halocline (Figure 4.1). The

#### 4. Opening of the Fram Strait

vertical separation of Atlantic water inflow with respect to the mixed layer above tends to reduce the amplitude of the halocline and the baroclinic-geostrophic balance of the gyre circulation.

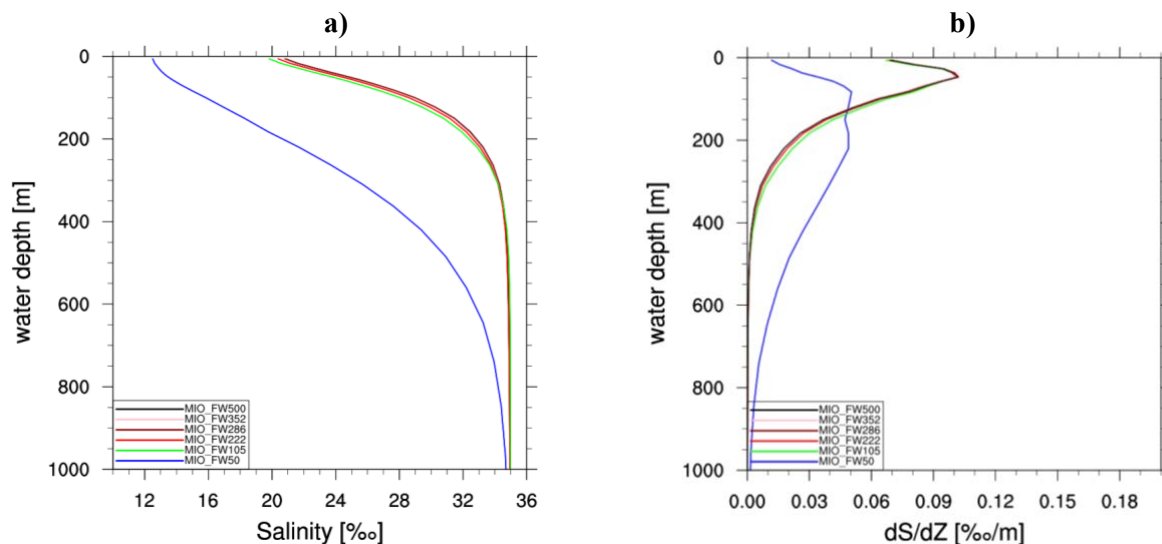


**Figure 4.1.** Impact of gateway width on vertical salinity characteristics in the Arctic Ocean. a) Mean salinity profiles (‰) and b) haloclines ( $dS/dz$ ; ‰/m) of the Arctic Ocean for different FS gateway widths.

By widening the FS from  $\sim 50$  km to  $\sim 105$  km at fixed gateway depths of  $\sim 1500$  mbsl, an unrestricted inflow of Atlantic water to the Arctic is possible and indicated by a prominent unperturbed Arctic halocline (Figure 4.1). We detect the transition towards a bi-directional gateway circulation and ventilation of the Arctic Ocean. It establishes a three-layer exchange flow through the FS that is characterized by vertical differentiation of water masses. The outflow of relatively thin, cold, and low-salinity Arctic water is situated above a compensational inflow of warm and salty North Atlantic water and a cold bottom outflow (Figure 4.2). Due to the enhanced import of saline and oxygen-rich Atlantic water through the FS, the Arctic subsurface waters eventually became saltier and oxygenated (Jakobsson et al., 2007; Thompson et al., 2012). With the establishment of a bi-directional circulation regime and an Arctic halocline (Figure 4.1), the through-flow into the Arctic Basin causes the reorganization towards a ventilated Arctic salinity regime.

#### 4. Opening of the Fram Strait

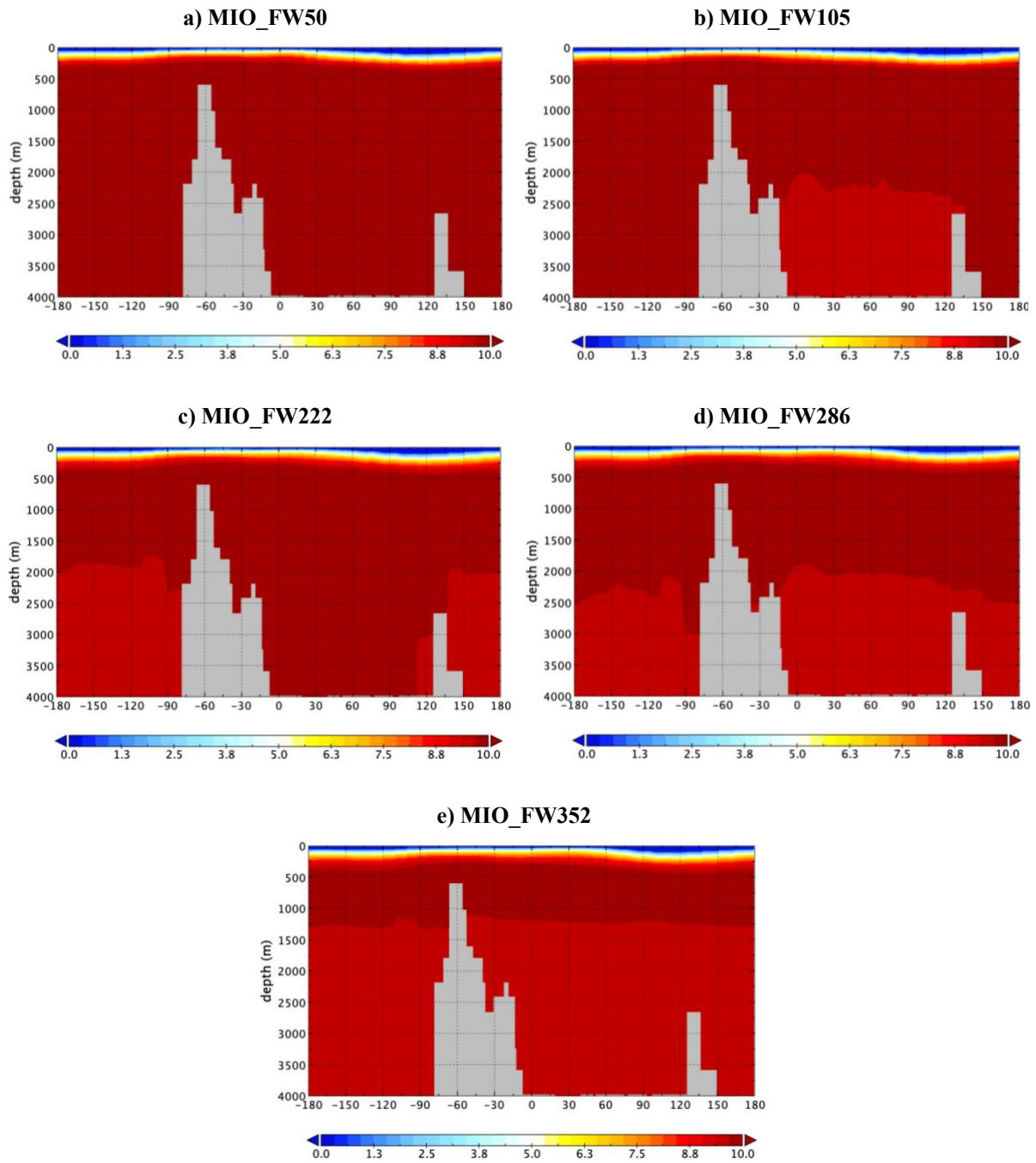


**Figure 4.2.** A cross-section of the Arctic Ocean annual mean temperature (in K) for the model experiments a) MIO\_FW50, b) MIO\_FW105, c) MIO\_FW222, d) MIO\_FW286 and e) MIO\_FW352.

#### 4. Opening of the Fram Strait

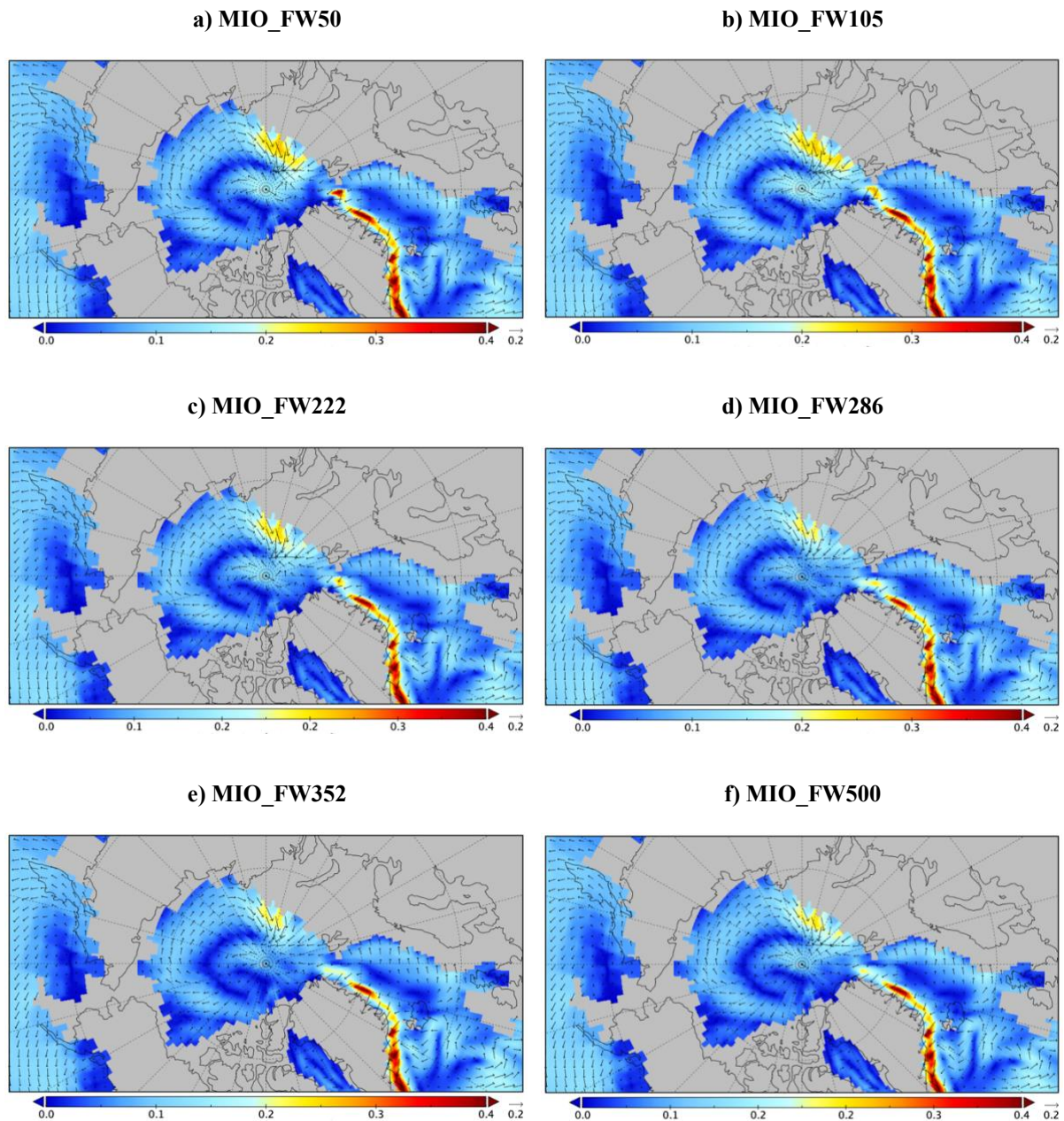


**Figure 4.3.** Ocean velocity at the surface (6 m water depth, m/s) for the experiments of a) MIO\_FW50, b) MIO\_FW105, c) MIO\_FW222, d) MIO\_FW286, e) MIO\_FW352 and f) MIO\_FW500.

Widening of the FS towards  $\sim 286$  km or above further strengthens a more effective cross-sectional water mass transport (Figure 4.3 and 4.4). The strait becomes wide enough that the effect of the Earth's rotation alters the water flow in the upper layer through the FS to a rotationally controlled bi-directional flow, rather than hydraulically controlled and the

#### 4. Opening of the Fram Strait

establishment towards a modern prototype exchange flow. It is characterized by the horizontal differentiation between the southward directed outflow of Arctic Basin at the western continental slope of the strait and the northward directed Atlantic inflow to the East. Although a modern like wide FS gateway configuration allows unrestricted ocean water interchange and thus reducing the Arctic halocline, we still obtain stronger than PI vertical salinity contrasts. This is mainly because of a relatively fresh Arctic surface layer fed by river runoff and net precipitation balanced by salty southern sourced Atlantic water. The total outflow of low-salinity surface water via the FS is greater than the total inflow (Table S4.1). Much of this exchange reflects recirculation within the strait, although parts of it enter the Arctic Ocean and contribute to ventilate deep waters.

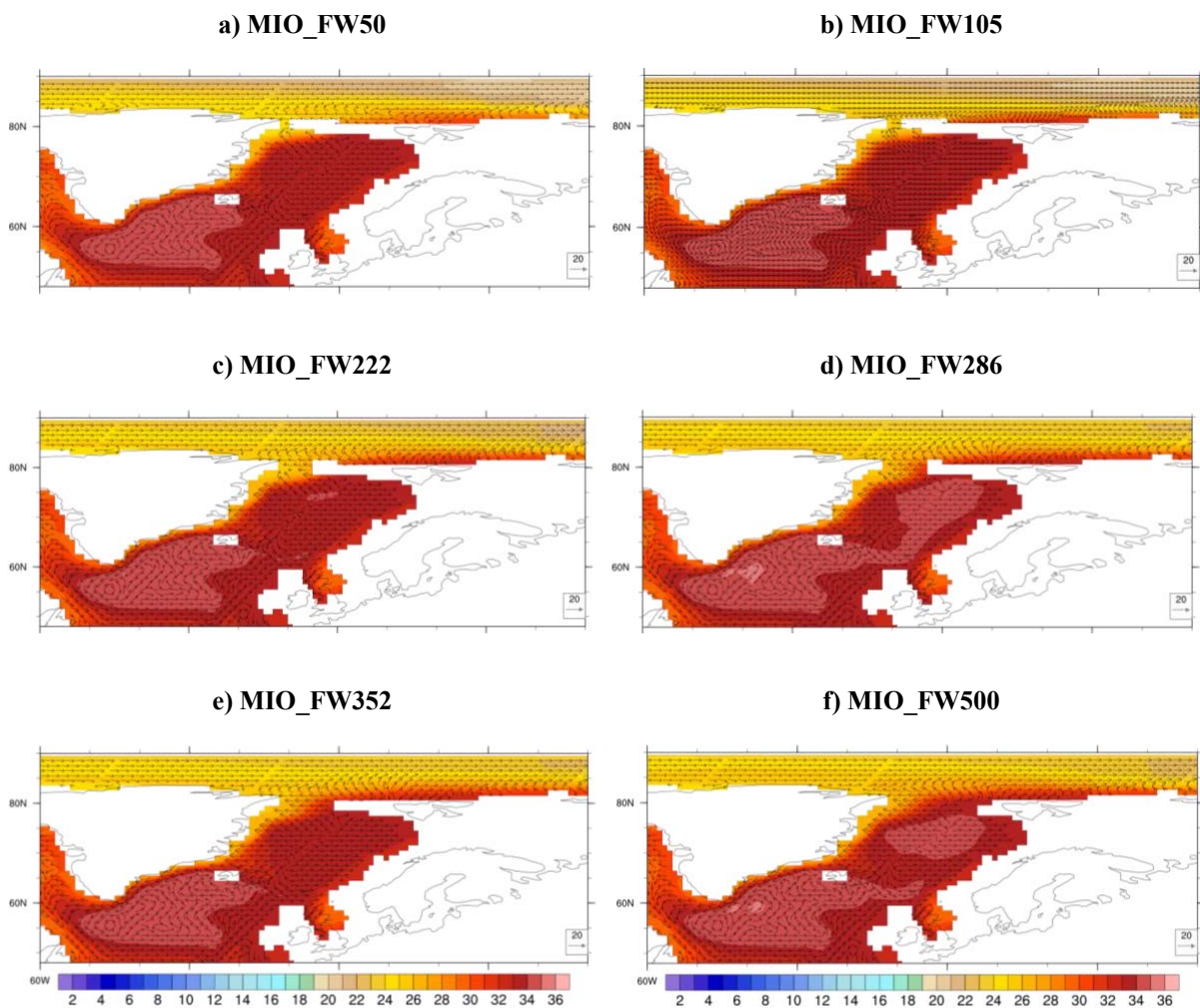


**Figure 4.4.** Salinity and ocean velocity (cm/s) at the water depths of 50 m for the experiments of a) MIO\_FW50, b) MIO\_FW105, c) MIO\_FW222, d) MIO\_FW286, e) MIO\_FW352 and f) MIO\_FW500.

#### *4. Opening of the Fram Strait*

Finally, we calculate the turnover time, which is defined as the ratio of total water volume in the Arctic Ocean to the total outflow through FS (Thompson et al., 2012). In our study, the total volume of water in the Arctic is  $1.6293 \times 10^{16} \text{ m}^3$  and the total outflow through FS is  $1.01 \times 10^6 \text{ m}^3/\text{s}$ . This results into a similar turnover time of  $\sim 512$  yrs, compared to 480 years estimated by Thompson et al. (2012) taken the uncertainties into account.

#### **4.2.2 Stratification in the Arctic Ocean**

In the model experiments MIO\_FW50 at a FS width of  $\sim 50$  km, we detect that the simulated stratification in the Arctic Ocean has a two-layer structure only, with a surface layer of shallow cold and low-salinity water situated above a deep and weakly stratified lower layer (Figure 4.2). The lower layer consists of warmer saline water of Atlantic origin that is advected northward through FS and progressively mixed with the cold low-salinity upper-ocean water. The exchange flow through FS is characterized by vertical separation of water masses, as shown by an outflow of relatively fresh and cold Arctic waters at the surface and a compensational inflow of warm and salty Atlantic waters below. This two-layer stratification of the Arctic Basin is caused by the net freshwater input and the reduced inflow of saline Atlantic water, which deters the possibility of forming a less saline but cold bottom layer.

The two-layer stratification in the Arctic Ocean changes with the widening of the FS and the increasing ocean water mass interchange. In the model experiments MIO\_FW105, MIO\_FW222, MIO\_FW286, MIO\_FW352 and MIO\_FW500 at the FS width of  $\sim 105$ ,  $\sim 222$ ,  $\sim 286$ ,  $\sim 352$  and  $\sim 500$  km (Figures 4.2 and 4.5b), respectively and with a sill depth of  $\sim 1500$  m, a three-layer structure for the Arctic Ocean is established, with a cold bottom layer encountered below the warmer intermediate Atlantic layer.

#### **4.2.3 Effect of CO<sub>2</sub> concentrations on Arctic Ocean stratification**

To test the sensitivity of Arctic Ocean stratification to atmospheric changes, we perform additional simulations at different levels of atmospheric CO<sub>2</sub> concentrations (280–840 ppm), capturing a wide range of greenhouse gas variations representative for the Eocene–Miocene time period (Beerling and Royer, 2011; Pagani et al., 2005; 2011). We choose only a single FS width of  $\sim 500$  km and vary the atmospheric CO<sub>2</sub> (280, 450, 600 and 840 ppm) accordingly. The CO<sub>2</sub> concentration at 450 ppm reflects the standard Miocene configuration that has also been applied for the earlier presented FS gateway sensitivity experiments. The CO<sub>2</sub> level of 280 ppm is typical for pre-industrial (PI) times. Today  $\sim 415$  ppm has been reached.

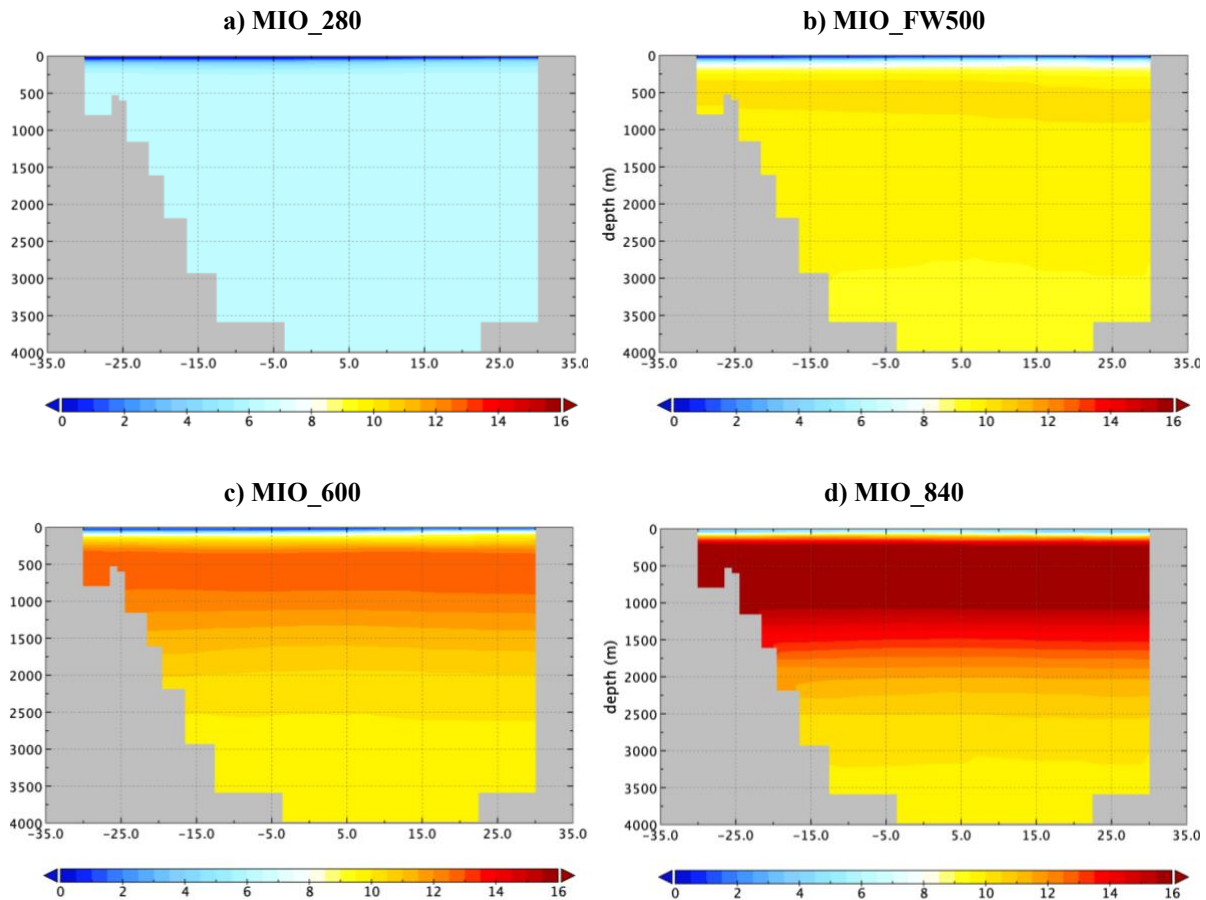


**Figure 4.5.** A cross-section of the Arctic Ocean annual mean temperature (in K) for the model experiments a) MIO\_280, b) MIO\_FW500, c) MIO\_600 and d) MIO\_840.

With the increasing of CO<sub>2</sub> levels, we observe a warming (3–6 °C) (Figure 4.5) in combination with reduced annual mean sea-ice cover in the Arctic Ocean (Figure 4.6). Analyses of gravity cores (Stein et al., 2015) show that the central Arctic Ocean was more or less ice-free during middle to late Miocene summers for 600 and 840 ppm CO<sub>2</sub> levels, whereas sea ice still existed during summers for 278 and 450 ppm CO<sub>2</sub> simulations. We find that the simulated stratification in the Arctic Ocean regime for the model experiments MIO\_280 has a bi-layer structure, with a cold shallow upper layer above a slightly warmer deep-water mass likely of Atlantic origin that extends down to the bottom (Figure 4.5). With the increasing of CO<sub>2</sub> levels to 450 ppm or above (MIO\_FW500, MIO\_600 and MIO\_840) we find 3-layer stratification in the Arctic Ocean, including a cold low-saline bottom layer. This 3-layer structure becomes even more pronounced by increasing the CO<sub>2</sub> level, and is most pronounced at CO<sub>2</sub> levels of 840 ppm (Figure 4.5).

#### 4. Opening of the Fram Strait

Elevated atmospheric CO<sub>2</sub> concentrations enhance the Arctic freshwater budget (Table S4.1). The additional freshwater from the Arctic region is transferred into the Atlantic Ocean, combined with enhanced high latitude warming that reduces deep-water formation. This leads to a slowdown of the Atlantic Meridional Overturning Circulation (AMOC) (Table S4.1). At the FS gateway, particularly the additional Arctic freshwater export linked with the attenuated salt import of northward directed Atlantic waters decreases the baroclinity and overall salinity in the Arctic Ocean (Figure S4.2 and Table S4.1).

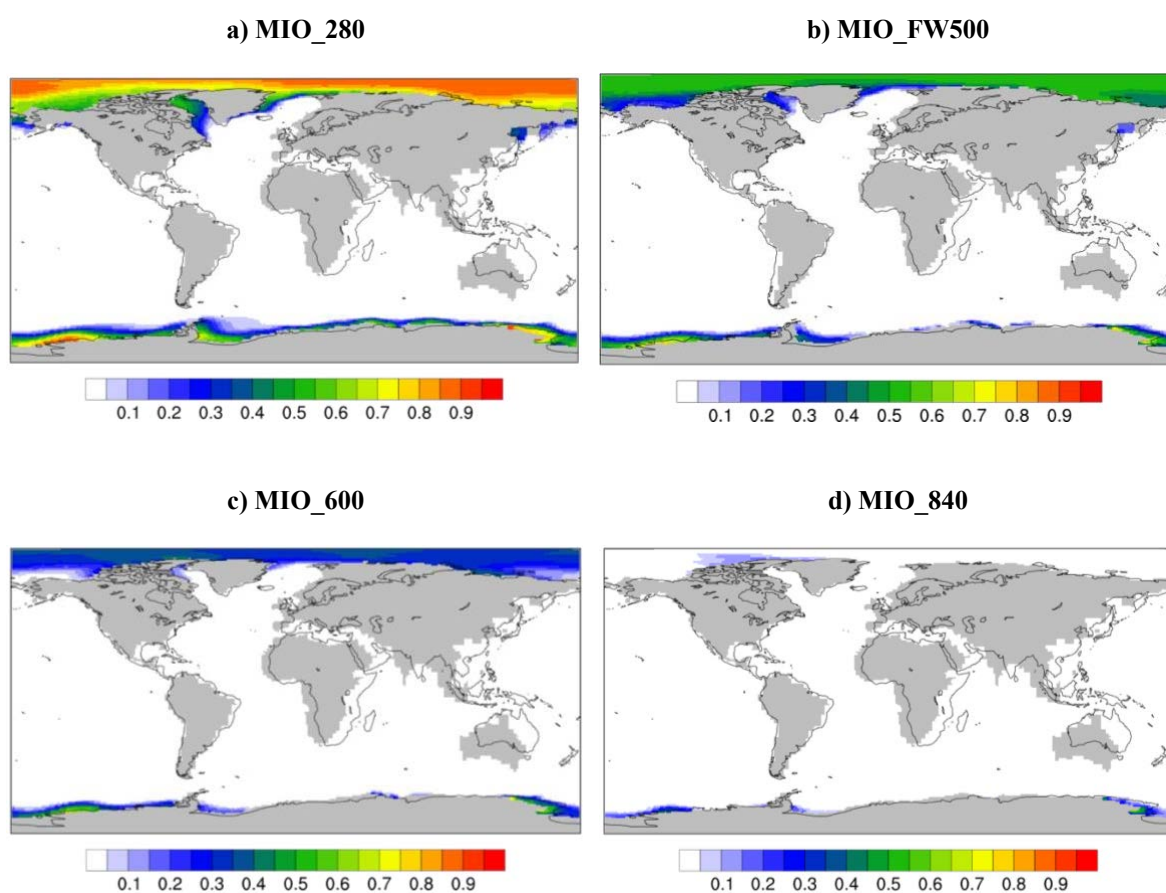


**Figure 4.6.** Annual mean sea-ice cover for the experiments of a) MIO\_280, b) MIO\_FW500, c) MIO\_600 and d) MIO\_840.

#### 4.2.4 Effect of FS widening on the climate

An isolated widening of the FS gateway from  $\sim 50$  to  $\sim 105$  km at fixed gateway depths of  $\sim 1500$  mbsl provides an enhanced inflow of warmer and saltier Atlantic water to the Arctic Ocean and unrestricted water exchange (Figure 4.4a and 4.4b). As a consequence, we detect mild warming (up to  $+1$  °C) but unchanged salinity conditions in the Nordic Seas (Figures 4.7 and 4.8). Arctic temperatures also remain unaltered, but a salinity (up to  $+3$  psu) increase in combination with reduced sea-ice cover is detected (Figure 4.9).

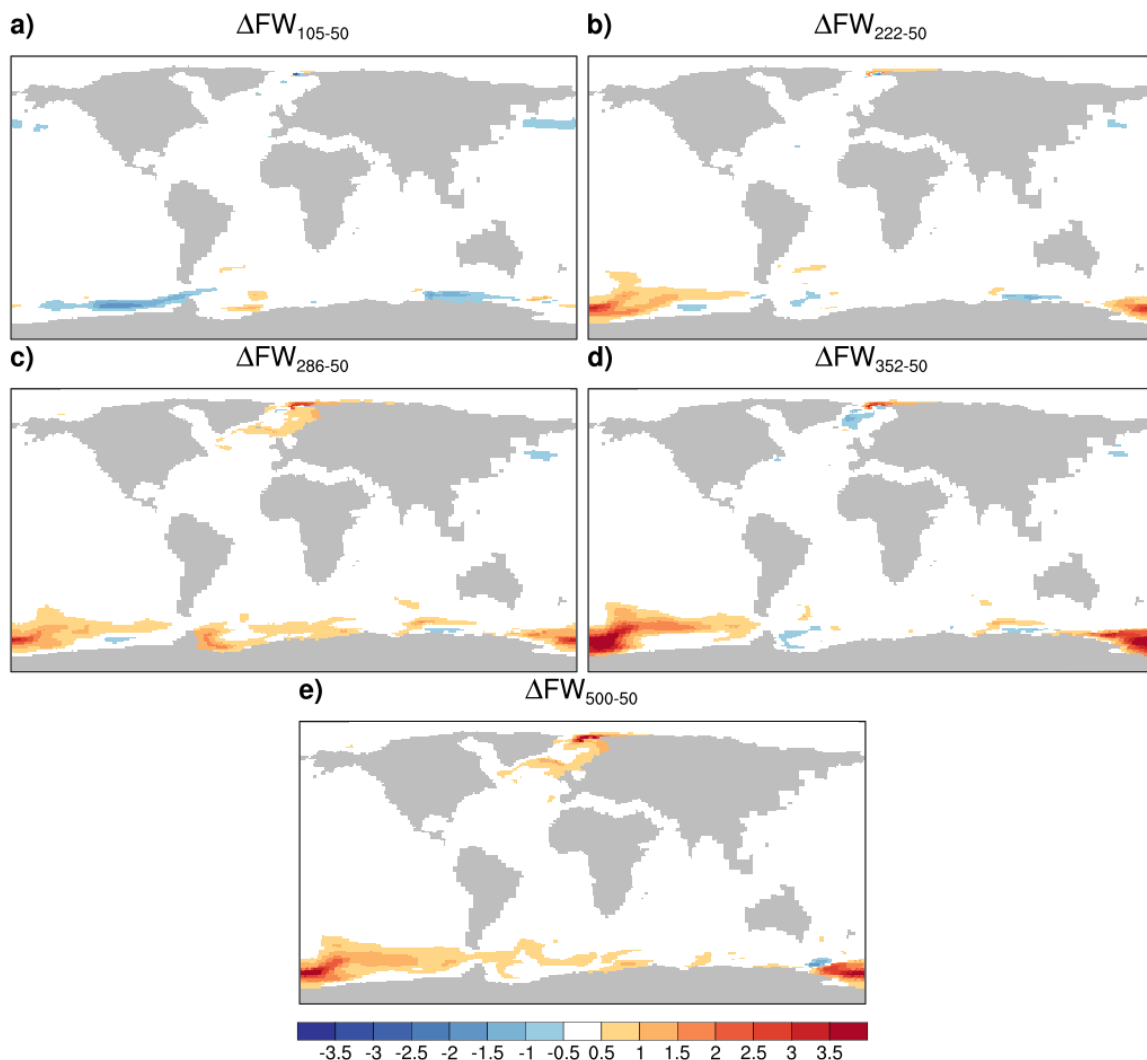


**Figure 4.7.** The effect of a)  $\Delta FW_{105-50}$ , b)  $\Delta FW_{222-50}$ , c)  $\Delta FW_{286-50}$ , d)  $\Delta FW_{352-50}$  and e)  $\Delta FW_{500-50}$  on sea surface temperature anomalies (SST; in °C).

#### 4. Opening of the Fram Strait

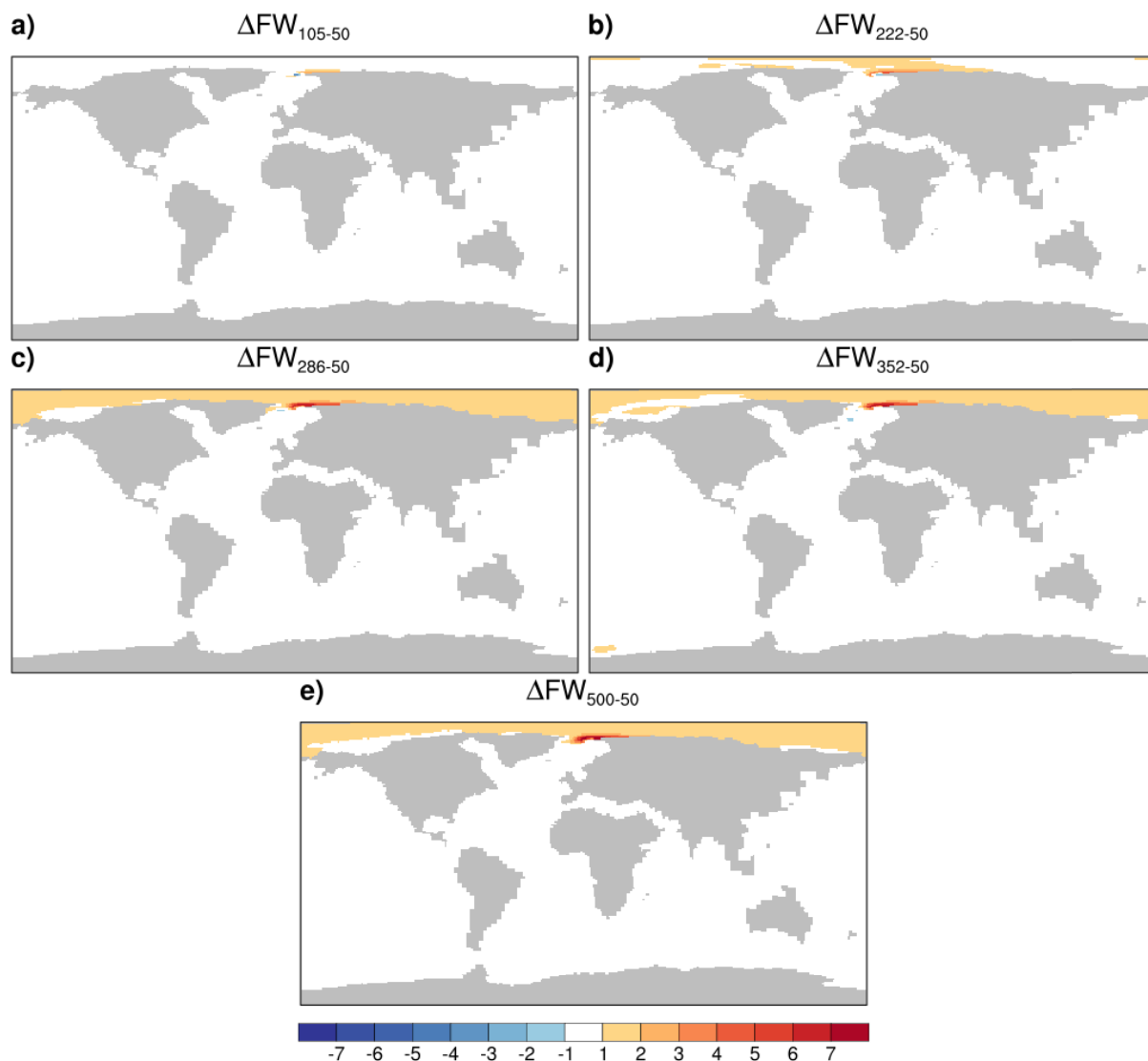


**Figure 4.8.** The effect of a)  $\Delta FW_{105-50}$ , b)  $\Delta FW_{222-50}$ , c)  $\Delta FW_{286-50}$ , d)  $\Delta FW_{352-50}$  and e)  $\Delta FW_{500-50}$  on sea surface salinity anomalies (SSS; in psu).

Progressive widening of the FS gateway from  $\sim 50$  km to  $\sim 500$  km (Table 3) shows the similar basic characteristics in temperature and salinity as widening from  $\sim 50$  to  $\sim 105$  km with stronger magnitudes of change for a wider FS gateway (Figures 4.7 and 4.8). The SSS changes in the Arctic appear to steadily become stronger with the widening of FS gateway. It is caused by the increased inflow of saline Atlantic water through FS which progressively mixed with the low-salinity upper-ocean water.

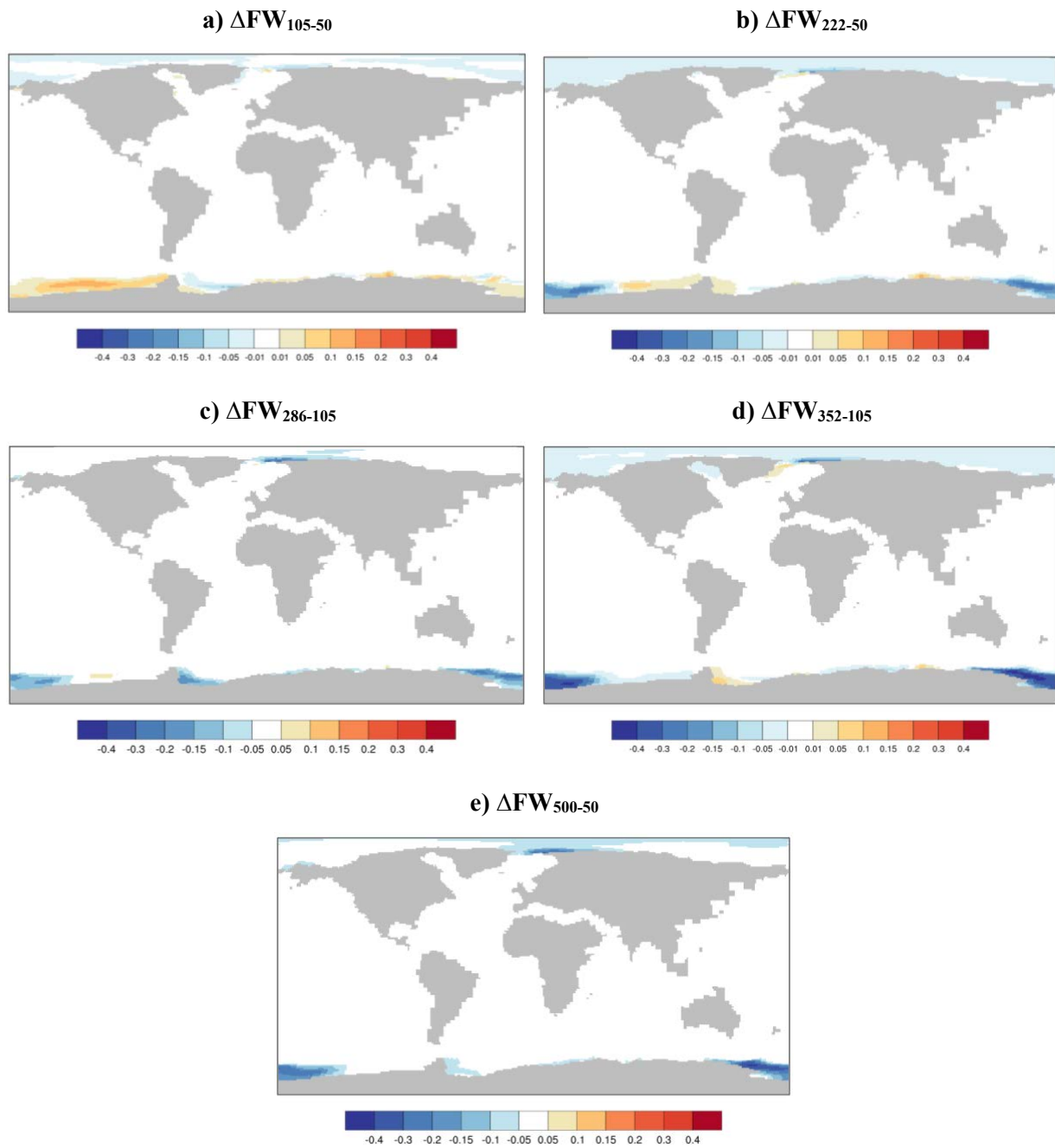


**Figure 4.9.** The effect of a)  $\Delta FW_{105-50}$ , b)  $\Delta FW_{222-50}$ , c)  $\Delta FW_{286-50}$ , d)  $\Delta FW_{352-50}$  and e)  $\Delta FW_{500-50}$  on sea ice concentration anomalies (SIC).

### 4.3 Discussion

The continuous opening of FS is well constrained by magnetic and seismic data (Jokat et al., 2016) that show oceanic crust in the FS might have been formed after ~24 Ma (Ehlers and Jokat, 2013). Thus, during this initial opening phase, a shallow water exchange between the Arctic Ocean and the North Atlantic (Jokat et al., 2008; Hegewald and Jokat, 2013) is likely. Both, plate kinematics models and geophysical data (Engen et al., 2008; Jokat et al., 2016) indicate that the opening of FS started earlier than suggested by previous paleo-oceanographic studies (Myhre et al., 1995) based on micropaleontology and biostratigraphy. With time, the FS widened as a result of a large strike-slip movement between Svalbard and Greenland. A paleo-bathymetric model based on magnetic and regional seismic data (Ehlers and Jokat, 2013) shows that the first deep-water exchange between the Arctic Basin and the Nordic Seas was likely between ~17 and 20 Ma. According to this model, the FS deepened to sill depths >1,500 mbsl at ~17 Ma. A paleo-bathymetric reconstruction indicates the transition to a fully ventilated Arctic Ocean at around 17.5 Ma allowing an unrestricted exchange of warm and saline Atlantic water and colder Arctic water (Moran et al., 2006; Jakobsson et al., 2007). The ventilation was achieved in a relatively short period, since the drill cores show an abrupt change to modern sedimentation at that time instant. According to the age–width estimation using geophysical data and a recent paleobathymetric model (Straume et al., 2020) yields similar results. The FS began to deepen in the early Miocene and reached modern depths (>2,000 m) by the middle Miocene (13.7 Ma; Jakobsson et al., 2007).

The simulated climate shows a global warming that matches the global mean temperature reconstruction (Goldner et al., 2014) suggesting warming (+6 °C) with respect to PI conditions (Stärz et al., 2017). The Arctic Ocean was also relatively warm with temperatures of about 8.4–9.2 °C (Table S4.1). This is directly supported by the early Miocene (~18.2 Ma) sediments recovered from the Lomonosov Ridge (IODP Exp 302) during ACEX indicate SST of ~10 °C (Weller and Stein, 2008). This also agrees with oxygen isotope analyses of fishbone carbonate (Waddell and Moore, 2008) in the ACEX cores provided a salinity of about 35 psu and temperatures of about 6 °C for the early Miocene. Stein et al. (2016) found alkenone-derived SST of ~8.9 °C in the central Arctic Ocean during late Miocene (~7.5 Ma; Table S4.2). Observational data based on a combination of satellite and direct measurements (IPCC, 2013; USEPA, 2016) show a warming (~0.5–1.5 °C) in the Nordic Seas with a CO<sub>2</sub> rise from ~300–

#### 4. Opening of the Fram Strait

400 ppm between 1901 and 2015 (GISS, 2020; NASA, 2020). In our Miocene simulation with increasing CO<sub>2</sub> levels from 280 to 450 ppm, we observe warmer (~2.5–4.5 °C) Nordic Seas (Figure S4.3). In general, our simulations could reproduce a warmer than present-day Arctic Ocean during the Miocene (Zachos et al., 2001; Björk et al., 2007) with a stronger hydrological cycle (Table S4.1; Held and Soden, 2006).

The geometrical widening of the FS could have been important for climate and global ocean circulation by influencing the production of NADW, initiating and intensifying the AMOC (Figure 4.10; Jakobsson et al., 2007; Knies and Gaina, 2008; Knies et al., 2014; Hutchinson et al., 2019). The transition from poorly oxygenated towards fully ventilated (oxygenated) Arctic Ocean, characterized by a warmer ocean with higher salinities, as suggested by sediment records from the Lomonosov Ridge (ACEX core analyses), has been attributed to the opening of FS (Moran et al., 2006; Jakobsson et al., 2007; Waddell and Moore, 2008).

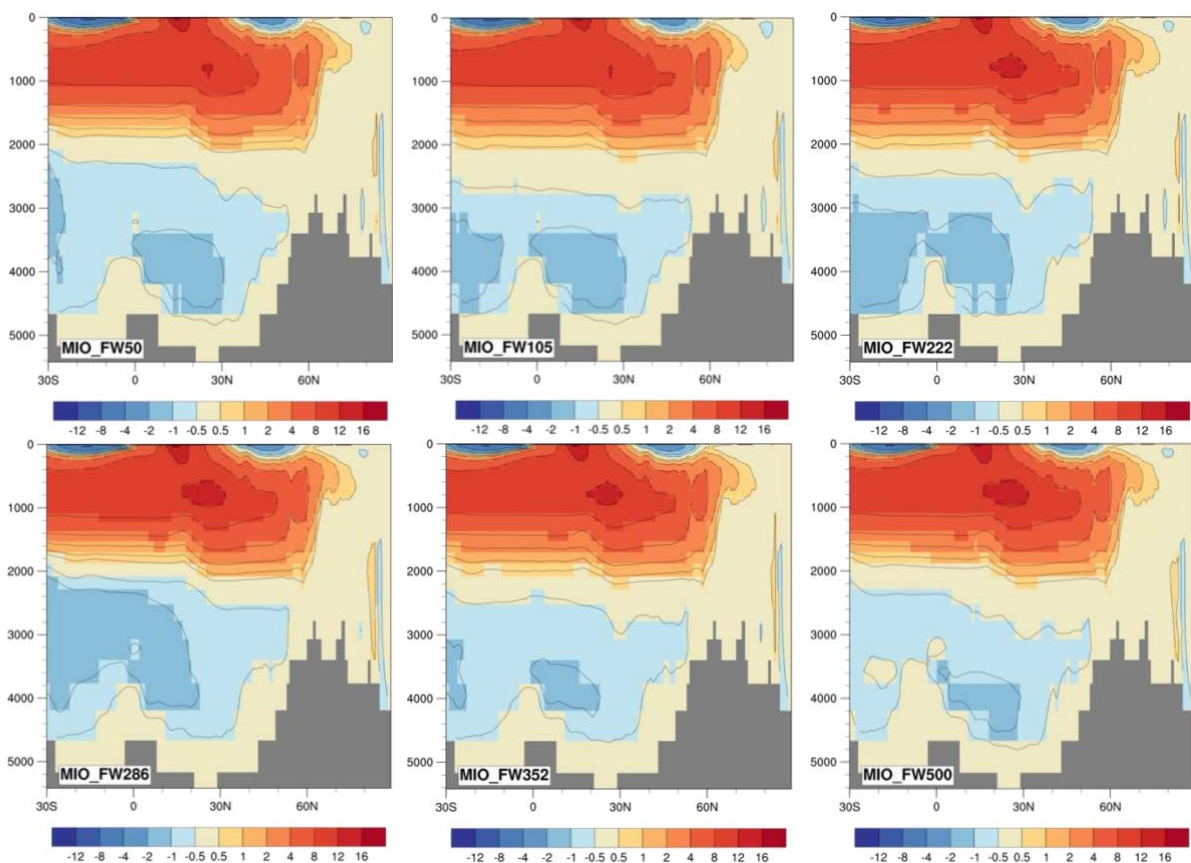


**Figure 4.10.** Atlantic Meridional Overturning Circulation (AMOC) for the experiments of MIO\_FW50, MIO\_FW105, MIO\_FW222, MIO\_FW286, MIO\_FW352 and MIO\_FW500.

#### *4. Opening of the Fram Strait*

In our numerical simulations, we have achieved a ventilated Arctic Ocean with a width of ~105 km. This agrees with the findings of previous studies (Thompson et al., 2010; 2012), although they have applied a shallower FS sill depth (1000 m) than used in our study (~1500 m) in order to induce ventilation. Hence, we do not expect a big difference to Thompson et al. (2010; 2012) from the point of ventilation changes if we would apply a similar depth. Furthermore, we used a fully-coupled Earth System Model including feedbacks in the atmosphere-ocean-land system. Hence, the similarity of the dynamics of Arctic ventilation in response to FS widening in Thompson et al. (2010; 2012) and our study highlights the importance of an oceanic control. A narrowing of the FS in the late Miocene by the Hovgård Ridge (Knies et al., 2014) might not have had a large impact as long as the remaining width was more than 100 km. The ventilation of the Arctic Ocean is established by inflow through FS of North Atlantic originated deep-water and injection of brine-enriched dense shelf waters (Rudels, 1995; Rudels et al., 2005). We estimate a turnover time of ~512 yrs in our study which is similar to the time estimated in Thompson et al. (2012).

Our model experiments with a FS width at around 105 km or more show a three-layer structure of Arctic stratification, with a colder shallow upper layer above a warmer intermediate layer of Atlantic origin and a relatively less warm bottom layer. The present-day Arctic Ocean also has a three-layer stratification, which depends crucially on temperature variations, the sea ice formation on the shelves and wind forcing (Rudels, 1995; Rudels et al., 2005). The exchange flow through FS shows a 3-layer structure with a thin upper layer of low salinity cold outflow from the Arctic Ocean, an intermediate inflow of saline and warmer water from the Atlantic Ocean below and a cold bottom layer of Arctic origin. However, it is in contrast to the findings of previous studies (Thompson et al., 2010; 2012) which found a two-layer stratification using a Miocene bathymetry.

At the wider FS gateway, warmer Atlantic water flushes the intermediate depths and progressively mixed with the cold low-salinity upper-ocean water and bottom layer. It causes a gradual nonlinear salinity increase (up to +2 psu) and warming (up to +1 °C) in the Arctic Ocean. The flow of warm waters from the North Atlantic enters the Nordic Seas and Arctic Basin through FS, mostly between 200 m depth and the mixed-layer (Figures 4.2 and 4.5), leading to substantial warming in the Arctic Ocean (Herold et al., 2012). This nonlinear salinization process and warming control the stratification.

Elevated atmospheric CO<sub>2</sub> enhances the Arctic freshwater budget, warming (Table S4.1) and a more accentuated halocline (Stärz et al., 2017). An intensified stratification is established by

an enhanced atmospheric hydrological cycle with increased river runoff and net precipitation (precipitation minus evaporation) in the Arctic Ocean (Table S4.1; Moran et al., 2016) that tends to freshen the relative fresh Arctic surface waters (Stärz et al., 2017). The lack of relatively saline inflow through the FS might also contribute to Arctic sea-surface freshening during the Miocene (Herold et al., 2012). Below the Arctic freshwater layer, there are the southern sourced North Atlantic waters, which cause an increase in salinity and temperature due to high evaporation in the low latitudes.

In the northern hemisphere, simulated annual sea-ice concentrations are significantly higher for large parts of the Arctic when FS was narrow and CO<sub>2</sub> levels low (Figures 4.6 and 4.9), which was due to cooler mixed-layer temperatures in combination with weaker NADW formation (Herold et al., 2012). Conversely, sea-ice decreases for a wider FS gateway and higher CO<sub>2</sub> levels. A perennial Arctic sea-ice cover likely occurred from the middle Miocene onwards (Woodruff and Savin, 1989; Darby, 2008; Krylov et al., 2008; Moran et al., 2016). These data are in contrast to geological analyses (Stein et al., 2015) that show ice-free warmer summer conditions in the Arctic Ocean during the middle to early late Miocene. Sea-ice proxy records suggest Arctic sea-ice cover was modest between 17.5–16 Ma and more prevalent following and prior to this time period (St. John, 2008). There is likely excessive Arctic sea-ice in our Miocene simulation (Herold et al., 2012).

The relatively short ventilation time is supported by the abrupt changes in sediment composition in the ACEX core analyses (Jakobsson et al., 2007). Although FS is fairly shallow and narrow in our Miocene simulations, the resulting ventilation timescales seem to be shorter than or comparable to corresponding estimates based on chemical tracer studies (Schlosser et al., 1997; Tanhua et al., 2009) in the present-day Arctic Ocean. In general, the current model reproduces geological observations on the climate conditions of the Arctic Ocean. Our model simulations do not show dramatic changes in the global circulation pattern and global climate questioning the role of the FS in triggering/enabling the Northern Hemisphere Glaciations (NHG) during early to middle Miocene. Several studies have proposed the closure of the Panama Seaway (Marshall et al., 1982; Webb, 2006), a decline in atmospheric CO<sub>2</sub> (Lunt et al., 2008; Bartoli et al., 2015; Seki, 2010), and tectonic uplift of plateaus and mountains in the high northern latitudes (Knies et al., 2014) are the important factors for the onset and intensification of the NHG during the Pliocene around 2.7 Ma (Haug et al., 2001; Lear et al., 2003; Ruddiman, 2010; Knies et al., 2014).

## **4.4 Conclusions of Chapter Four**

By means of an Earth System Model, we have qualitatively analysed the impact of FS opening in controlling ventilation of the Arctic Ocean during early to middle Miocene in different model experiments. We explore the role of the FS width and CO<sub>2</sub> concentrations in the establishment of the modern-like stratification in the Arctic Ocean and exchange flow through FS. Our simulations show that a progressive widening of the FS causes unaltered salinity conditions and a mild warming in the Nordic Seas. Arctic water temperatures remain unaltered and salinity changes appear to steadily become stronger. For a sill depth at around 1500 m, we have achieved ventilation of the Arctic Ocean regime with a FS width of ~105 km. At this depth and width at around 105 km or more, we observe a modern-like three-layer stratification in the Arctic Ocean, with a shallow surface layer of cold and low-salinity water situated above a deep and warmer layer of Atlantic origin and a cold bottom layer. The exchange flow through FS also shows a 3-layer structure. The ventilation mechanisms and stratification in the Arctic Ocean simulated in our study using a significantly shallower and narrower FS during early Miocene, are comparable to the present-day ocean basin. In general, our model reproduces geological observations on the climate conditions of the Arctic Ocean. However, the simulations do not show dramatic changes in the global circulation pattern and global climate questioning the role of the FS in triggering/enabling the NHG.

In future studies, the presented framework might be a good tool to interpret high-resolution sediment records and data from up-coming drilling projects that target the past climate evolution in the North Atlantic-Arctic sector.

## 4.5 Appendix

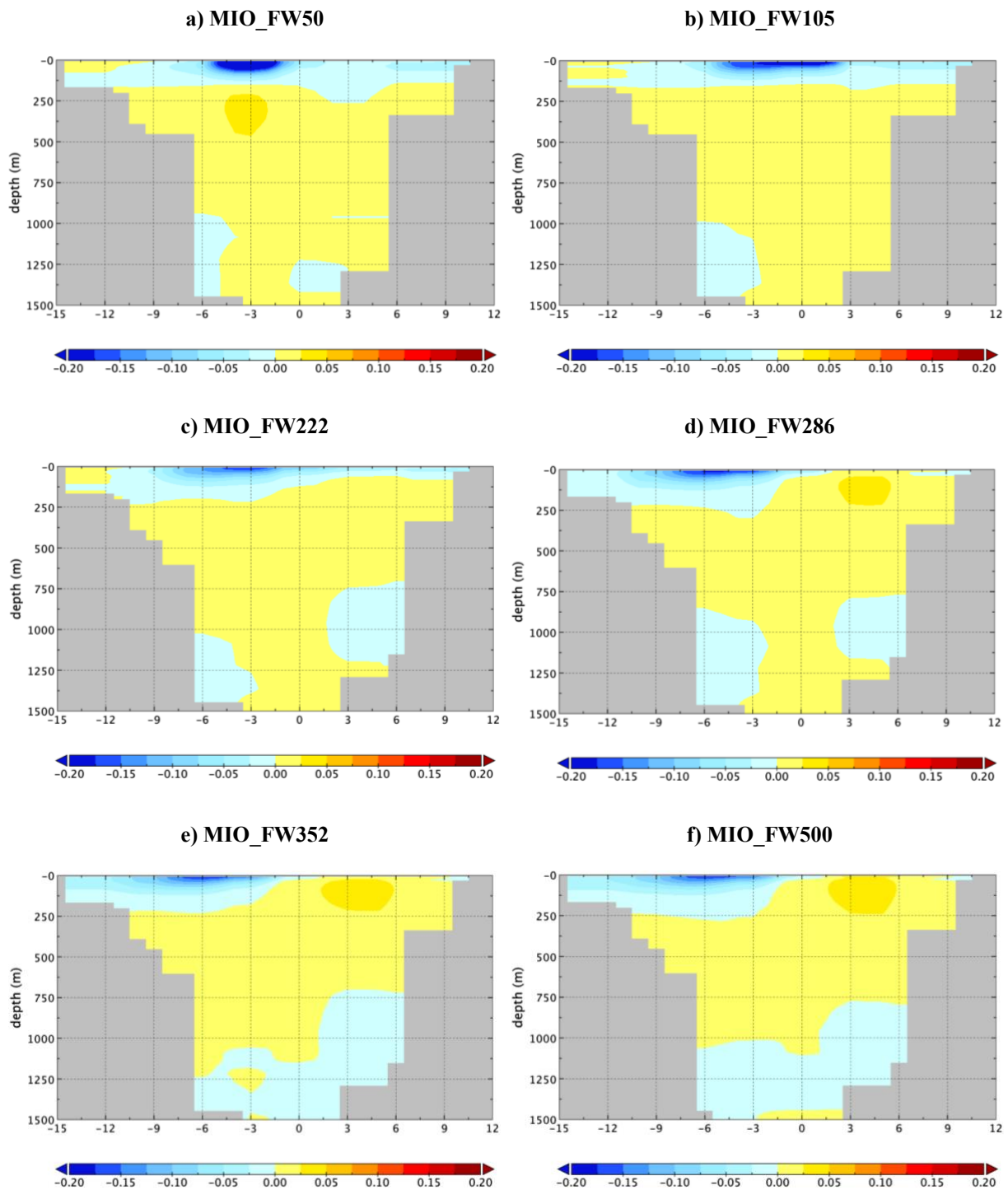


**Figure S4.1.** Ocean velocity at the Fram Strait ( $79.5^{\circ}\text{N}$ ; pos. northward, neg. southward, m/s) for the experiments of a) MIO\_FW50, b) MIO\_FW105, c) MIO\_FW222, d) MIO\_FW286, e) MIO\_FW352 and f) MIO\_FW500.

#### 4. Opening of the Fram Strait

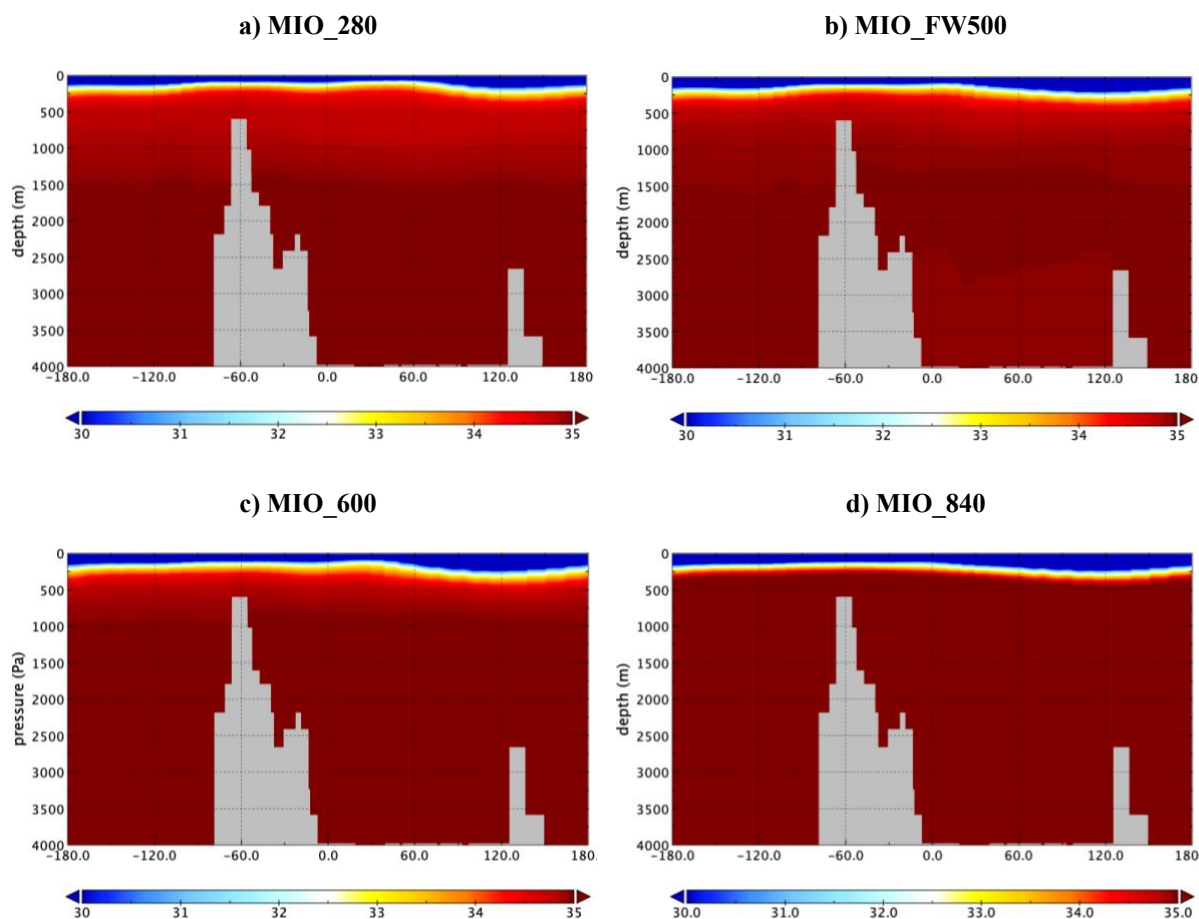


**Figure S4.2.** A cross-section of the Arctic Ocean annual mean salinity (in psu) for the experiments of a) MIO\_280, b) MIO\_450, c) MIO\_600 and d) MIO\_840.

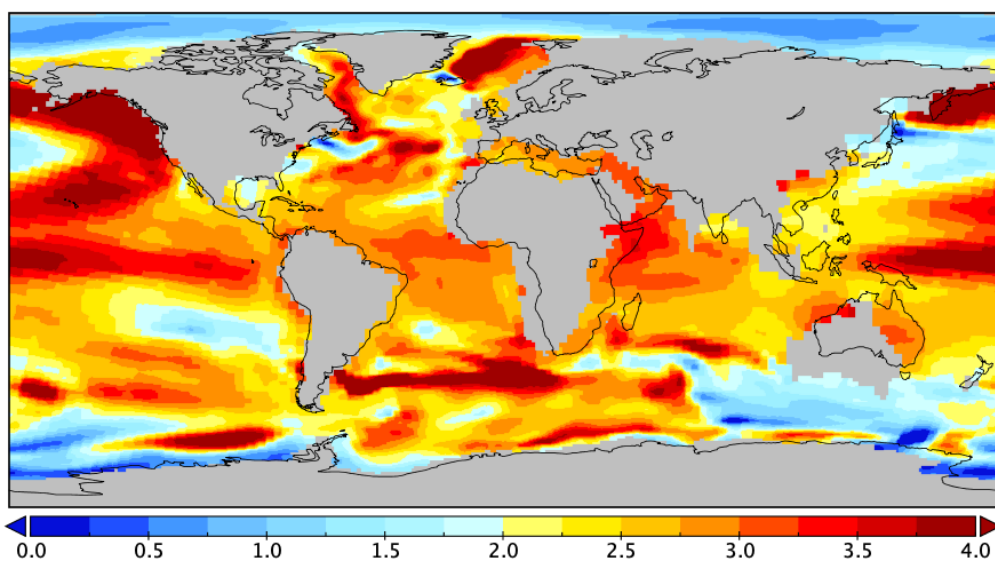


**Figure S4.3.** The sea surface temperature anomalies for  $\text{CO}_2$  changes from 280 to 450 ppm (SST; in  $^{\circ}\text{C}$ ).

**Table S4.1:** Key Diagnostics of different model simulations.

Exp. ID	Fram Strait inflow (into the Arctic Ocean; Sv)	Fram Strait outflow (Sv)	Integr. net freshwater flux into Arctic (Sv)	Mean salinity of Arctic Ocean (‰)	Mean temperature of Arctic Ocean (°C)	Mean SSS Arctic Ocean (‰)	Mean SST Arctic Ocean (°C)	AMOC Index (30-60 °N, Sv)	Global AABW Index (60-80 °S, Sv)
MIO_FW50	0.67	-0.92	0.50	31.7	8.4	19.4	0.21	14.0	-1.66
MIO_FW105	0.76	-1.01	0.50	33.6	9.2	19.8	0.27	14.2	-1.89
MIO_FW222	0.84	-1.08	0.50	33.6	9.1	20.4	0.37	14.2	-2.17
MIO_FW286	0.97	-1.22	0.50	33.6	9.1	20.8	0.43	14.4	-1.88
MIO_FW352	1.01	-1.24	0.50	33.6	9.0	20.8	0.36	13.9	-1.60
MIO_FW500	1.12	-1.35	0.50	33.6	9.1	20.8	0.50	14.4	-1.43
MIO_280	1.04	-1.22	0.40	33.8	6.0	22.7	-0.85	14.4	-3.22
MIO_600	1.15	-1.40	0.56	33.6	10.4	20.2	1.78	12.0	-0.56
MIO_840	1.19	-1.48	0.63	33.8	12.5	19.4	5.27	9.64	-0.74
PI	1.17	-3.85	0.25	34.7	2.2	31.3	-0.28	15.6	-4.06

\* Integrated net freshwater flux = net precipitation + river runoff

**Table S4.2:** Compilation of sea surface temperatures of Miocene time interval from marine records in the Arctic Ocean.

Location	Expedition, core	Latitude (°N)	Age (Ma)	Epoch	Method	SST (°C)	Reference
Lomonosov Ridge	IODP Exp 302, ACEX	87.9	18.2	Early Miocene	U <sup>k</sup> <sub>37</sub>	10	Weller and Stein (2008)
Lomonosov Ridge	IODP Exp 302, ACEX	87.9	18	Early Miocene	TEX86	19.7	Sangiorgi et al. (2008)
Lomonosov Ridge	IODP Exp 302, ACEX	87.9	18	Early Miocene	U <sup>k</sup> <sub>37</sub>	13	Weller and Stein (2008)
Lomonosov Ridge	IODP Exp 302, ACEX	87.9	17.9	Early Miocene	d <sup>18</sup> O	6	Waddell and Moore (2008)
Lomonosov Ridge	IODP Exp 302, ACEX	87.9	11.5	Late Miocene	U <sup>k</sup> <sub>37</sub>	10.5	Stein et al. (2016)
Lomonosov Ridge	IODP Exp 302, ACEX	87.9	9.1	Late Miocene	U <sup>k</sup> <sub>37</sub>	15.5	Stein et al. (2016)
Lomonosov Ridge	IODP Exp 302, ACEX	87.9	7.5	Late Miocene	U <sup>k</sup> <sub>37</sub>	8.9	Stein et al. (2016)
Lomonosov Ridge	IODP Exp 302, ACEX	87.9	6	Late Miocene	U <sup>k</sup> <sub>37</sub>	5.4	Stein et al. (2016)
Lomonosov Ridge	PS87/106	81.2	6–9	Late Miocene	U <sup>k</sup> <sub>37</sub>	4–7	Stein et al. (2016)

#### *4. Opening of the Fram Strait*

Chapter  5

# The Impact of Different Atmospheric CO<sub>2</sub> Concentrations on Large Scale Miocene Temperature Signatures

In this chapter the state-of-the-art fully coupled Earth System Model AWI-ESM2.1 (Sidorenko et al., 2019) is applied to investigate the effect of newly and enhanced Miocene on-/offshore topographic information on the climate sensitivity at different atmospheric CO<sub>2</sub> concentrations. The model simulation uses a high-resolution global Miocene bathymetric and topographic reconstruction (Paxman et al., 2019; Hochmuth et al., 2020a; Straume et al., 2020), which captures the major paleobathymetric features (such as ocean ridges, plateaus and margins) and mountain ranges in the paleotopography of the continents (e.g., the Andes). In the model experiments, the breakdown of seasonality for different background climate is evaluated.

*Declaration: this chapter has been submitted for publication in *Paleoceanography and Paleoclimatology* (Hossain et al., 2022).*

## **5.1 Model setup and experimental design**

### **5.1.1 Paleobathymetry and Paleotopography**

The model setup (AWI-ESM2.1) is based on Middle Miocene time period (~14 Ma) comprising the combined high-resolution (0.1° x 0.1°) global paleobathymetry and paleotopography of Straume et al. (2020), Hochmuth et al. (2020a) and Paxman et al. (2019) (Figure 5.1). Paleobathymetry at latitudes south of 30°S is reconstructed following the paleobathymetric reconstruction of Hochmuth et al. (2020a), using sediment backstripping (Steckler & Watts, 1978). It is based on the reconstruction by Straume et al. (2020) and includes a suite of new paleobathymetric grids of the Southern Ocean. Hochmuth et al. (2020b) merged the Southern Ocean (Hochmuth et al., 2020a) and Antarctic bathymetry/topography (Paxman et al. 2019). This Antarctic median topography is the most recent reconstruction with a resolution of approximately 5 km. The northern part (north of 30°S) of the grids uses the paleobathymetric reconstruction of Straume et al. (2020). The transition between the grids is smoothed to avoid artificial abrupt changes in the bathymetry.

Straume et al. (2020) have re-evaluated the evolution of the Northern Hemisphere oceanic gateways (i.e., the Fram Strait, Greenland-Scotland Ridge, the Central American Seaway, and the Tethys Seaway) and embedded their tectonic histories in a new global paleobathymetry and paleotopography model. The model implements updated plate kinematics, oceanic lithospheric ages, estimated sediment thickness, and paleodepths of oceanic plateaus and microcontinents.

### **5.1.2 Experimental design**

In our reference Miocene simulation (MIO\_450) we prescribe an atmospheric CO<sub>2</sub> concentration of 450 ppm. We implement a high-resolution paleobathymetry and paleotopography of the Middle Miocene. The Fram Strait represents a single ocean gateway control towards the Arctic Ocean (Butt et al., 2002). The North Atlantic gateways are wide enough (GSR depth: ~410 m and FS depth: ~2400 m; width: ~420 km; Table 4) to maintain rotationally controlled flows across the gateways. Other ocean gateways like the Canadian Archipelago, Bering Strait, Tethys through-flow and Barents Sea evolved after the Middle Miocene. Moreover, the Panama Seaway still connects the Pacific and Atlantic Oceans. In our Miocene setup the Greenland ice sheet is absent, whereas the height of the Antarctic ice sheet and the Miocene orography (East Africa, Andes, Rocky Mountains, Tibetan Plateau) are

## 5. The Impact of Different Atmospheric CO<sub>2</sub>

reduced compared to PI. The orbital parameters are kept constant at PI values. We initialise the ocean from a constant temperature (3.5 °C) and salinity (34.7 psu).

### Paleobathymetry and Paleotopography

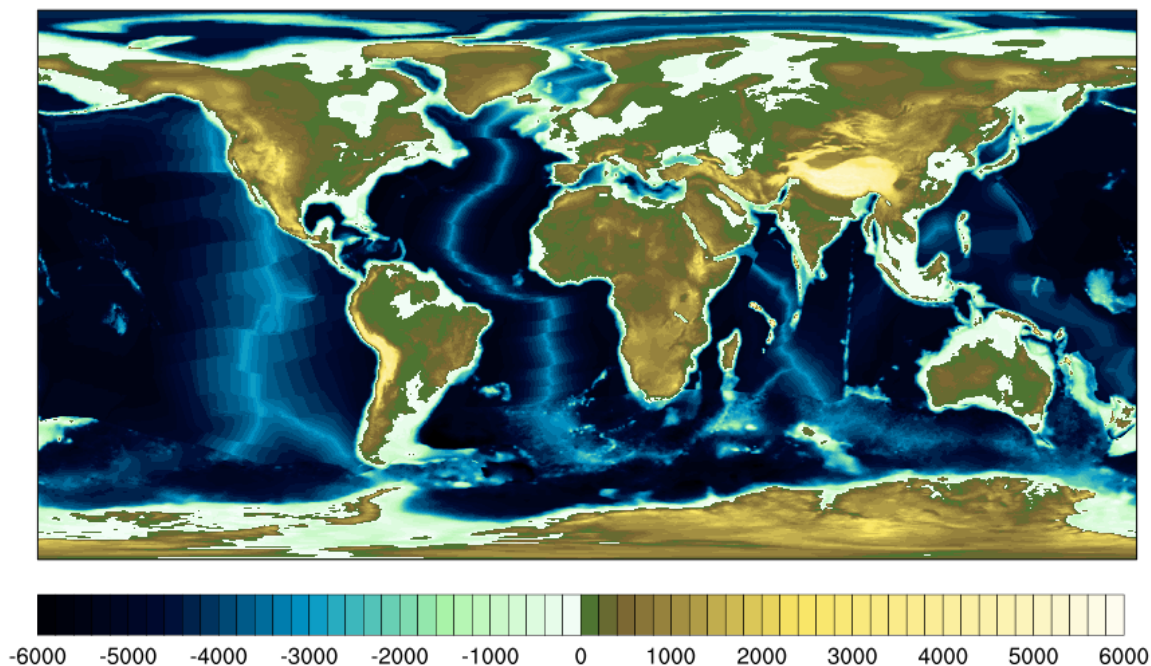


**Figure 5.1.** Global compilation of Middle Miocene paleobathymetry and paleotopography (in m) (Paxman et al., 2019; Hochmuth et al., 2020a; Straume et al., 2020).

We perform the model simulations PI\_CTRL using an atmospheric CO<sub>2</sub> concentration of 280 ppm and PI boundary conditions (ocean bathymetry and topography, orbital forcing, vegetation and ice sheet topography) and initialized from three-dimensional PI ocean salinity and temperature fields of the Polar science center Hydrographic Climatology (PHC; Steele et al., 2001).

In order to analyze the relative importance of boundary conditions and CO<sub>2</sub> concentrations as forcing factors we have run three additional simulations MIO\_280, MIO\_720 and PI\_450, respectively (Table 4). We apply the same CO<sub>2</sub> concentration for the simulation MIO\_280 as PI\_CTRL, but with Miocene boundary conditions. Simulation PI\_450 adopts the same boundary conditions as PI\_CTRL, while it is run with a higher CO<sub>2</sub> concentration of 450 ppm. In order to analyze the effect of boundary conditions, their complex interactions and synergy between them, we utilized a factor separation analysis (Stein & Alpert, 1993). After model integration of at least 1 kyrs, climatological mean values of the final 100 yrs of model output

## 5. The Impact of Different Atmospheric CO<sub>2</sub>

is used for analysis (Figure S5.1). The model simulations are evaluated with available proxy data.

**Table 4:** List of sensitivity experiments including relevant model parameters.

<b>Model Exp.</b>	<b>max. GSR depth (m)</b>	<b>max. Fram Strait depth (m)</b>	<b>Bathymetry &amp; topography</b>	<b>Atmos. CO<sub>2</sub> (ppm)</b>	<b>Length of simulation (kyrs)</b>
MIO_280	~410 m	~2,400 m	Middle Miocene	280	1.0
MIO_450	~410 m	~2,400 m	Middle Miocene	450	1.0
MIO_720	~410 m	~2,400 m	Middle Miocene	720	1.0
PI_CTRL	~1,100 m	~2,800 m	PI	280	1.0
PI_450	~1,100 m	~2,800 m	PI	450	1.0

## 5.2 Results

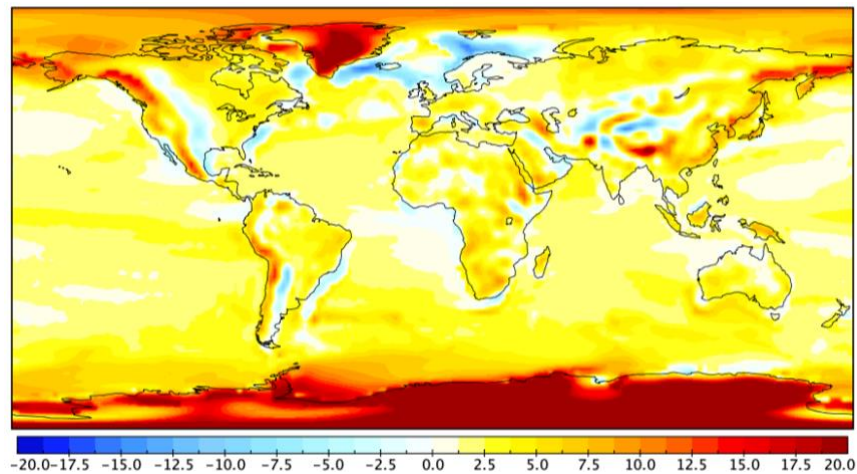
### 5.2.1 Effect of Miocene boundary conditions

In experiment MIO\_450 with Miocene boundary conditions, we simulate a mean surface air temperature of ~16.4 °C, which is warmer (~3.0 °C) than the preindustrial climate (PI\_CTRL, ~13.4 °C). The simulated Miocene climate shows a reduced sea-ice cover, increased water vapour, river runoff and precipitation (Figure 5.2 and Table S5.1). The spatial temperature changes between MIO\_450 and PI\_CTRL are heterogeneous (Figure 5.2a). In combination with ice-albedo changes (Figure 5.2b and 5.2c), the resulting temperature variation is largely pronounced in the high-latitudes.

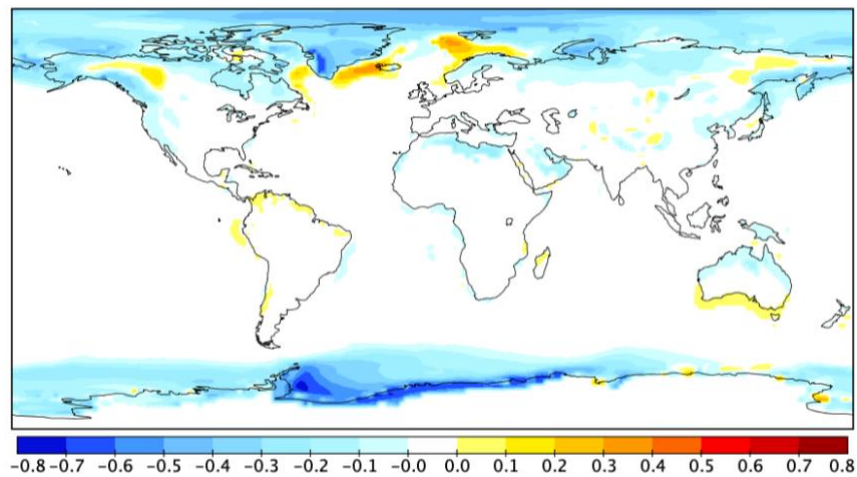
The most pronounced warming occurs over Antarctica exceeding temperature of +35 °C and Greenland (+28 °C). Other regions of exceptional warming are the Weddell Sea and Ross Sea, with a warming of up to +20 °C. Furthermore, the warming at the western border of North and South America and Tibetan Plateau is mainly related to topography changes between Miocene and PI (Figure 5.2). The only region with a pronounced cooling is located in the Nordic Seas (~14 °C), which is associated with a relative shallow GSR in comparison to PI (please see section 3.2 for further details) and in combination with ice-albedo changes (Figure 5.2b and 5.2c). Albedo changes in the continental boundaries are mostly controlled by displacement of

## 5. The Impact of Different Atmospheric CO<sub>2</sub>

### a) Surface Temperature



### b) Surface albedo



### c) Sea ice fraction

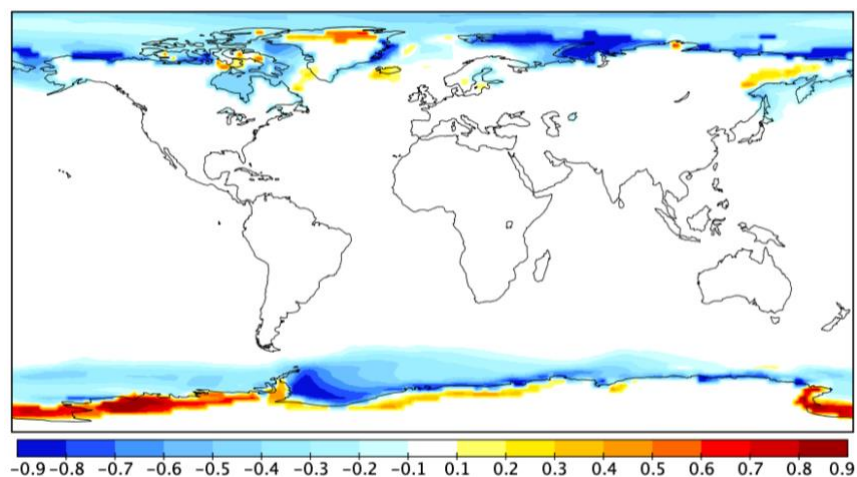


**Figure 5.2.** Annually averaged differences of a) surface air temperature (in °C), b) surface albedo and c) sea ice fraction between the Middle Miocene (MIO\_450) and the pre-industrial climate state (PI\_CTRL).

## 5. The Impact of Different Atmospheric CO<sub>2</sub>

the continents during the Miocene, contributing to the temperature changes in those regions (Figure 5.1 and 5.2). Our study suggests that substantial changes in surface albedo are vital to explain the Miocene temperature change (Figure 5.2).

### 5.2.2 Impact of atmospheric CO<sub>2</sub> and synergetic effects

To evaluate the relative importance of CO<sub>2</sub> concentrations ( $\Delta\text{CO}_2$ ) and non-CO<sub>2</sub> Miocene boundary conditions ( $\Delta\text{BC}$ ) as forcing factors we used a factor separation analysis (Stein & Alpert, 1993). We compare our simulations PI\_450 and MIO\_280 with the PI climate simulation (PI\_CTRL). According to this analysis, the synergy ( $\Delta\text{Synergy}$ ) is the difference of the combined boundary conditions effect ( $\Delta(\text{BC}+\text{CO}_2)$ ) and the singular effects  $\Delta\text{BC}$  and  $\Delta\text{CO}_2$  (Figure 5.3). The two simulations PI\_450 and MIO\_280 (Figure 5.3a and 5.3b) clearly show that changes in the CO<sub>2</sub> concentrations and non-CO<sub>2</sub> boundary conditions strongly alter the global temperature pattern. The global-mean surface temperature increase of  $\sim 3.0$  °C in MIO\_450 can be attributed to the impact of the atmospheric CO<sub>2</sub> increase from 280 to 450 ppm ( $\Delta\text{CO}_2 = +1.4$  °C) and the effect of boundary conditions changes other than CO<sub>2</sub> ( $\Delta\text{BC} = +1.3$  °C), while the synergy between them is positive ( $\Delta\text{Synergy} = +0.3$  °C).

The resulting temperature increase is very pronounced over Antarctica (+30 °C), Greenland (+22 °C), the Weddell Sea and the Ross Sea, which is largely controlled by reduced ice sheet height and sea ice cover during the Miocene. In contrast to these regions a pronounced cooling occurs in the Nordic Seas and Barents Sea where temperature decreased down to  $-16$  °C in combination with increased sea ice cover and surface albedo (Figure 5.2). Temperature changes in this region is related to relative shallow GSR than PI (Hossain et al., 2020). The relative shallow GSR reduces the entrance of warmer and saltier Atlantic waters to the Nordic Seas. The reduced corresponding warm salty water exchange across the gateway largely controls the overall temperature and salinity decrease (up to  $-6$  psu) at the ocean surface in the Nordic Seas and Barents Sea (Figure S5.2; Hossain et al., 2020). The high latitude temperature increase due to changes in ice sheet extend has a limited impact on tropical warming (Figure 5.2).

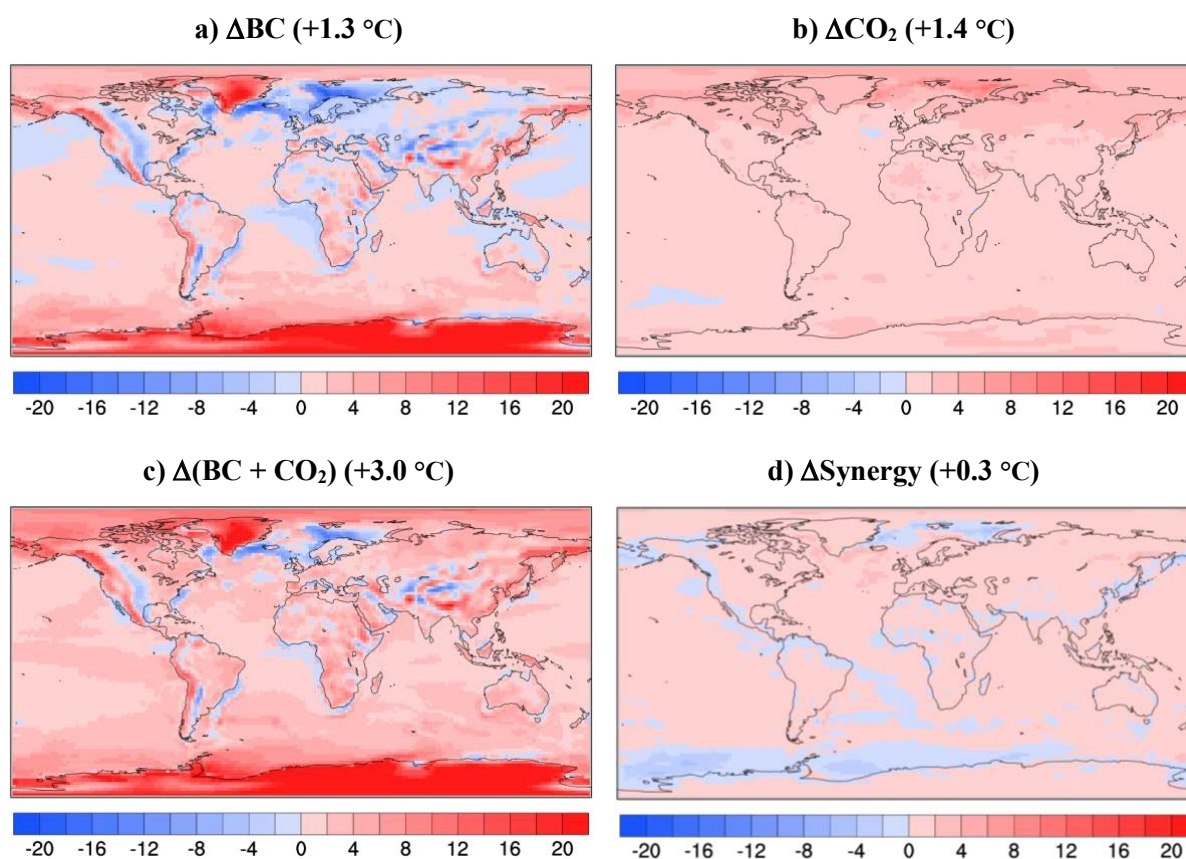


**Figure 5.3.** Application of a synergy analysis between non-CO<sub>2</sub> boundary conditions and atmospheric CO<sub>2</sub>. Synergy analysis ( $\Delta Synergy$ ) between changing non-CO<sub>2</sub> Miocene boundary conditions ( $\Delta BC$ ), declining CO<sub>2</sub> ( $\Delta CO_2$ ), and the combined effect  $\Delta(BC + CO_2)$  with respect to a change in the surface air temperature (SAT in °C).

The factor separation indicates that the warming over the Arctic and Southern Ocean (except Weddell Sea) can be interpreted by a similar influence of both forcing factors (atmospheric CO<sub>2</sub> and non-CO<sub>2</sub> Miocene boundary conditions). The warming at the western border of North America, southern border of Siberia and Tibetan Plateau is related to displacement of the continents (between Miocene and PI; Figure 5.3a), while the warming over all land masses is due to CO<sub>2</sub> changes (Figure 5.3b). The surface temperature changes in the Nordic Seas and Barents Sea are dominated by the associated bathymetry changes in these regions.

The Labrador Sea and the North Atlantic (e.g., south of Iceland) are strongly influenced by the positive synergy between the boundary conditions and the CO<sub>2</sub> forcing. In contrast to these regions the negative synergy is pronounced over Nordic Seas and Barents Sea. At the southern high-latitudes, the negative synergy effect is pronounced in the Southern Ocean, particularly in the Weddell Sea, the Ross Sea and larger coastal region of the Antarctica (Figure 5.3c). The enhanced synergy impact in these regions can be explained by a high temperature sensitivity

## 5. *The Impact of Different Atmospheric CO<sub>2</sub>*

of sea-ice and associated feedbacks that are already triggered by global temperature change in  $\Delta BC$  and  $\Delta CO_2$ . Therefore, the combined effect of both forcing factors can cause a weaker warming at a regional-scale, as well as an important positive effect at the global-scale (Figure 5.3d).

### 5.2.3 Data-model comparison

We compare the simulated annual-mean land and SSTs for Miocene experiments against available proxy data estimates (Figure 5.4; please see Burls et al., 2021). The spatial patterns of simulated surface temperatures are shown in Figure 5.5 alongside a dataset of Middle Miocene temperature proxy reconstructions (Burls et al., 2021). Both the terrestrial and SST proxies of Middle Miocene indicate a reduced meridional temperature gradient while the model simulates a substantial meridional temperature gradient (Figure 5.4a and 5.4b). The model simulations appear to demonstrate a reasonable fit with the tropical Middle Miocene SST records (Figures 5.4b and 5.5). Simulations generally suffer from cold biases outside of the tropics. Mid to high-latitudes warmth tends to fall into better agreement with the proxy data as CO<sub>2</sub> concentrations increase.

We detect cold SST biases in the Southern Ocean and North Atlantic (Figure 5.5). In general, the model simulations capture the midlatitude and tropical temperature distribution of the proxy data, but fail to capture the full extent of Miocene polar amplified warmth observed in the proxy records (Figure 5.4a and 5.4b). The nature of this mismatch can be explained by observing the equator-to-pole temperature gradient. It is 4.9 to 9.9 °C warmer in the simulations than in the proxy reconstructions (Table S5.1). Our simulations, MIO\_450 and MIO\_720 are roughly 2.0 °C and 0.3 °C colder compared to the SAT calculated from the proxy records presented here. However, the model simulations show general agreement and a high and significant correlation coefficient with proxy data. The most significant correlation coefficient and lowest root-mean-square error (RMSE) with SST records is detected for the simulation with 720 ppm of CO<sub>2</sub> ( $R = 0.86$ ,  $RMSE = 7.1$ ; Figure 5.6; Table S5.2) although the correlation coefficients with other simulations are very close. The terrestrial temperature proxies also demonstrate the lowest RMSE with the MIO\_720.

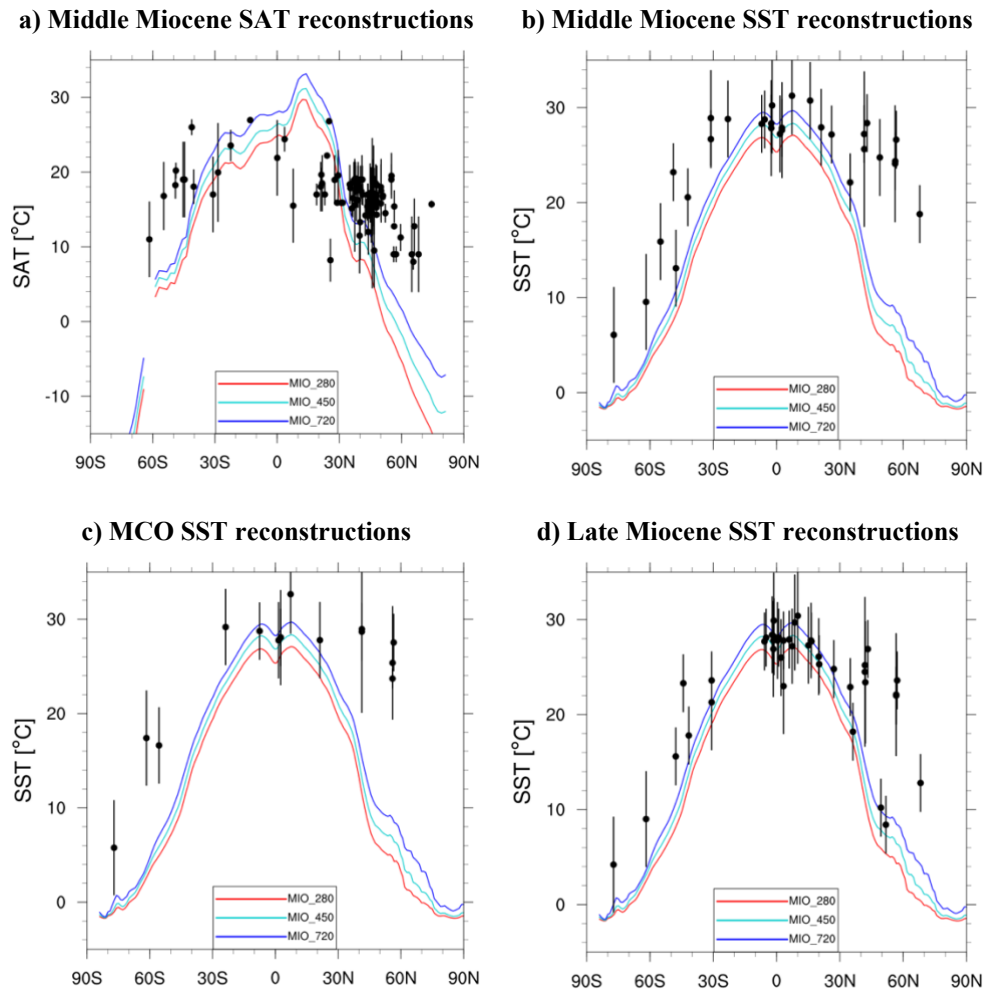


**Figure 5.4.** a) Zonal-annual-mean land surface temperature for all Miocene experiments. The circles localize the Middle Miocene terrestrial temperature reconstructions. Zonal-annual-mean SST for all Miocene experiments. The circles localize the b) Middle Miocene, c) MCO and d) Late Miocene SST reconstructions (Burlis et al., 2021).

The deviation between model and data becomes larger when we consider the MCO SST proxies (Figure 5.4; Table S5.2). Our model simulations struggle to reproduce the elevated temperatures and reduced meridional temperature gradient estimated by the MCO SST proxies. In our experiments, the low-latitudes tropics appears to provide a reasonable fit with Late Miocene proxies while the mid- to high-latitudes are too cold (Figures 5.4 and 5.7). We find most significant correlation coefficient and lowest deviations for the simulations with 720 ppm of CO<sub>2</sub> ( $R = 0.90$ ,  $RMSE = 4.3$ ; Table S5.2). Overall, we find that model simulations have better alignment with Late Miocene proxies.

## 5. The Impact of Different Atmospheric CO<sub>2</sub>

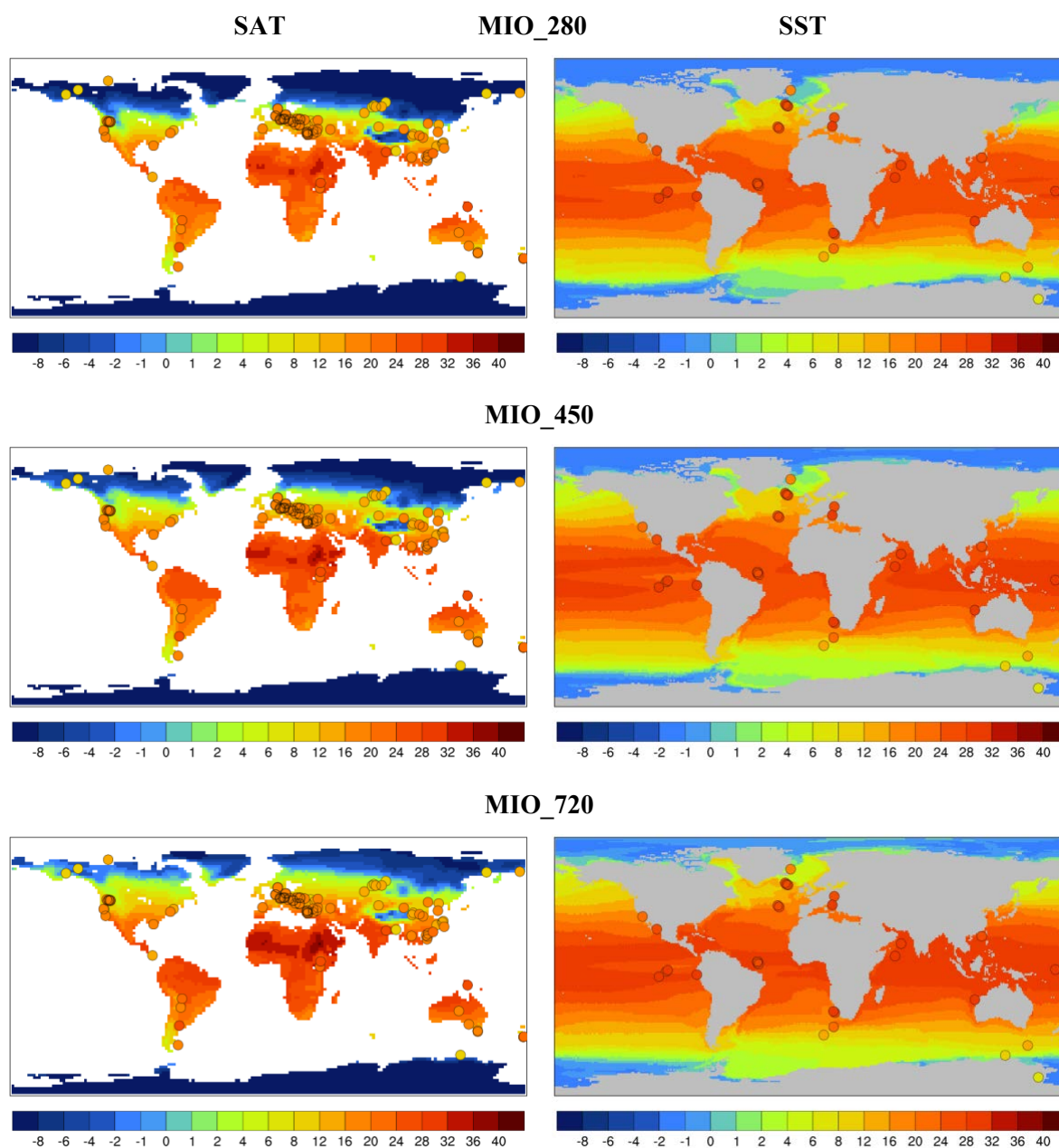


**Figure 5.5.** The global annual mean SST of different Miocene experiment outputs compared with the Middle Miocene age mean annual terrestrial and sea surface temperature reconstructions. Background color fill: the simulated global pattern of annual mean SAT and SST (in °C). The colors fill of the circles show the temperature as recorded by different proxy records, respectively.

## 5. The Impact of Different Atmospheric CO<sub>2</sub>

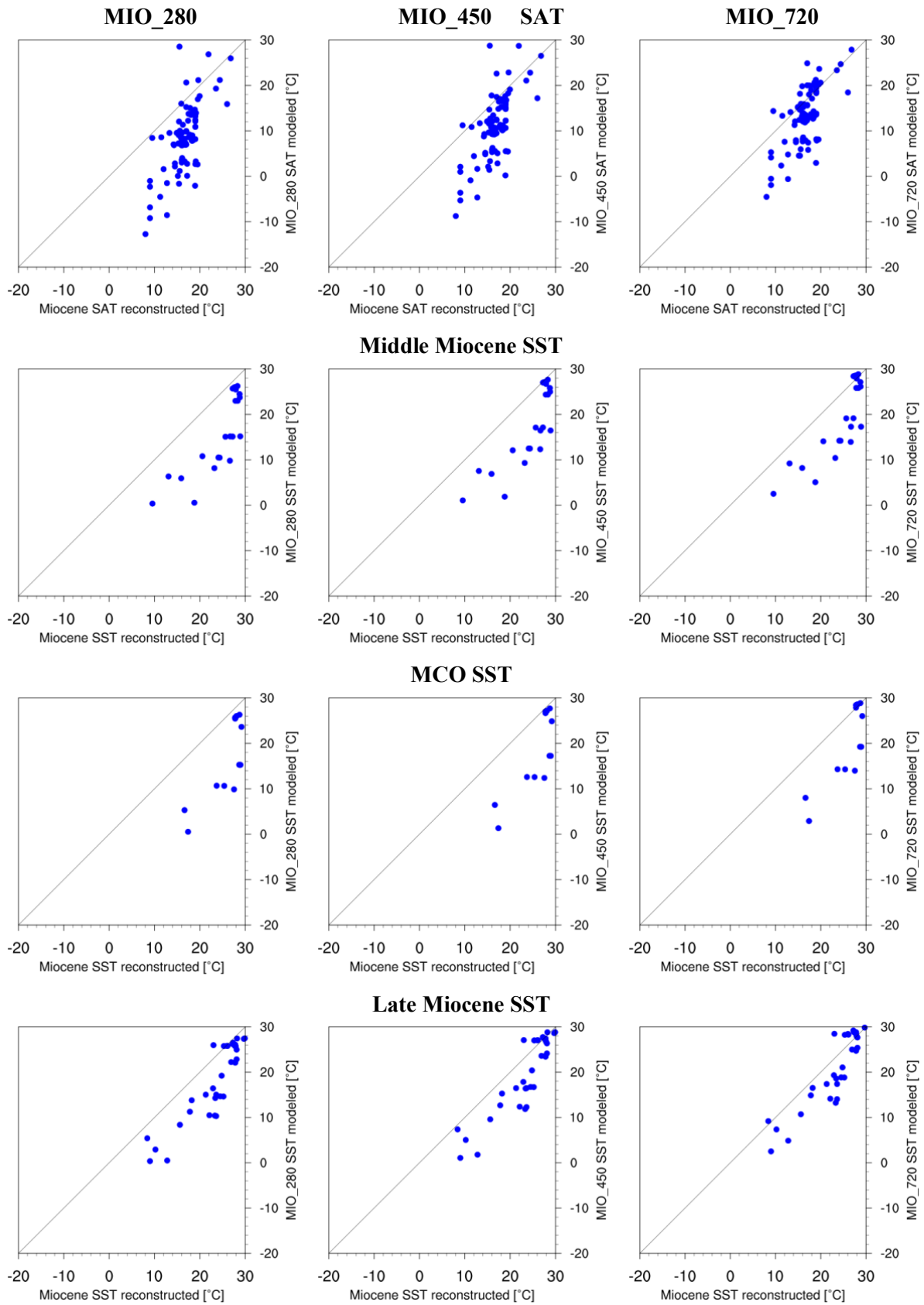


**Figure 5.6.** Model fit: Comparison of reconstructed temperature changes of the annual mean Miocene experiment output vs. the Miocene temperature reconstructions. The black line represents the 1:1 line indicating a perfect model fit.

## 5. The Impact of Different Atmospheric CO<sub>2</sub>

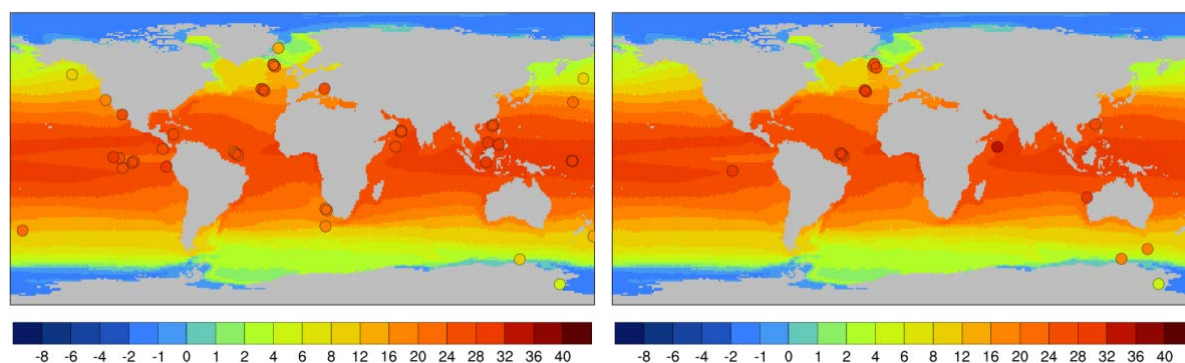


**Figure 5.7.** Annual mean SST of MIO\_450 compared with reconstructions for the Late Miocene (left) and MCO (right) (Burls et al., 2021). The colors fill of the circles show the temperature as recorded by different proxy records, respectively.

### 5.2.4 Meridional temperature changes at elevated CO<sub>2</sub> concentration

Across the Miocene simulations (at different atmospheric CO<sub>2</sub> concentrations) the magnitude of high-latitude warming spans  $\sim 10.2\text{--}13.3\text{ }^{\circ}\text{C}$  in the SH and  $\sim 1.7\text{--}11.8\text{ }^{\circ}\text{C}$  in the NH compared to PI, while tropical warming spans  $\sim 0.6\text{--}3.4\text{ }^{\circ}\text{C}$  (Figure 5.8). We observe a substantial polar amplified warmth in the high latitudes of both hemispheres across the simulations. In the higher northern latitudes, there is a pronounced polar amplification effect for CO<sub>2</sub> increase from 280 to 450 ppm (latitudinal mean surface temperature increase of  $\sim 5.4\text{ }^{\circ}\text{C}$ ; latitudinal value  $>80\text{ }^{\circ}\text{N}$ ), which is weaker for the same radiative CO<sub>2</sub> forcing from 450 to 720 ppm (latitudinal mean surface temperature increase of  $\sim 4.7\text{ }^{\circ}\text{C}$ ; latitudinal value  $>80\text{ }^{\circ}\text{N}$ ) (Figure 5.8a). That means the impact of the CO<sub>2</sub> forcing is less pronounced. Temperature difference in the low latitude is almost constant for both CO<sub>2</sub> cases.

Our warmest Miocene climate state with a CO<sub>2</sub> level of 720 ppm is characterized by a seasonality breakdown in the Arctic Ocean. We detect a pronounced warming in boreal winter (December-January-February, DJF; mean surface temperature increase of  $\sim 10.9\text{ }^{\circ}\text{C}$ ) for a CO<sub>2</sub> increase from 450 to 720 ppm, in contrast to a weak boreal summer (June-July-August, JJA) temperature increase (mean surface temperature increase of  $\sim 0.5\text{ }^{\circ}\text{C}$ ; Figure 5.8 and Table S5.2). The change in the boreal summer temperature signature is accompanied by a strong sea-ice concentration decline (Figures 5.8) and enhanced moisture availability promotes cloud formation in the summer months (Figure 5.9 and S5.3). As a consequence of the enhanced cloud formation in the boreal summer months, the planetary albedo increases which enhances the reflection of solar radiation. It dampens the temperature response to the CO<sub>2</sub> forcing at a warmer Miocene background climate.

## 5. The Impact of Different Atmospheric CO<sub>2</sub>

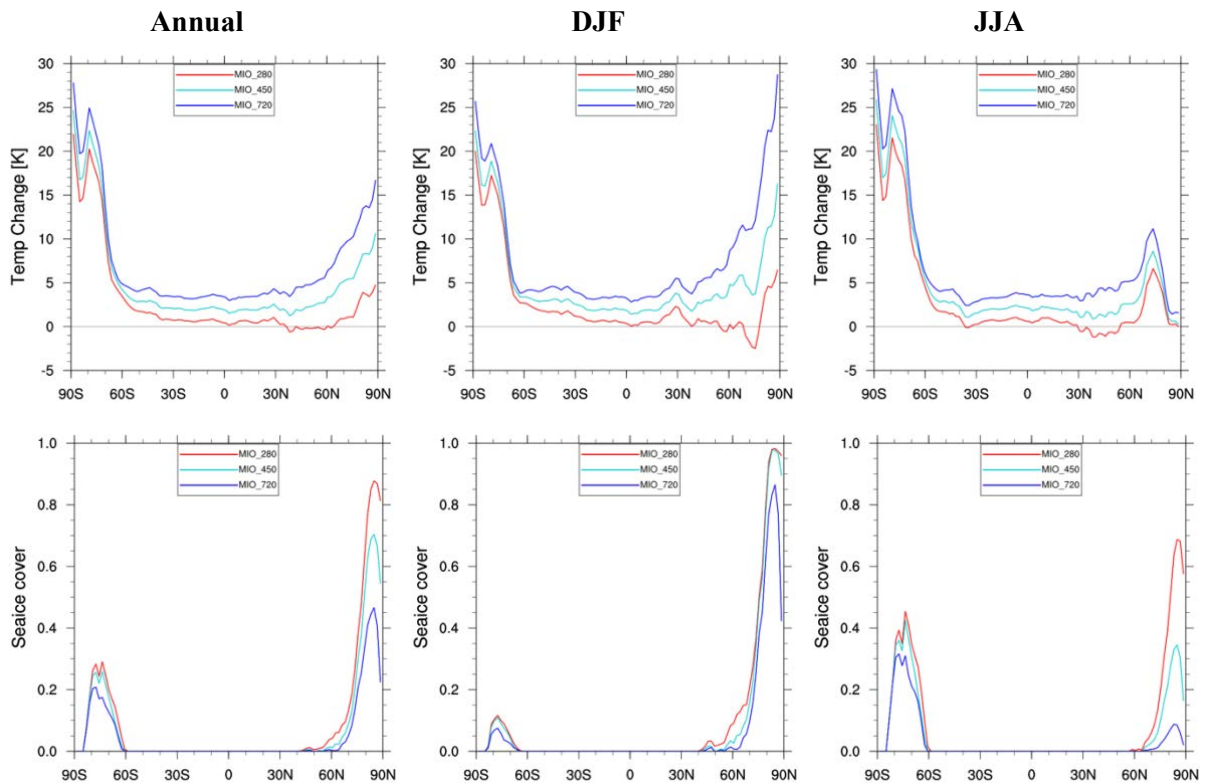


**Figure 5.8.** The zonal annual, December-January-February (DJF) and June-July-August (JJA) mean surface temperature change (top row) of Miocene experiments (relative to the PI control) and zonal annual, DJF and JJA mean sea-ice cover (bottom row) of Miocene experiments.

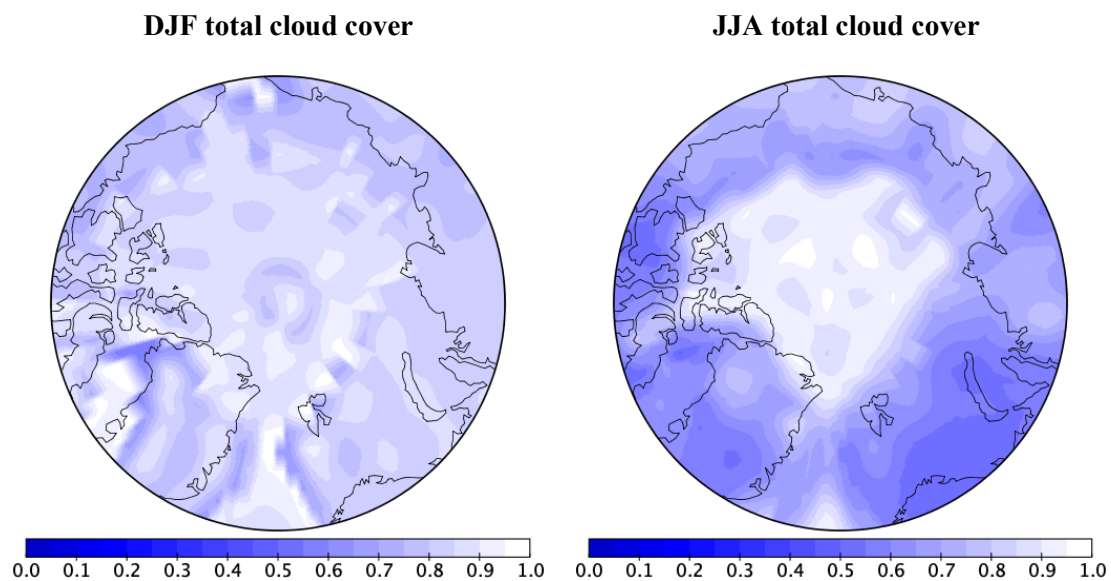


**Figure 5.9.** DJF (left) and JJA (right) mean total cloud cover for the experiments of MIO\_720.

### 5.3 Discussion

Climate simulations of Middle Miocene by Krapp & Jungclaus (2011) found a surface temperature of ~17.1–19.2 °C (at a CO<sub>2</sub> level of 480–720 ppm) that is in the range of our simulations with corresponding CO<sub>2</sub> levels (Table S5.1). Our simulated Miocene climate (using CO<sub>2</sub> concentrations of 280–720 ppm) shows a global mean SST of 17.5–20.0 °C which is in good agreement with the Early to Middle Miocene simulations used in Burls et al. (2021) but colder (~3.7–6.7 °C) than the global mean surface temperature estimates for the Middle Miocene (24.46°C ± 0.81°C) based on the compiled proxy SST syntheses (Burls et al., 2021).

The modelled Miocene climate (MIO\_450) exhibits a sensitive SAT response (+1.4 °C) to CO<sub>2</sub> increase, which is governed by different climate feedbacks, such as water vapour (Soden & Held, 2006; +19% increase compared to PI; Table S5.2) and sea-ice changes (Figure 5.10; Soden & Held, 2006; Knorr et al., 2011). Our non-CO<sub>2</sub> Miocene boundary conditions (including paleobathymetry, ice sheet height) raise global temperature by +1.3 °C, agreeing with previous estimates (Burls et al., 2021). Strong regional warming is detected in response to reduced height of the Antarctic ice sheet and the absence of a Greenland ice sheet but the influence is limited beyond the both hemispheres high latitudes (Burls et al., 2021). The major warming as compared to PI (Figure 5.4) is caused by atmospheric CO<sub>2</sub> and land surface characteristics changes (e.g., surface albedo) linked with aspects of the global energy balance (e.g., effective longwave emissivity, planetary albedo) (Knorr et al., 2011; Burls et al., 2021). A sea surface cooling occurs in the Nordic Seas due to a relative shallow GSR in combination with the associated ice-albedo feedback is also found in Hossain et al. (2020), which supports our findings.

During the Miocene, different proxy reconstructions suggest that SSTs were ~8–10 °C warmer than PI in the high latitudes of the SH (Shevenell et al., 2004), ~10–15 °C warmer in the NH (Super et al., 2020) and ~5–8 °C warmer in the deep ocean (Lear et al., 2015), leading to a global mean surface warming of ~7.6–2.3 °C compared to PI (Goldner et al., 2014), which are in the range of our Miocene simulations. Burls et al. (2021) estimate global mean surface temperature reconstructions of ~5.3–11.5 °C higher than PI. The equator-to-pole is ~4.9–9.9 °C warmer in our simulations than proxy data compared to ~17 °C in Goldner et al. (2014). However, the model simulations show general agreement and a significant correlation

## 5. The Impact of Different Atmospheric CO<sub>2</sub>

coefficient with proxy data which are in the range of the Early to Middle Miocene simulations used in Burls et al. (2021; Table S5.2 & S5.3). Overall, the results of our study might better explain the proxy data and circulation patterns of the World Oceans, in particular Southern Ocean due to the state-of-the-art numerical approach and a realistic enhanced paleobathymetry are used, compared with previous smoother bathymetry and lower resolution models. As for the Eocene, high-resolution model simulations with similar enhanced paleobathymetry in the Southern Ocean has shown some improvement in the ability to simulate heat transport and circulation patterns of the Southern Ocean, consistent with available proxy data (Sauermilch et al., 2021).

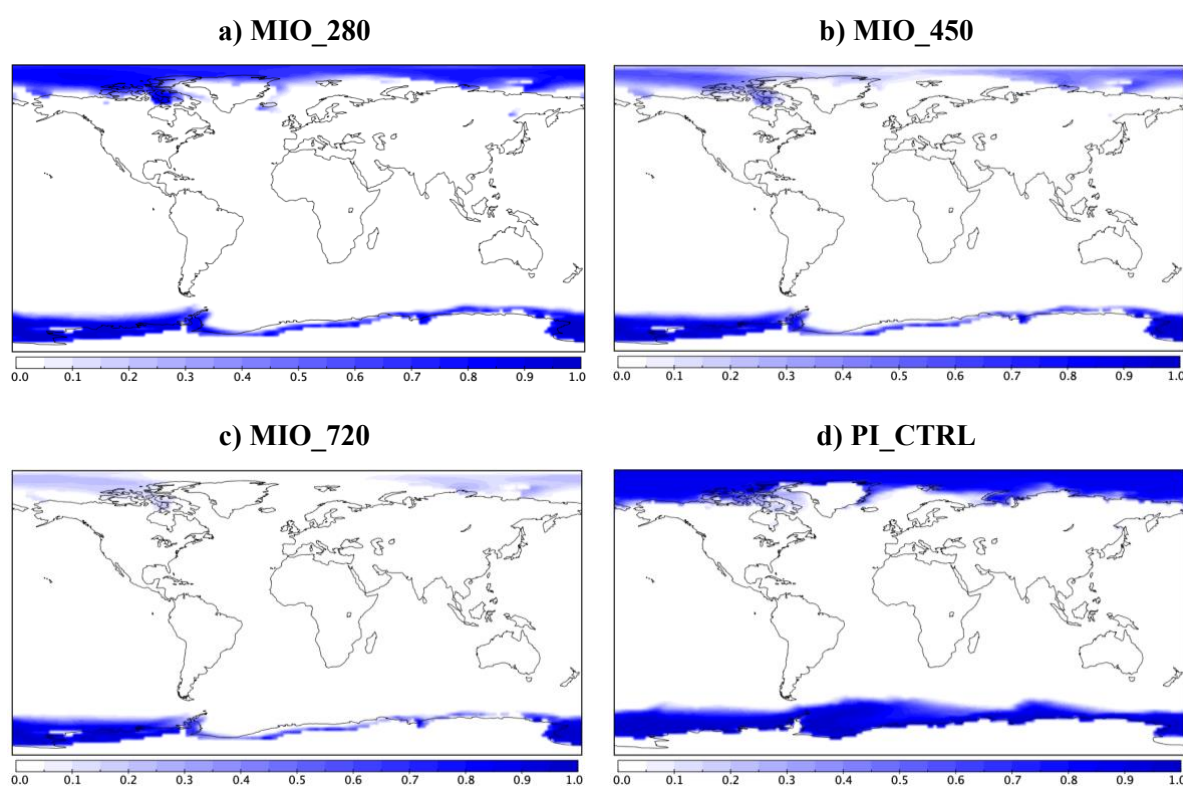


**Figure 5.10.** Summer mean sea-ice cover for the experiments of a) MIO\_280, b) MIO\_450, c) MIO\_720 and d) PI\_CTRL.

Seasonal paleoclimate data (Utescher & Mosbrugger, 2007) and Goosse et al. (2018) suggest that the polar amplification warmth has a large seasonal cycle. The mean warming is minimum during boreal summer and maximum during boreal winter/fall with a peak in November in the Arctic Ocean (Utescher & Mosbrugger, 2007; Laine et al., 2016), which supports our results. In a warmer climate, the total amount of clouds increases, which increases the planetary albedo as well as the amount of reflected solar radiation, and acting as a negative cloud optical depth

## 5. *The Impact of Different Atmospheric CO<sub>2</sub>*

feedback (Goosse et al., 2018; Figure S5.3). Climate models robustly show the cloud optical depth feedback (Zelinka et al., 2012; Goosse et al., 2018) but it is stronger than implied by proxies (Ceppi et al., 2016; Terai et al., 2016). In boreal winter, the heat released by the ocean and cloud feedbacks induce a pronounced warming (Figure 5.8; Laîné et al., 2016; Goosse et al., 2018).

The weakening of the meridional temperature gradient and degree of polar amplified warming increases in the simulations with higher CO<sub>2</sub> levels, but generally fails to capture the full extent of weakening of the reconstructed meridional gradient observed in the proxies (Burls et al., 2021). This inability of our model to capture the full extent of the reduction of meridional temperature gradient and polar amplified warmth reflected in proxies is an issue that is not only unique to either our model or Miocene but also seen in different paleoclimate modelling studies during the Cenozoic (Huber & Caballero, 2011; Krapp & Jungclauss, 2011; Goldner et al., 2014; Haywood et al., 2020; Steinthorsdottir et al., 2021; Burls et al., 2021).

Potential mechanisms that could clarify the discrepancy between proxy reconstructions and models are linked with the Arctic amplification, where surface albedo and lapse rate provide feedback to climate warming (Pithan & Mauritsen, 2014), which depends on the atmosphere vertical structure. Another effect might be major reorganizations of the ocean circulation (Butzin et al., 2011), potentially associated with feedbacks including the vegetation and hydrological cycle (Lohmann et al., 2015; 2022). A combination of higher atmospheric CO<sub>2</sub> and more effective ocean mixing can contribute to much warmer high latitudes, and a reduced winter-to-summer range of temperature (Valdes et al., 1996; Sloan et al., 2001; Lohmann et al., 2022).

### **5.4 Conclusions of Chapter Five**

By means of the state-of-the-art climate model AWI-ESM2.1, we have simulated Miocene climate states at different atmospheric CO<sub>2</sub> concentrations and evaluated the effect of model boundary conditions during the Middle Miocene. We estimate a global mean surface warming of +3 °C relative to the PI state at a CO<sub>2</sub> level of 450 ppm. The atmospheric CO<sub>2</sub> increase from 280 to 450 ppm provides an individual warming contribution of ~1.4 °C, which is approximately as strong as all non-CO<sub>2</sub> Miocene forcing contributions combined (~1.3 °C). In combination with ice-albedo changes, the resulting temperature change is largely pronounced

## 5. *The Impact of Different Atmospheric CO<sub>2</sub>*

in the high-latitudes. A pronounced cooling in the Nordic Seas, is associated with relative shallow GSR comparative to PI and in combination with ice-albedo changes, is detected. We compare the modelled climate with available surface temperature proxy reconstructions to assess the range of model-data agreement. The simulated surface temperatures fit well with proxy reconstructions except in the high latitudes. The high latitude cooling bias becomes less pronounced for higher CO<sub>2</sub> concentrations and is least pronounced in our simulation with a CO<sub>2</sub> concentration of 720 ppm. The most significant correlation coefficient and lowest RMSE with terrestrial and SST records are detected for the simulation with higher CO<sub>2</sub> level. Our climate simulation with higher CO<sub>2</sub> level shows a reduced climate sensitivity and polar amplification, since the warmest Miocene climate state with a CO<sub>2</sub> level of 720 ppm is characterized by a seasonality breakdown in the Arctic Ocean. A pronounced warming in boreal winter is detected for a CO<sub>2</sub> increase from 450 to 720 ppm, in contrast to a weak boreal summer warming response. This change in the seasonal temperature response is accompanied by a strong sea-ice concentration decline and enhanced moisture availability promotes cloud formation in the summer months. As a consequence the planetary albedo increases (i.e., the reflection of solar radiation enhances) and dampens the temperature response to the CO<sub>2</sub> forcing at a warmer Miocene background climate.

Overall, our model simulations show general agreement and a significant correlation coefficient with proxy data and are in the range of the Early to Middle Miocene simulations. Furthermore, the results of our study might better explain the proxy data and circulation patterns of the World Oceans, in particular Southern Ocean due to the state-of-the-art numerical approach and a realistic enhanced paleobathymetry are used, compared with previous smoother bathymetry and lower resolution models. However, it's need to be further investigated. Future sensitivity studies can use our model setup and evaluate the effect of combined high-resolution global paleobathymetry (implemented in this study) on ocean circulation and climate. Moreover, in the future, the sensitivity studies with the enhanced vertical mixing (Lohmann et al., 2022), state-of-the-art parameterizations of cloud-aerosol interactions (Lunt et al., 2021; Zhu et al., 2019; Zhu & Poulsen, 2019), changes in aerosols (Lunt et al., 2021), improved representations of tidal mixing (Green & Huber, 2013; Lohmann, 2020), might be required for providing more realistic climatic response for the Miocene.

## 5.5 Appendix

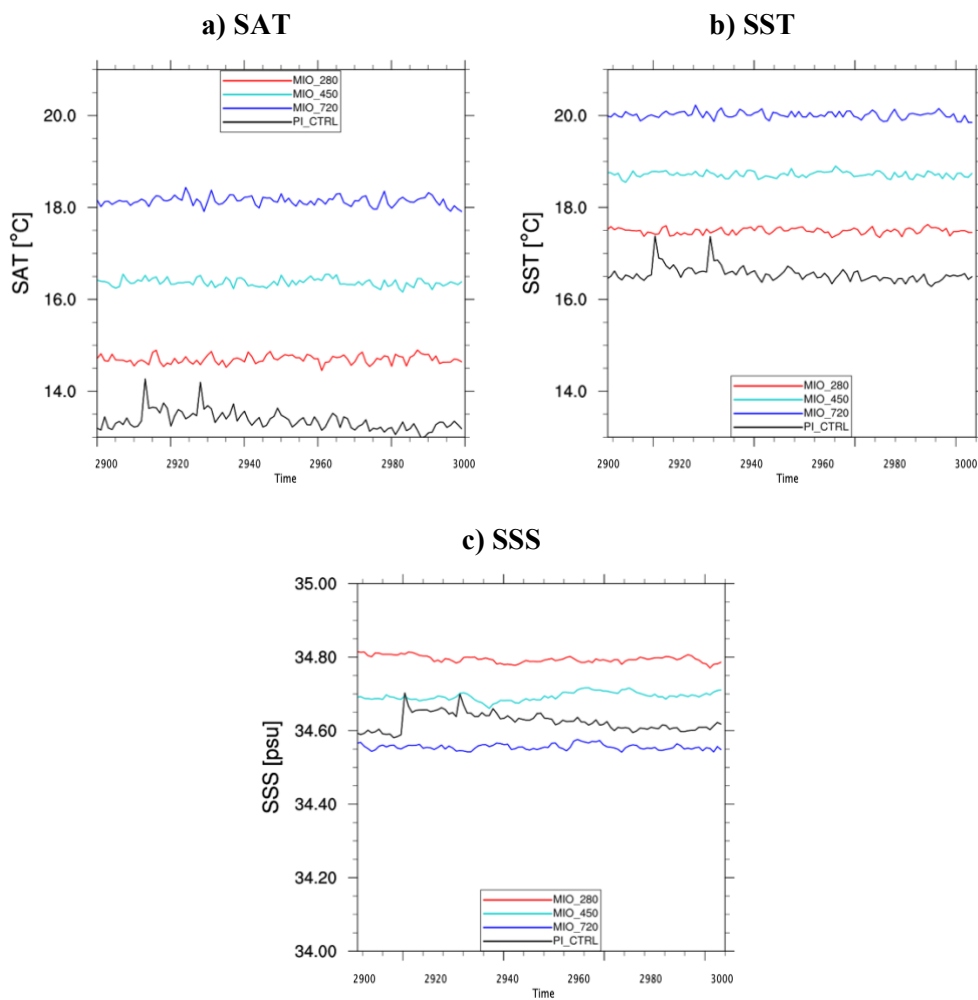


**Figure S5.1.** The timeseries of a) surface air temperature (in °C), b) sea surface temperature (in °C) and c) sea surface salinity (in psu) of MIO\_280, MIO\_450, MIO\_720 and PI\_CTRL.

## 5. The Impact of Different Atmospheric CO<sub>2</sub>

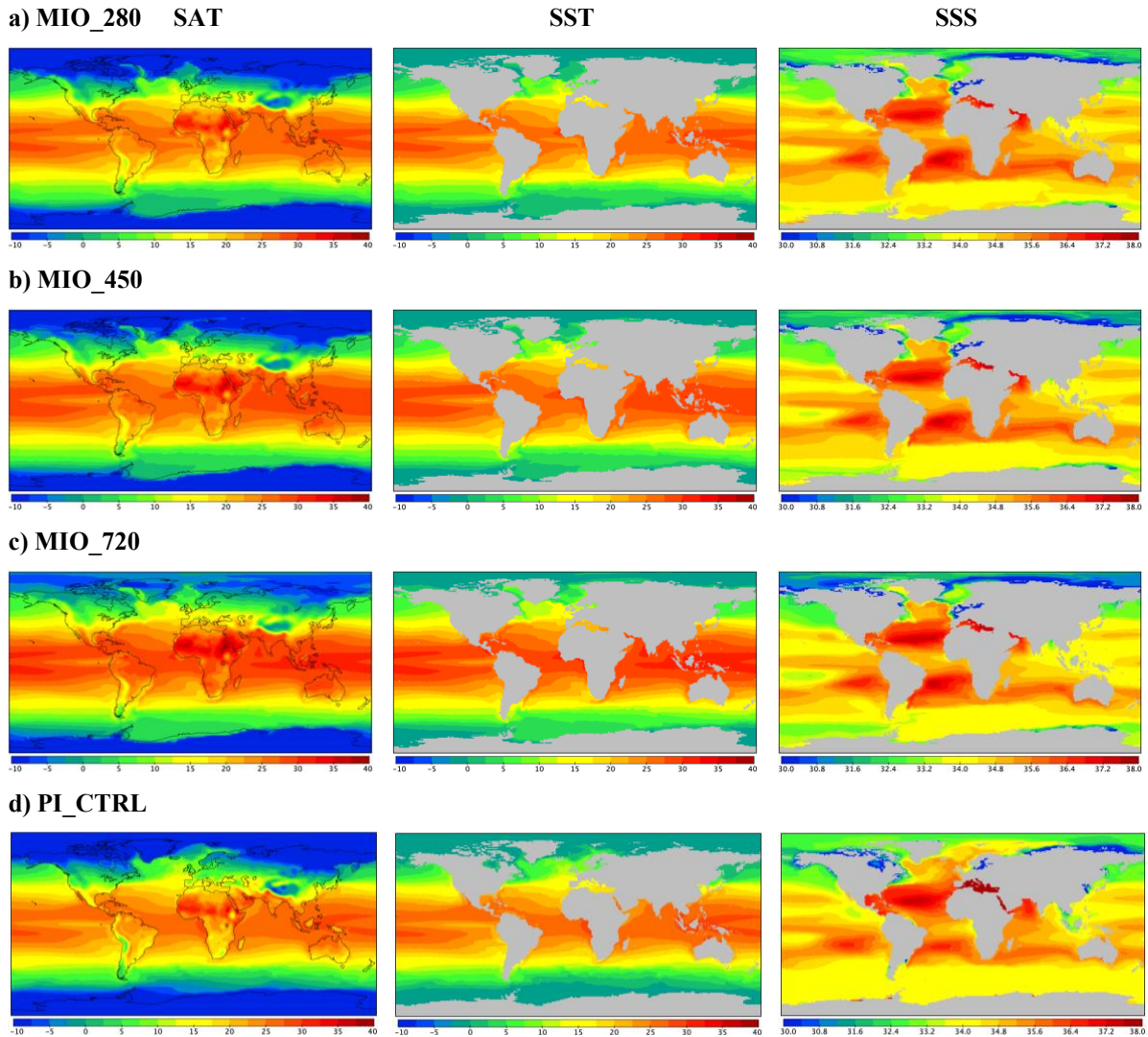


**Figure S5.2.** Annual mean surface air temperature (in °C), sea surface temperature (in °C) and sea surface salinity (in psu) of a) MIO\_280, b) MIO\_450, c) MIO\_720 and d) PI\_CTRL.

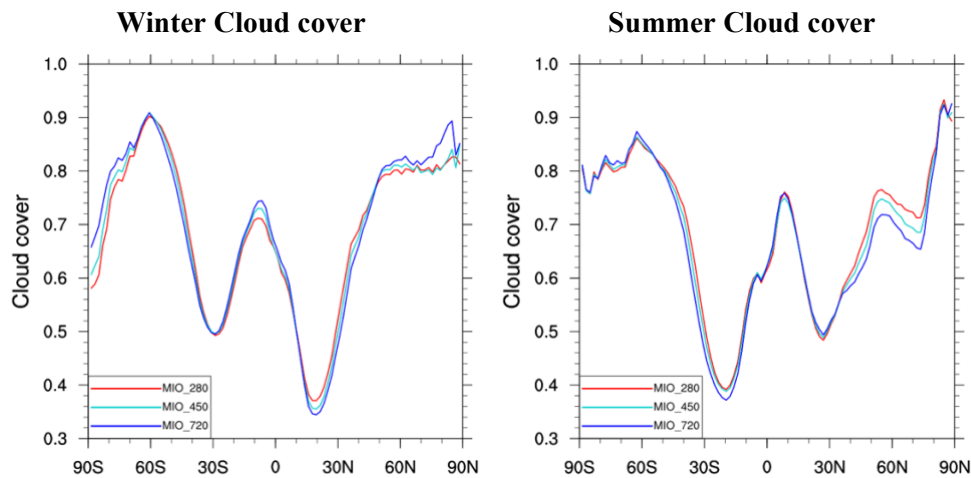


**Figure S5.3.** a) Winter and b) Summer zonal mean total cloud cover for the experiments of MIO\_280, MIO\_450 and MIO\_720.

## 5. The Impact of Different Atmospheric CO<sub>2</sub>

**Table S5.1:** Key Diagnostics of different model simulations.

Model Ex.	Mean SAT (°C)	Mean SST (°C)	Mean temperature at ~2400 m	Mean SSS (psu)	Mean Arctic SAT (°C)	JJA mean Arctic SAT (°C)	DJF mean Arctic SAT (°C)	Mean Arctic SST (°C)	Mean SSS Arctic (psu)	Equator to pole* temperature gradient (K)	Global mean vert. Integ. water vapour (kg/m <sup>2</sup> )
MIO_280	14.7	17.5	3.1	34.8	-15.2	-28.7	-0.8	-1.6	31.7	34.4	22.7
MIO_450	16.4	18.7	3.9	34.7	-9.8	-21.8	-0.3	-1.4	31.2	31.8	25.5
MIO_720	18.1	20.0	4.7	34.6	-5.1	-10.9	0.7	-0.7	30.8	29.4	28.9
PI_CTRL	13.3	16.6	1.8	34.6	-16.9	-33.1	-1.6	-1.8	32.8	34.6	21.4
PI_450	14.7	17.5	3.2	34.7	-12.8	-27.8	-1.1	-1.6	32.3	32.2	23.6

\* Equator-to-pole temperature gradient for proxies is 24.5 °C

**Table S5.2:** The correlation and RMSE between the simulated annual mean SAT/SST and annual mean Middle Miocene SAT/SST, MCO SST and Late Miocene proxy reconstructions.

Model Ex.	Middle Miocene SAT			Middle Miocene SST			MCO SST			Late Miocene SST		
	R	R <sup>2</sup>	RMSE	R	R <sup>2</sup>	RMSE	R	R <sup>2</sup>	RMSE	R	R <sup>2</sup>	RMSE
MIO_280	0.65	0.42	9.9	0.84	0.70	9.6	0.80	0.64	10.6	0.89	0.80	6.5
MIO_450	0.67	0.45	7.8	0.85	0.73	8.3	0.83	0.68	9.2	0.90	0.81	5.3
MIO_720	0.68	0.46	5.9	0.86	0.73	7.1	0.83	0.70	7.9	0.90	0.81	4.3

## 5. The Impact of Different Atmospheric CO<sub>2</sub>

**Table S5.3:** The correlation and RMSE between the annual mean SAT of different Early to Middle Miocene simulations and the Middle Miocene annual mean SAT proxy reconstructions (Burls et al., 2021).

Model Ex.	R	R <sup>2</sup>	RMSE
CCSM-NH3 355ppm	0.56	0.31	7.9
CCSM-NH3 560ppm	0.55	0.31	6.7
CCSM3 T42 MMCO 400ppm	0.56	0.31	6.5
CCSM3 T42 MMCO 200ppm	0.56	0.32	8.0
CCSM3 T42 MMG 200ppm	0.56	0.31	8.2
CCSM3 T42 MMG 400ppm	0.56	0.31	6.7
CCSM4 400ppm	0.56	0.31	5.9
CESM1 400ppm	0.59	0.35	6.6
COSMOS Middle Miocene 278ppm	0.55	0.31	7.3
COSMOS Middle Miocene 450ppm	0.52	0.27	6.7
HadCM3L Middle Miocene 90SLE 280ppm	0.63	0.40	8.2
HadCM3L Middle Miocene 90SLE 400ppm	0.62	0.39	5.8
HadCM3L Middle Miocene 90SLE 560ppm	0.62	0.38	5.0
HadCM3L Middle Miocene 90SLE 850ppm	0.60	0.36	5.4
HadCM3L Middle Miocene 55SLE 280ppm	0.63	0.40	8.4
HadCM3L Middle Miocene 55SLE 400ppm	0.63	0.39	6.0
HadCM3L Middle Miocene 55SLE 560ppm	0.61	0.38	5.0
HadCM3L Middle Miocene 55SLE 850ppm	0.60	0.36	5.4
HadCM3L Middle Miocene NoICE 280ppm	0.63	0.39	8.4
HadCM3L Middle Miocene NoICE 400ppm	0.63	0.39	5.9
HadCM3L Middle Miocene NoICE 560ppm	0.61	0.38	5.0
HadCM3L Middle Miocene NoICE 850ppm	0.61	0.37	5.5
HadCM3L Langhian 280ppm	0.54	0.29	12.4
HadCM3L Langhian 400ppm	0.55	0.30	10.1
HadCM3L Langhian 560ppm	0.55	0.31	8.4
IPSLCM 20Ma 420ppm	0.53	0.28	6.3
IPSLCM 20Ma 560ppm	0.52	0.27	6.2
IPSLCM 20Ma 840ppm	0.52	0.28	7.2
IPSLCM 20Ma NoGIS 560ppm	0.53	0.28	6.3
NorESM-L 20Ma 350ppm	0.57	0.33	5.4
NorESM-L 20Ma 560ppm	0.56	0.31	4.6

## *5. The Impact of Different Atmospheric CO<sub>2</sub>*

## Summary and Conclusions

The present study was aimed to simulate Miocene climate conditions at different atmospheric CO<sub>2</sub> concentrations and investigate thermohaline changes in response to the subsidence of Atlantic-Arctic gateways for various Greenland-Scotland Ridge (GSR) and Fram Strait (FS) configurations. The primary focus has been on surface temperature changes, specifically the sensitivity of temperature changes to the range of boundary conditions applied across the simulations. It also gives insight into the model capability to capture the full range of polar amplified warmth and reduced meridional temperature gradient patterns observed in the proxy reconstructions. In this thesis work, a set of Miocene climate simulations has been performed with state-of-the-art fully coupled atmosphere-ocean-sea-ice model approaches and Early to Middle Miocene boundary conditions.

The Miocene simulations (at different atmospheric CO<sub>2</sub> concentrations) show a substantial polar amplified warmth in the high latitudes of both hemispheres. The simulated surface temperatures are compared against available proxy data to assess the range of model-data agreement and large-scale Miocene surface warming patterns over both ocean and land. Both the terrestrial and sea surface temperature proxies of Middle Miocene indicate a reduced meridional temperature gradient while the model simulates a relatively pronounced meridional temperature gradient. The model simulations appear to demonstrate a reasonable fit with the tropical Middle Miocene sea surface temperature records. Mid to high-latitudes warmth tends

## 6. Summary and Conclusions

to fall into better agreement with the proxy data as CO<sub>2</sub> concentrations increase. In general, the model simulations capture the midlatitude and tropical temperature distribution of the proxy data, but cannot capture the full extent of Miocene polar amplified warmth observed in the proxy records.

Better understanding of gateway evolution is essential to improve the accuracy of climate model. Based on the geological/geophysical constraints the present study deduces the relative timing of subsidence of Atlantic-Arctic gateways. The final opening of the Arctic–Atlantic gateway gradually allowed more deep-water mass exchange (Hossain et al., 2020; 2021), which likely caused an intensification of the North Atlantic Deep Water (NADW; Hossain et al., 2020). Moreover, the opening of FS allowed entrance of saline Atlantic waters to the Arctic Ocean and established the ventilation of the Arctic Ocean (Hossain et al., 2020; 2021).

The following conclusions were made in response to the four key questions that motivated the present work:

1. *What are the thermohaline responses to the subsidence of Greenland-Scotland Ridge and Fram Strait during early to middle Miocene?*

In Chapter 2 thermohaline changes in response to different GSR and FS subsidence histories were investigated in different model scenarios. A singular subsidence of GSR and FS enables enhanced circulation of saltier and warmer water from the Atlantic Ocean to the Arctic Ocean that induces a salinization process in this region and causes thermohaline changes in the Arctic Ocean, Nordic Seas as well as in the south of Iceland. It also influences the NADW formation. Furthermore, based on geological evidence and tectonic constraints this study conjectures that a tectonic situation with a progressive GSR deepening for a shallow FS sill depth configuration is the most likely Eocene to Miocene scenario. The deepening of FS initiated when GSR was already becoming deep. However, changes in the relative timing of the Atlantic-Arctic gateways are not only a key control for North Atlantic and Arctic environmental conditions, but also have far field bi-polar impacts. Considering the impact of the gateways' subsidence, the GSR deepening is the dominant controlling factor for thermohaline changes.

2. *What are the minimum depth and width of Fram Strait that is required for ventilation of the Arctic Ocean?*

The results in Chapter 3 indicate that for a FS sill depth at around 1500 m, a ventilation of the Arctic Ocean regime has been achieved due to enhanced import of saline Atlantic water through a FS width of ~105 km. Scientific drilling in the central Arctic Ocean suggests that the evolution of a poorly ventilated and land-locked sea to a fully ventilated Arctic Ocean at around 17.5 Ma (Jakobsson et al., 2007). Moreover, at this width and depth, a modern-like three-layer stratification in the Arctic Ocean is observed, with a shallow surface layer of cold and low-salinity water situated above a deep and warmer layer of Atlantic origin and a cold bottom layer.

3. *How did the opening of the Fram Strait during early-to-middle Miocene influence the global ocean circulation/current system?*

The geometrical opening of FS during early Miocene was an important climatic event that enhanced the water exchange between the Atlantic and Arctic oceans, strongly affected the paleoceanographic conditions in the Arctic (Thompson et al., 2012; Hossain et al., 2020; 2021) and possibly affected the global thermohaline circulation (Haley et al. 2008). It increases salinity in the Arctic Ocean and influences the density of NADW by entrainment. The opening of the FS establishes a three-layer exchange flow through the FS that is characterized by vertical differentiation of water masses. With the establishment of a bi-directional circulation regime and an Arctic halocline, the through-flow into the Arctic Basin causes the reorganization towards a ventilated Arctic salinity regime. However, the simulations do not show dramatic changes in the global circulation pattern and global climate questioning the role of the FS in triggering/enabling the NHG.

4. *What are the impacts of atmospheric CO<sub>2</sub> changes on large scale Miocene temperature changes? To what extent can a climate model reproduce the temperature signals that are acquired from proxy records?*

The atmospheric CO<sub>2</sub> forcing provides an individual warming contribution of ~1.4 °C relative to PI, which is approximately as strong as all non-CO<sub>2</sub> Miocene forcing contributions combined (~1.3 °C). For a CO<sub>2</sub> increase from 280 to 450 ppm polar amplification is simulated in the northern high latitudes, which is stronger than for the

## 6. Summary and Conclusions

same radiative CO<sub>2</sub> forcing from 450 to 720 ppm. At higher CO<sub>2</sub> levels the Miocene climate also shows a reduced climate sensitivity. The warmest Miocene climate scenario with a CO<sub>2</sub> level of 720 ppm is characterized by a seasonality breakdown in the Arctic Ocean, where a pronounced warming in boreal winter, in contrast to a weak boreal summer warming response is detected.

The model simulations show general agreement and a significant correlation coefficient with proxy data. Simulations with higher CO<sub>2</sub> levels show the best fit to proxy reconstructions of surface temperatures, since in particular the high latitude cooling bias becomes least pronounced. The weakening of the meridional temperature gradient and degree of polar amplified warming increases in the simulations with higher CO<sub>2</sub> levels, but generally fails to capture the full extent of weakening of the reconstructed meridional gradient observed in the proxies. It is obvious that our understanding of important physical parameters or positive feedbacks is missing or incomplete to explain how these processes and climate trends are related to these reconstructed atmospheric CO<sub>2</sub> changes.

However, this inability of the model to capture the full extent of the reduction of meridional temperature gradient and polar amplified warmth reflected in proxies is an issue that is not only unique to either the studied model or Miocene but also seen in different paleoclimate modelling studies during the Cenozoic (Huber & Caballero, 2011; Krapp & Jungclaus, 2011; Goldner et al., 2014; Haywood et al., 2020; Steinthorsdottir et al., 2021; Burls et al., 2021). Overall, better understanding of important physical parameters and boundary conditions (including bathymetry, orography and ocean gateways evolution) is essential to improve the accuracy of climate model.

Interestingly, a moderate low-latitude and pronounced high-latitude warming (~12 °C in the Arctic temperature relative to PI) is simulated in the recent Miocene climate simulations (Figure 6.1; Lohmann et al., 2022). It is found that enhanced ocean mixing with atmospheric CO<sub>2</sub> levels of 450 ppm can contribute to much warmer high latitudes and enable meridional temperature characteristics representative of MCO reconstructions. However, the climate simulations cannot realistically represent the vertical mixing but aim to approach the possible explanations for the Miocene climate under changed sensitive ocean parameters. Implementation of this mixing hypotheses in future research might improve the ability of models to simulate Miocene warmth and meridional gradients.

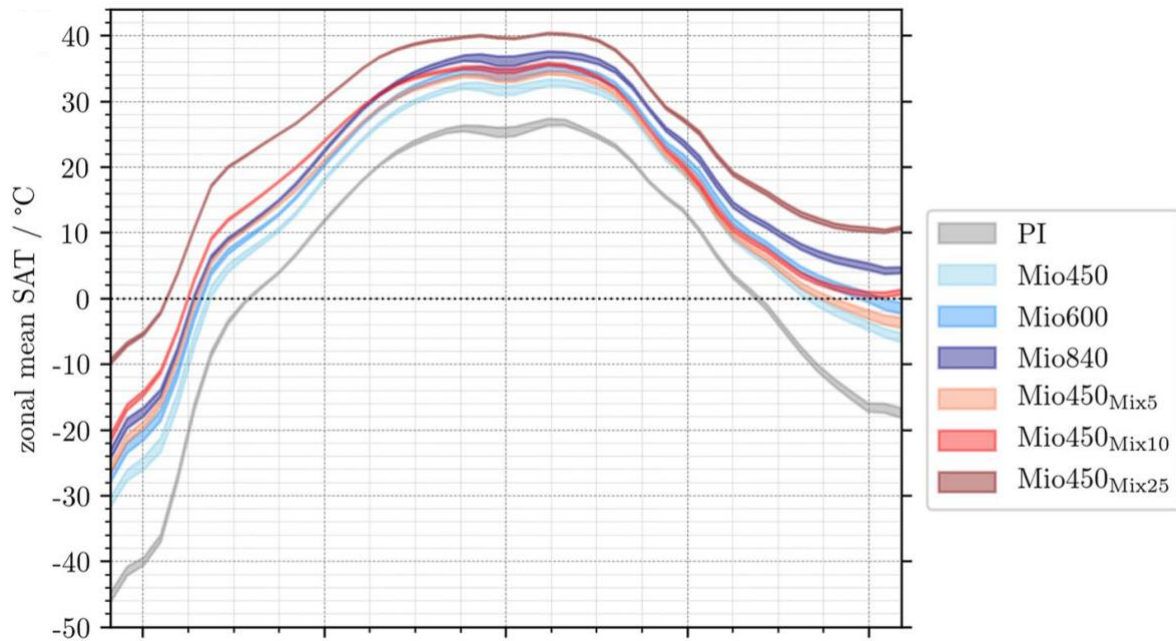


**Figure 6.2.** Zonal-annual mean surface air temperature (SAT) for the Miocene (Mio) at different atmospheric  $\text{CO}_2$  concentrations. The results of Miocene reference simulation (with a  $\text{CO}_2$  level of 450 ppm), simulations with increased atmospheric  $\text{CO}_2$  (600 and 840 ppm) and preindustrial (PI) simulation with standard vertical mixing parameters are shown. Moreover, three additional simulations with 5, 10, and 25-times increased ocean mixing (indicated by Mix 5, Mix 10, and Mix 25, respectively) are provided (taken from Lohmann et al., 2022).

## *7. Outlook*

Chapter



# 7

## Outlook

The presented study utilized a state-of-the-art numerical approach and a realistic enhanced paleobathymetry, particularly in the Southern Ocean, compared with previous smoother bathymetry, which might better explain the proxy data and circulation patterns of the World Oceans. The diverse examinations presented in this thesis work have allowed for new insights into the Miocene climate, which may help shaping the future of Miocene research can be summarized below:

- Future data from up-coming drilling projects that target the past climate evolution can use these presented gateways scenarios and characteristic thermohaline changes as basis for various interpretation models to test and further our understanding of the high-latitude climate evolution by superposed gateway changes.
- Moreover, further sensitivity studies are needed to investigate the impact of other key ocean gateways changes including the Panama Gateway, the Drake Passage, the Indonesian Seaway, the Tethys Gateway and Canadian archipelago, exploring different widths and depths of gateways based on maximum/minimum estimates from plate tectonic reconstructions.

## 7. Outlook

- Future sensitivity studies can use the presented model setup (Chapter 5) and evaluate the effect of combined high-resolution global paleobathymetry (implemented in this study) on ocean circulation and climate.
- Furthermore, in the future, the sensitivity studies with the enhanced vertical mixing (Lohmann et al., 2022), state-of-the-art parameterizations of cloud-aerosol interactions (Lunt et al., 2021; Zhu et al., 2019; Zhu & Poulsen, 2019), changes in aerosols (Lunt et al., 2021), improved representations of tidal mixing (Green & Huber, 2013; Lohmann, 2020), might be required for providing more realistic climatic response for the Miocene.

In conclusion, our understanding of Miocene climatic, oceanic, and biogeochemical changes on broad temporal and spatial scales is still developing. By investigating this time interval, many lessons can be learned, such as the cause and effects of highly elevated temperatures occurred during the MCO. Improved understanding of how key components of the Earth system works under varying background conditions enable us to answer such fundamental questions as whether broad warming patterns can be obtained at relatively moderate atmospheric CO<sub>2</sub> concentration, a particularly pertinent issue as we already enter uncharted territory of elevated atmospheric CO<sub>2</sub> at present. Simulating various scenarios in climate models as well as synthesizing the existing and impending data on Miocene temperature, atmospheric CO<sub>2</sub>, tectonic evolution, ice sheet dynamics, and atmospheric and ocean circulation allows us improve our current understanding.

## Bibliography

- Aagaard, K., & Carmack, E. C. (1994). The Arctic Ocean and climate: A perspective. In O. M. Johannessen, R. D. Muench & J. E. Overland (Eds.), *The polar oceans and their role in shaping the global environment*, Geophysical Monograph Series (Vol. 85, pp. 5-20). Washington, DC: American Geophysical Union. <https://doi.org/10.1029/GM085>
- Bartoli, G., Sarnthein, M., Weinelt, M., Erlenkeuser, H., Garbe-Schönberg, D., & Lea, D. W. (2005). Final closure of Panama and the onset of northern hemisphere glaciation. *Earth and Planetary Science Letters*, 237(1-2), 33-44. <https://doi.org/10.1016/j.epsl.2005.06.020>
- Beerling, D. J., Fox, A., & Anderson, C. W. (2009). Quantitative uncertainty analyses of ancient atmospheric CO<sub>2</sub> estimates from fossil leaves. *American Journal of Science*, 309, 775–787. <https://doi.org/10.2475/09.2009.01>
- Beerling, D. J. & Royer, D. L. (2011). Convergent cenozoic CO<sub>2</sub> history. *Nature Geoscience* 4,418–420. <https://doi.org/10.1038/ngeo1186>
- Björk, G., Jakobsson, M., Rudels, B., Swift, J. H., Anderson, L., Darby, D. A., Backman, J., Coakley, B., Winsor, P., Polyak, L. & Edwards, M. (2007). Bathymetry and deep-water exchange across the central Lomonosov Ridge at 88–89 N. *Deep Sea Research Part I: Oceanographic Research Papers*. 54(8):1197-208. <https://doi.org/10.1016/j.dsr.2007.05.010>
- Bradshaw, C. D., Lunt, D. J., Flecker, R., & Davies-Barnard, T. (2015). Disentangling the roles of late Miocene paleogeography and vegetation– implications for climate sensitivity. *Palaeogeography Palaeoclimatology Palaeoecology*, 417, 17–34. <https://doi.org/10.1016/j.palaeo.2014.10.003>
- Bradshaw, C. D. (2021). *Miocene Climates*. Editor(s): David Alderton, Scott A. Elias, *Encyclopedia of Geology (Second Edition)*, Academic Press, Pages 486-496, ISBN 9780081029091. <https://doi.org/10.1016/B978-0-12-409548-9.12392-9>
- Broecker, W. S., & Denton, G. H. (1989). The role of ocean-atmosphere reorganizations in glacial cycles. *Geochimica et Cosmochimica Acta*, 53(10), 2465-2501.

## *Bibliography*

- [https://doi.org/10.1016/0016-7037\(89\)90123-3](https://doi.org/10.1016/0016-7037(89)90123-3)
- Burls, N.J., Bradshaw, C.D., De Boer, A.M., Herold, N., Huber, M., Pound, M., Donnadiu, Y., Farnsworth, A., Frigola, A., Gasson, E. and von der Heydt, A.S. (2021). Simulating Miocene warmth: insights from an opportunistic Multi-Model ensemble (MioMIP1). *Paleoceanography and Paleoclimatology*, p.e2020PA004054.
- Butt, F. A., Drange, H., Elverhøi, A., Otterå, O. H., & Solheim, A. (2002). Modelling Late Cenozoic isostatic elevation changes in the Barents Sea and their implications for oceanic and climatic regimes: preliminary results. *Quaternary Science Reviews*, 21(14-15), 1643-1660. [https://doi.org/10.1016/S0277-3791\(02\)00018-5](https://doi.org/10.1016/S0277-3791(02)00018-5)
- Butzin, M., Lohmann, G., & Bickert, T. (2011). Miocene ocean circulation inferred from marine carbon cycle modeling combined with benthic isotope records. *Paleoceanography*, 26, PA1203. <https://doi.org/10.1029/2009PA001901>
- Ceppi, P., McCoy, D. T. & Hartmann, D. L. (2016). Observational evidence for a negative shortwave cloud feedback in mid to high latitudes. *Geophys. Res. Lett.* 43, 1331–1339.
- Danek, C., Scholz, P., & Lohmann, G. (2019). Effects of high resolution and spinup time on modeled North Atlantic circulation. *Journal of Physical Oceanography*, 49(5), 1159-1181.
- Danilov, S., Sidorenko, D. Wang, Q., & Jung, T. (2017). The Finite-volume Sea ice–Ocean Model (FESOM2). *Geoscientific Model Development*, 10, pp.765-789.
- Darby, D. A. (2008). Arctic perennial ice cover over the last 14 million years. *Paleoceanography*, 23(1). <https://doi.org/10.1029/2007PA001479>.
- Davies, R., Cartwright, J., Pike, J., & Line, C. (2001). Early Oligocene initiation of North Atlantic deep water formation. *Nature*, 410(6831), 917. <https://doi.org/10.1038/35073551>
- Driscoll, N. W. & Haug, G. H. (1998). A short circuit in thermohaline circulation: A cause for northern hemisphere glaciation? *Science* 282, 436–438. <https://doi.org/10.1126/science.282.5388.436>
- Ehlers, B. M., & Jokat, W. (2013). Paleo-bathymetry of the northern North Atlantic and consequences for the opening of the Fram Strait. *Marine Geophysical Research*, 34(1), 25-43. <https://doi.org/10.1007/s11001-013-9165-9>
- Elsworth, G., Galbraith, E., Halverson, G., & Yang, S. (2017). Enhanced weathering and CO2 drawdown caused by latest Eocene strengthening of the Atlantic meridional overturning circulation. *Nature geoscience*, 10(3), 213. <https://doi.org/10.1038/ngeo2888>
- Engen, Ø., Faleide, J. I., & Dyreng, T. K. (2008). Opening of the Fram Strait gateway: A review of plate tectonic constraints. *Tectonophysics* 450(1-4):51-69. <https://doi.org/10.1016/j.tecto.2008.01.002>

- Eronen, J. T., Fortelius, M., Micheels, A., Portmann, F. T., Puolamäki, K., & Janis, C. M. (2012). Neogene aridification of the Northern Hemisphere. *Geology*, 40(9), 823-826.
- Flower, B. P., & Kennett, J. P. (1995). Middle Miocene deepwater paleoceanography in the southwest Pacific: relations with East Antarctic Ice Sheet development. *Paleoceanography*, 10(6), 1095-1112. <https://doi.org/10.1029/95PA02022>
- Frigola, A., Prange, M., & Schulz, M. (2018). Boundary conditions for the middle Miocene climate transition (MMCT v1.0). *Geoscientific Model Development*, 11(4), 1607–1626. <https://doi.org/10.5194/gmd-11-1607-2018>
- GISS (Goddard Institute for Space Studies) (2020). Global Mean CO2 Mixing Ratios (ppm): Observations. <http://data.giss.nasa.gov/modelforce/ghgases/Fig1A.ext.txt>. Accessed November 11, 2020
- Goldner, A., Herold, N., & Huber, M. (2014). The challenge of simulating the warmth of the mid-Miocene climatic optimum in CESM1. *Climate of the Past*, 10(2), 523–536. <https://doi.org/10.5194/cp-10-523-2014>
- Gong, X., Knorr, G., Lohmann, G., & Zhang, X. (2013). Dependence of abrupt Atlantic meridional ocean circulation changes on climate background states. *Geophysical Research Letters*, 40(14), 3698-3704. <https://doi.org/10.1002/grl.50701>
- Goosse, H., Kay, J.E., Armour, K.C., Bodas-Salcedo, A., Chepfer, H., Docquier, D., Jonko, A., Kushner, P.J., Lecomte, O., Massonnet, F. & Park, H.S. (2018). Quantifying climate feedbacks in polar regions. *Nature communications*, 9(1), 1-13.
- Gordon, A. L. (1981). Seasonality of Southern Ocean sea ice. *Journal of Geophysical Research: Oceans*, 86(C5), 4193-4197. <https://doi.org/10.1029/JC086iC05p04193>
- Green, J. A. M., & Huber, M. (2013). Tidal dissipation in the early Eocene and implications for ocean mixing. *Geophysical Research Letters*, 40(11), 2707-2713. <https://doi.org/10.1002/grl.50510>
- Haley, B. A., Frank, M., Spielhagen, R. F., & Eisenhauer, A. (2008). Influence of brine formation on Arctic Ocean circulation over the past 15 million years. *Nature Geoscience* 1(1):68-72. <https://doi.org/10.1038/ngeo.2007.5>
- Haug, G. H., & Tiedemann, R. (1998). Effect of the formation of the Isthmus of Panama on Atlantic Ocean thermohaline circulation. *Nature*, 393(6686), 673. <https://doi.org/10.1038/31447>
- Haug, G. H., Tiedemann, R., Zahn, R., & Ravelo, A. C. (2001). Role of Panama uplift on oceanic freshwater balance. *Geology*. 29(3):207-10.
- Haywood, A. M., Tindall, J. C., Dowsett, H. J., Dolan, A. M., Foley, K. M., Hunter, S. J., Hill,

## *Bibliography*

- D.J., Chan, W.L., Abe-Ouchi, A., Stepanek, C. & Lohmann, G. (2020). A return to large-scale features of Pliocene climate: The Pliocene Model Intercomparison Project Phase 2. *Climate of the Past Discussions*, 16, 2095–2123. <https://doi.org/10.5194/cp-2019-145>
- Hegewald, A., & Jokat, W. (2013). Relative sea level variations in the Chukchi region-Arctic Ocean-since the late Eocene. *Geophysical Research Letters*, 40(5), 803-807. <http://dx.doi.org/10.1002/GRL.50182>
- Held, I. M., & Soden, B. J. (2006). Robust response of the hydrological cycle to global warming. *Journal of Climate* 19,5686-5699. <https://doi.org/10.1175/JCLI3990.1>
- Herold, N., Seton, M., Müller, R. D., You, Y., & Huber, M. (2008). Middle Miocene tectonic boundary conditions for use in climate models. *Geochemistry, Geophysics, Geosystems*, 9(10). <https://doi.org/10.1029/2008GC002046>
- Herold, N., Huber, M., Greenwood, D. R., Müller, R. D., & Seton, M. (2011). Early to middle Miocene monsoon climate in Australia. *Geology*, 39, 3–6. <https://doi.org/10.1130/G31208.1>
- Hochmuth, K., Gohl, K., Leitchenkov, G., Sauermilch, I., Whittaker, J.M., Uenzelmann-Neben, G., Davy, B. and De Santis, L., (2020a). The Evolving Paleobathymetry of the Circum-Antarctic Southern Ocean Since 34 Ma: A Key to Understanding Past Cryosphere-Ocean Developments. *Geochemistry, Geophysics, Geosystems*, 21(8), e2020GC009122.
- Hochmuth, K., Paxman, G. J. G., Gohl, K., Jamieson, S. S. R., Leitchenkov, G. L., Bentley, M. J., Ferraccioli, F., Sauermilch, I., Whittaker, J., Uenzelmann-Neben, G. & Davy, B. (2020b). Combined palaeotopography and palaeobathymetry of the Antarctic continent and the Southern Ocean since 34 Ma. *PANGAEA*, <https://doi.pangaea.de/10.1594/PANGAEA.923109>
- Holbourn, A. E., Kuhnt, W., Clemens, S. C., Kochhann, K. G. D., Jahnck, J., Löffers, J., & Andersen, N. (2018). Late Miocene climate cooling and intensification of southeast Asian winter monsoon. *Nature Communications*, 9, 1584. <https://doi.org/10.1038/s41467-018-03950-1>
- Hossain, A., Knorr, G., Lohmann, G., Stärz, M. & Jokat, W., (2020). Simulated thermohaline fingerprints in response to different Greenland-Scotland Ridge and Fram Strait subsidence histories. *Paleoceanography and Paleoclimatology*, 35(7), p.e2019PA003842. <https://doi.org/10.1029/2019PA003842>
- Hossain, A., Knorr, G., Jokat, W., & Lohmann, G. (2021). Opening of the Fram Strait led to the establishment of a modern-like three-layer stratification in the Arctic Ocean during

- the Miocene. *arktos*, 1-12. <https://doi.org/10.1007/s41063-020-00079-8>
- Hossain, A., Knorr, G., Jokat, W., Lohmann, G., Hochmuth, K., Gierz, P., & Gohl, K. (2022). The impact of different atmospheric CO<sub>2</sub> concentrations on large scale Miocene temperature signatures. *Paleoceanography and Paleoclimatology*, in revision.
- Huang, X., Gohl, K., & Jokat, W. (2014). Variability in Cenozoic sedimentation and paleo-water depths of the Weddell Sea basin related to pre-glacial and glacial conditions of Antarctica. *Global and Planetary Change*, 118, 25-41. <https://doi.org/10.1016/j.gloplacha.2014.03.010>
- Huang, X., Stürz, M., Gohl, K., Knorr, G., & Lohmann, G. (2017). Impact of Weddell Sea shelf progradation on Antarctic bottom water formation during the Miocene. *Paleoceanography*, 32(3), 304-317. <https://doi.org/10.1002/2016PA002987>
- Huber, M., & Caballero, R. (2011). The early Eocene equable climate problem revisited. *Climate of the Past*, 7(2), 603–633. <https://doi.org/10.5194/cp-7-603-2011>
- Hutchinson, D. K., Coxall, H. K., O'Regan, M., Nilsson, J., Caballero, R., & de Boer, A. M. (2019). Arctic closure as a trigger for Atlantic overturning at the Eocene-Oligocene Transition. *Nature communications*, 10(1), 1-9.
- IPCC (Intergovernmental Panel on Climate Change) (2013). *Climate change 2013: The physical science basis. Working Group I contribution to the IPCC Fifth Assessment Report*. Cambridge, United Kingdom: Cambridge University Press. <https://www.ipcc.ch/report/ar5/wg1/>. Accessed November 11, 2020
- Jakobsson, M., Backman, J., Rudels, B., Nycander, J., Frank, M., Mayer, L., Jokat, W., Sangiorgi, F., O'Regan, M., Brinkhuis, H., King, J., & Moran, K. (2007). The early Miocene onset of a ventilated circulation regime in the Arctic Ocean. *Nature*, 447(7147), 986. <https://doi.org/10.1038/nature05924>
- Jokat, W., Geissler, W., & Voss, M. (2008). Basement structure of the north-western Yermak Plateau. *Geophysical research letters*, 35(5). <https://doi.org/10.1029/2007GL032892>
- Jokat, W., Lehmann, P., Damaske, D., & Nelson, J. B. (2016). Magnetic signature of North-East Greenland, the Morris Jesup Rise, the Yermak Plateau, the central Fram Strait: constraints for the rift/drift history between Greenland and Svalbard since the Eocene. *Tectonophysics*, 691, 98-109. <https://doi.org/10.1016/j.tecto.2015.12.002>
- Jungclaus, J. H., Keenlyside, N., Botzet, M., Haak, H., Luo, J. J., Latif, M., Marotzke, J., Mikolajewicz, U., & Roeckner, E. (2006). Ocean circulation and tropical variability in the coupled model ECHAM5/MPI-OM. *Journal of climate*, 19(16), 3952-3972. <https://doi.org/10.1175/JCLI3827.1>

## *Bibliography*

- Jungclauss, J. H., Lorenz, S. J., Timmreck, C., Reick, C. H., Brovkin, V., Six, K., Segschneider, J., Giorgetta, M.A., Crowley, T.J., Pongratz, J., & Krivova, N. A. (2010). Climate and carbon-cycle variability over the last millennium. *Climate of the Past*, 6, 723-737. doi:10.5194/cp-6-723-2010.
- Kageyama, M., Harrison, S. P., Kapsch, M.-L., Lofverstrom, M., Lora, J. M., Mikolajewicz, U., Sherriff-Tadano, S., Vadsaria, T., Abe-Ouchi, A., Bouttes, N., Chandan, D., Gregoire, L. J., Ivanovic, R. F., Izumi, K., LeGrande, A. N., Lhardy, F., Lohmann, G., Morozova, P. A., Ohgaito, R., Paul, A., Peltier, W. R., Poulsen, C. J., Quiquet, A., Roche, D. M., Shi, X., Tierney, J. E., Valdes, P. J., Volodin, E., and Zhu, J. (2021). The PMIP4 Last Glacial Maximum experiments: preliminary results and comparison with the PMIP3 simulations, *Clim. Past*, 17, 1065–1089, <https://doi.org/10.5194/cp-17-1065-2021>.
- Kennett, J.P. (1977). Cenozoic evolution of Antarctic glaciation, the circum- Antarctic Ocean, and their impact on global paleoceanography. *Journal of Geophysical Research* 82, 3843-3860.
- Knies, J., & Gaina, C. (2008). Middle Miocene ice sheet expansion in the Arctic: Views from the Barents Sea. *Geochemistry, Geophysics, Geosystems*, 9(2). <https://doi.org/10.1029/2007GC001824>
- Knies, J., Mattingsdal, R., Fabian, K., Grøsfjeld, K., Baranwal, S., Husum, K., De Schepper, S., Vogt, C., Andersen, N., Matthiessen, J., & Andreassen, K. (2014). Effect of early Pliocene uplift on late Pliocene cooling in the Arctic–Atlantic gateway. *Earth and Planetary Science Letters*, 387, 132-144. <https://doi.org/10.1016/j.epsl.2013.11.007>
- Knorr, G., Butzin, M., Micheels, A., & Lohmann, G. (2011). A warm Miocene climate at low atmospheric CO<sub>2</sub> levels. *Geophysical Research Letters*, 38(20), L20701. <https://doi.org/10.1029/2011GL048873>
- Knorr, G., & Lohmann, G. (2014). Climate warming during Antarctic ice sheet expansion at the Middle Miocene transition. *Nature Geoscience*, 7, 376–381. <https://doi.org/10.1038/ngeo2119>
- Knutti, R., Rugenstein, M. A. A., & Hegerl, G. C. (2017). Beyond equilibrium climate sensitivity. *Nature Geoscience*, 10(10), 727–736. <https://doi.org/10.1038/ngeo3017>
- Koldunov, N. V., Aizinger, V., Rakowsky, N., Scholz, P., Sidorenko, D., Danilov, S., & Jung, T. (2019). Scalability and some optimization of the Finite-volume Sea ice-Ocean Model, Version 2.0 (FESOM2). *Geoscientific Model Development*, 12, pp.3991-4012.
- Krapp, M., & Jungclauss, J. H. (2011). The Middle Miocene climate as modeled in an atmosphere-ocean-biosphere model. *Climate of the Past*, 7(4), 1169–1188.

- <https://doi.org/10.5194/cp-7-1169-2011>
- Kristoffersen, Y. (1990). On the tectonic evolution and paleoceanographic significance of the Fram Strait gateway. In: Bleil U, Thiede J (eds) Geological history of the Polar Oceans: Arctic versus Antarctic. Kluwer Academic Publishers, Dordrecht, pp 63–76. [https://doi.org/10.1007/978-94-009-2029-3\\_4](https://doi.org/10.1007/978-94-009-2029-3_4)
- Krylov, A. A., Andreeva, I. A., Vogt, C., Backman, J., Krupskaya, V. V., Grikurov, G. E., Moran, K. & Shoji, H. (2008). A shift in heavy and clay mineral provenance indicates a middle Miocene onset of a perennial sea ice cover in the Arctic Ocean. *Paleoceanography*, 23(1). <https://doi.org/10.1029/2007PA001497>.
- Krschner, W. M., Kvaek, Z., & Dilcher, D. L. (2008). The impact of Miocene atmospheric carbon dioxide fluctuations on climate and the evolution of terrestrial ecosystems. *Proceedings of the National Academy of Sciences of the United States of America*, 105, 449–453. <https://doi.org/10.1073/pnas.0708588105>
- Laberg, J. S., Stoker, M. S., Dahlgren, K. T., de Haas, H., Haflidason, H., Hjelstuen, B. O., Nielsen, T., Shannon, P.M., Vorren, T.O., van Weering, T.C., & Ceramicola, S. (2005). Cenozoic alongslope processes and sedimentation on the NW European Atlantic margin. *Marine and Petroleum Geology*, 22(9-10), 1069-1088. <https://doi.org/10.1016/j.marpetgeo.2005.01.008>
- Lainé, A., Yoshimori, M., & Abe-Ouchi, A. (2016). Surface Arctic amplification factors in CMIP5 models: land and oceanic surfaces and seasonality. *J. Clim.* 29,3297–3316.
- Lawrence, K. T., Coxall, H. K., Sosdian, S., & Steinthorsdottir, M. (2021). Navigating Miocene ocean temperatures for insights into the future. *EOS: Transactions*, 102. <https://doi.org/10.1029/2021EO210528>.
- Lear, C. H., Rosenthal, Y., Wright, J. D. (2003). The closing of a seaway: ocean water masses and global climate change. *Earth and Planetary Science Letters* 210, 425-436.
- Lohmann, G., Pfeiffer, M., Laepple, T., Leduc, G., & Kim, J. H. (2013). A model-data comparison of the Holocene global sea surface temperature evolution. *Climate of the Past*, (9), 1807-1839. <https://doi.org/10.5194/cp-9-1807-2013>
- Lohmann, G., Butzin, M., & Bickert, T. (2015). Effect of vegetation on the late Miocene Ocean circulation. *Journal of Marine Science and Engineering*, 3(4), 1311–1333. <https://doi.org/10.3390/jmse3041311>
- Lohmann, G. (2020). Temperatures from Energy Balance Models: the effective heat capacity matters. *Earth System Dynamics*, 11(4), 1195-1208, <https://doi.org/10.5194/esd-11-1195-2020>.

## *Bibliography*

- Lohmann, G., Butzin, M., Eissner, N., Shi, X., & Stepanek, C. (2020). Abrupt climate and weather changes across time scales. *Paleoceanography and Paleoclimatology*, 35(9), e2019PA003782, <https://doi.org/10.1029/2019PA003782>.
- Lohmann, G., Knorr, G., Hossain, A. & Stepanek, C. (2022). Effects of CO<sub>2</sub> and ocean mixing on Miocene and Pliocene temperature gradients, *Paleoceanography and Paleoclimatology*, 35(7), <https://doi.org/10.1029/2020PA003953>.
- Lunt, D. J., Foster, G. L., Haywood, A. M., & Stone, E. J. (2008). Late Pliocene Greenland glaciation controlled by a decline in atmospheric CO<sub>2</sub> levels. *Nature*, 454(7208), 1102–1105.
- Lunt, D. J., Bragg, F., Chan, W.-L., Hutchinson, D. K., Ladant, J.-B., Morozova, P., Niezgodzki, I., Steinig, S., Zhang, Z., Zhu, J., Abe-Ouchi, A., Anagnostou, E., de Boer, A. M., Coxall, H. K., Donnadieu, Y., Foster, G., Inglis, G. N., Knorr, G., Langebroek, P. M., Lear, C. H., Lohmann, G., Poulsen, C. J., Sepulchre, P., Tierney, J. E., Valdes, P. J., Volodin, E. M., Dunkley Jones, T., Hollis, C. J., Huber, M., and Otto-Bliesner, B. L. (2021). DeepMIP: model intercomparison of early Eocene climatic optimum (EECO) large-scale climate features and comparison with proxy data, *Clim. Past*, 17, 203–227, <https://doi.org/10.5194/cp-17-203-2021>
- Marshall, L. G., Webb, S. D., Sepkoski, J. J., & Raup, D. M. (1982). Mammalian evolution and the great American interchange. *Science*, 215(4538), 1351–1357.
- Marsland, S. J., Haak, H., Jungclaus, J. H., Latif, M., & Röske, F. (2003). The Max-Planck-Institute global ocean/sea ice model with orthogonal curvilinear coordinates. *Ocean modelling*, 5(2), 91–127. [https://doi.org/10.1016/S1463-5003\(02\)00015-X](https://doi.org/10.1016/S1463-5003(02)00015-X)
- Micheels, A., A. A. Bruch, & V. Mosbrugger (2009), Miocene climate modelling sensitivity experiments for different CO<sub>2</sub> concentrations, *Palaeontol. Electron.*, 12, 1–20.
- Mikolajewicz, U., & Crowley, T. J. (1997). Response of a coupled ocean/energy balance model to restricted flow through the Central American Isthmus. *Paleoceanography*, 12(3), 429–441. <https://doi.org/10.1029/96PA03542>
- Miller, K. G. (1992). Middle Eocene to Oligocene stable isotopes, climate, and deep-water history: the terminal Eocene event? In Prothero, D. R. & Berggren, W. A. (Eds.), *Eocene-Oligocene climatic and biotic evolution*. Princeton Univ. Press, Princeton, NJ, 160–177.
- Moran, K., Backman, J., Brinkhuis, H., Clemens, S. C., Cronin, T., Dickens, G. R., Eynaud, F., Gattacceca, J., Jakobsson, M., Jordan, R. W., Kaminski, M., King, J., Koc, N., Krylov, A., Martinez, N., Matthiessen, J., McInroy, D., Moore, T. C., Onodera, J., O'Regan, A. M., Pälike, H., Rea, B., Rio, D., Sakamoto, T., Smith, D.C., Stein, R., St. John, K., Suto, I.,

- Suzuki, N., Takahashi, K., Watanabe, M., Yamamoto, M., Frank, M., Jokat, W., Kristoffersen, Y. (2006). The cenozoic palaeoenvironment of the arctic ocean. *Nature*, 441(7093), 601. <https://doi.org/10.1038/nature04800>
- Müller, R. D., Seton, M., Zahirovic, S., Williams, S. E., Matthews, K. J., Wright, N. M., Shephard, G.E., Maloney, K.T., Barnett-Moore, N., Hosseinpour, M. & Bower, D. J. (2016). Ocean Basin evolution and global-scale plate reorganization events since Pangea breakup. *Annual Review of Earth and Planetary Sciences*, 44(1), 107–138. doi: 10.1146/annurev-earth-060115-012211
- Myhre, A. M., Thiede, J., Firth, J. V., Ahagon, N., Black, K. S., Bloemendal, J., Brass, G. W., Bristow, J. F., Chow, N., Cremer, M., Davis, L. (1995) Site 909. In *Proceedings of the Ocean Drilling Program. Initial reports 1995 (Vol. 151, pp. 159-220)*. Ocean Drilling Program.
- NASA (2020), Carbon Dioxide. <https://climate.nasa.gov/vital-signs/carbon-dioxide/>. November 11, 2020.
- Otto-Bliesner, B. L., Brady, E. C., Zhao, A., Brierley, C. M., Axford, Y., Capron, E., Govin, A., Hoffman, J. S., Isaacs, E., Kageyama, M., Scussolini, P., Tzedakis, P. C., Williams, C. J. R., Wolff, E., Abe-Ouchi, A., Braconnot, P., Ramos Buarque, S., Cao, J., de Vernal, A., Guarino, M. V., Guo, C., LeGrande, A. N., Lohmann, G., Meissner, K. J., Menviel, L., Morozova, P. A., Nisancioglu, K. H., O'ishi, R., Salas y Méliá, D., Shi, X., Sicard, M., Sime, L., Stepanek, C., Tomas, R., Volodin, E., Yeung, N. K. H., Zhang, Q., Zhang, Z., and Zheng, W. (2021). Large-scale features of Last Interglacial climate: results from evaluating the lig127k simulations for the Coupled Model Intercomparison Project (CMIP6)–Paleoclimate Modeling Intercomparison Project (PMIP4), *Clim. Past*, 17, 63–94, <https://doi.org/10.5194/cp-17-63-2021>.
- Pagani, M., Zachos, J. C., Freeman, K. H., Tipple, B., & Bohaty, S. (2005). Marked decline in atmospheric carbon dioxide concentrations during the Paleogene. *Science*, 309(5734), 600-603. <https://doi.org/10.1126/science.1110063>
- Pagani, M., Huber, M., Liu, Z., Bohaty, S. M., Henderiks, J., Sijp, W., Krishnan, S. & DeConto, R. M. (2011). The role of carbon dioxide during the onset of Antarctic glaciation. *science*, 334(6060), 1261-1264. <https://doi.org/10.1126/science.1203909>
- Pagani, M., Huber, M., Liu, Z., Bohaty, S. M., Henderiks, J., Sijp, W., Krishnan, S., & DeConto, R. M. (2013) The role of carbon dioxide during the onset of Antarctic glaciation. *Science* 334(6060):1261-4. <https://doi.org/10.1126/science.1203909>
- Parnell-Turner, R., White, N., Henstock, T., Murton, B., MacLennan, J., & Jones, S. M. (2014).

## *Bibliography*

- A continuous 55-million-year record of transient mantle plume activity beneath Iceland. *Nature Geoscience*, 7(12), 914-919. <https://doi.org/10.1038/ngeo2281>
- Paxman, G. J. G., Jamieson, S. S. R., Hochmuth, K., Gohl, K., Bentley, M. J., Leitchenkov, G., & Ferraccioli, F. (2019). Reconstructions of Antarctic topography since the Eocene–Oligocene boundary. *Palaeogeography, Palaeoclimatology, Palaeoecology* 535, 109346.
- Pithan, F., & Mauritsen, T. (2014). Arctic amplification dominated by temperature feedbacks in contemporary climate models. *Nature Geosciences*, 7, 181–184. <https://doi.org/10.1038/ngeo2071>
- Polzin, K. L., Toole, J. M., Ledwell, J. R., & Schmitt, R. W. (1997). Spatial Variability of Turbulent Mixing in the Abyssal Ocean. *Science* 276, 93-96.
- Poore, H. R., Samworth, R., White, N. J., Jones, S. M., & McCave, I. N. (2006). Neogene overflow of northern component water at the Greenland-Scotland Ridge. *Geochemistry, Geophysics, Geosystems*, 7(6). <https://doi.org/10.1029/2005GC001085>
- Pratt, L. J., & Spall, M. A. (2008) Circulation and exchange in choked marginal seas. *Journal of Physical Oceanography*, 38(12), 2639-2661. <https://doi.org/10.1175/2008JPO3946.1>
- Raddatz, T. J., Reick, C. H., Knorr, W., Kattge, J., Roeckner, E., Schnur, R., Schnitzler, K.G., Wetzel, P. & Jungclaus, J. (2007). Will the tropical land biosphere dominate the climate–carbon cycle feedback during the twenty-first century? *Climate Dynamics*, 29(6), 565–574. <https://doi.org/10.1007/s00382-007-0247-8>
- Rebesco, M., Hernández-Molina, F.J., Van Rooij, D., & Wåhlin, A. (2014). Contourites and associated sediments controlled by deep-water circulation processes: state-of-the-art and future considerations. *Marine Geology* 352, 111-154.
- Roeckner, E., Bäuml, G., Bonaventura, L., Brokopf, R., Esch, M., Giorgetta, M., Hagemann, S., Kirchner, I., Kornblueh, L., Manzini, E., & Rhodin, A. (2003). The atmospheric general circulation model ECHAM 5. PART I: Model description. Report / MPI für Meteorologie, 349. <http://hdl.handle.net/11858/00-001M-0000-0012-0144-5>
- Royer, D. L. (2001). Stomatal density and stomatal index as indicators of paleoatmospheric CO<sub>2</sub> concentration. *Review of Palaeobotany and Palynology*, 114, 1–28. [https://doi.org/10.1016/S0034-6667\(00\)00074-9](https://doi.org/10.1016/S0034-6667(00)00074-9)
- Ruddiman, W. F. (2010). A paleoclimatic enigma?. *Science*, 328(5980), 838-839.
- Rudels, B. (1995). The thermohaline circulation of the Arctic Ocean and the Greenland Sea. *Philosophical Transactions. Physical Sciences and Engineering* 352, 287-299. <https://doi.org/10.1098/rsta.1995.0071>
- Rudels, B., Björk, G., Nilsson, J., Winsor, P., Lake, I., & Nohr, C. (2005). The interaction

- between waters from the Arctic Ocean and the Nordic Seas north of Fram Strait and along the East Greenland Current: results from the Arctic Ocean-02 Oden expedition. *Journal of Marine Systems*, 55(1-2), 1-30. <https://doi.org/10.1016/j.jmarsys.2004.06.008>
- Sangiorgi, F., Brumsack, H. J., Willard, D. A., Schouten, S., Stickley, C. E., O'Regan, M., ... & Brinkhuis, H. (2008). A 26 million year gap in the central Arctic record at the greenhouse-icehouse transition: Looking for clues. *Paleoceanography*, 23(1). <https://doi.org/10.1029/2007PA001477>
- Sauermilch, I., Whittaker, J. M., Klocker, A., Munday, D. R., Hochmuth, K., Bijl, P. K., & LaCasce, J. H. (2021). Gateway-driven weakening of ocean gyres leads to Southern Ocean cooling. *Nature communications*, 12(1), 1-8. <https://doi.org/10.1038/s41467-021-26658-1>
- Schlosser, P., Kromer, B., Ekwurzel, B., Bönisch, G., McNichol, A., Schneider, R., Von Reden, K., Östlund, H.G. & Swift, J. H. (1997). The first trans-Arctic 14C section: comparison of the mean ages of the deep waters in the Eurasian and Canadian basins of the Arctic Ocean. *Nuclear Instruments and Methods in Physics Research Section B: Beam Interactions with Materials and Atoms*, 123(1-4), 431-437.
- Scholz P., Sidorenko D., Gurses O., Danilov S., Koldunov N., Wang Q., Sein, D., Smolentseva, M., Rakowsky, N. & Jung, T. (2019). Assessment of the Finite Volume Sea Ice Ocean Model (FESOM2.0), Part I: Description of selected key model elements and comparison to its predecessor version. *Geoscientific Model Development Discussions*. <https://doi.org/10.5194/gmd-2018-329>, 1–42.
- Seki, O., Foster, G. L., Schmidt, D. N., Mackensen, A., Kawamura, K., & Pancost, R. D. (2010). Alkenone and boron-based Pliocene pCO<sub>2</sub> records. *Earth and Planetary Science Letters*, 292(1-2), 201-211.
- Shevenell, A. E., Kennett, J. P., & Lea, D. W. (2004). Middle Miocene Southern Ocean cooling and antarctic cryosphere expansion. *Science*, 305(5691), 1766–1770. <https://doi.org/10.1126/science.11100061>
- Sidorenko, D., Rackow, T., Jung, T., Semmler, T., Barbi ,D., Danilov, S., Dethloff ,K., Dorn, W., Fieg, K., Goessling, H. F., Handorf, D., Harig, S., Hiller, W., Juricke, S., Losch, M., Schröter, J., Sein, D. V., & Wang, Q. (2015). Towards multi-resolution global climate modeling with ECHAM6–FESOM. Part I: model formulation and mean climate. *Climate Dynamics*, 44(3-4), pp.757-780.
- Sidorenko, D., Goessling, H. F., Koldunov, N., Scholz, P., Danilov, S., Barbi ,D., Cabos, W., Gurses, O., Harig, S., Hinrichs, C., Juricke, S., Lohmann, G., Losch, M., Mu, L., Rackow,

## *Bibliography*

- T., Rakowsky, N., Sein, D., Semmler, T., Shi, X., Stepanek, C., Streffing, J., Wang, Q., Wekerle, C., Yang, H., & Jung, T. (2019). Evaluation of FESOM2.0 coupled to ECHAM6.3: Preindustrial and HighResMIP simulations. *Journal of Advances in Modeling Earth Systems*, 11, pp.3794-3815.
- Soden, B. J. & Held, I. M. (2006). An assessment of climate feedbacks in coupled ocean-atmosphere models. *J. Clim.* 19, 3354–3360.
- Sosdian, S. M., Greenop, R., Hain, M. P., Foster, G. L., Pearson, P. N., & Lear, C. H. (2018). Constraining the evolution of Neogene ocean carbonate chemistry using the boron isotope pH proxy. *Earth and Planetary Science Letters*, 498, 362–376. <https://doi.org/10.1016/j.epsl.2018.06.017>
- Sosdian, S. M., Babila, T. L., Greenop, R., Foster, G. L., & Lear, C. H. (2020). ocean carbon storage across the middle Miocene: A new interpretation for the Monterey event. *Nature Communications*, 11, 134. <https://doi.org/10.1038/s41467-019-13792-0>
- Spicer, R. A., Herman, A. B., & Kennedy, E. M. (2004). The foliar physiognomic record of climatic conditions during dormancy: CLAMP and the cold month mean temperature. *J. Geol.*, 112, 685–702. <https://doi.org/10.1086/424579>
- St. John, K. (2008). Cenozoic ice-rafting history of the central Arctic Ocean: Terrigenous sands on the Lomonosov Ridge. *Paleoceanography*, 23, PA1S05. <https://doi.org/10.1029/2007PA001483>.
- Stärz, M., Lohmann, G., & Knorr, G. (2016). The effect of a dynamic soil scheme on the climate of the mid-Holocene and the Last Glacial Maximum. *Climate of the Past*, 12(1). <https://doi.org/10.5194/cp-12-151-2016>
- Stärz, M., Jokat, W., Knorr, G., & Lohmann, G. (2017). Threshold in North Atlantic-Arctic Ocean circulation controlled by the subsidence of the Greenland-Scotland Ridge. *Nature communications*, 8, 15681. <https://doi.org/10.1038/ncomms15681>
- Steckler, M. S., & Watts, A. B. (1978). Subsidence of the Atlantic-type continental margin off New York. *Earth and planetary science letters*, 41(1), 1-13.
- Steele, M., Morley, R., & Ermold, W. (2001). PHC: A global ocean hydrography with a high-quality Arctic Ocean. *Journal of Climate*, 14(9), 2079-2087, [https://doi.org/10.1175/1520-0442\(2001\)014<2079:PAGOHW>2.0.CO;2](https://doi.org/10.1175/1520-0442(2001)014<2079:PAGOHW>2.0.CO;2).
- Stein, R., Jokat, W., Niessen, F., & Weigelt, E. (2015). Exploring the long-term Cenozoic Arctic Ocean climate history: a challenge within the International Ocean Discovery Program (IODP). *arktos*, 1(1), 3. doi:10.1007/s41063-015-0012-x.
- Stein, R., Fahl, K., Schreck, M., Knorr, G., Niessen, F., Forwick, M., Gebhardt, C., Jensen, L.,

- Kaminski, M., Kopf, A. & Matthiessen, J. (2016). Evidence for ice-free summers in the late Miocene central Arctic Ocean. *Nature Communications*, 7, 11148. <https://doi.org/10.1038/ncomms11148>
- Stein, U., & Alpert, P. I. N. H. A. S. (1993). Factor separation in numerical simulations. *Journal of the Atmospheric Sciences*, 50(14), 2107-2115. [https://doi.org/10.1175/1520-0469\(1993\)050<2107:FSINS>2.0.CO;2](https://doi.org/10.1175/1520-0469(1993)050<2107:FSINS>2.0.CO;2)
- Steinthorsdottir, M., Coxall, H. K., De Boer, A. M., Huber, M., Barbolini, N., Bradshaw, C.D., Burls, N.J., Feakins, S.J., Gasson, E., Henderiks, J. & Holbourn, A.E. (2021). The Miocene: The future of the past. *Paleoceanography and Paleoclimatology*, 36(4), p.e2020PA004037.
- Stepanek, C., & Lohmann, G. (2012). Modelling mid-Pliocene climate with COSMOS. *Geosci. Model Dev.*, 5, 1221-1243. <https://doi.org/10.5194/gmd-5-1221-2012>
- Stevens, B., Giorgetta, M., Esch, M., Mauritsen, T., Crueger, T., Rast, S. Salzmann, M., Schmidt, H., Bader, J., Block, K. & Brokopf, R.(2013). Atmospheric component of the MPI-M Earth System Model: ECHAM6. *Journal of Advances in Modeling Earth Systems*, 5, 146–172. <https://doi.org/10.1002/jame.20015>
- Stoll, H. M., Guitian, J., Hernandez-Almeida, I., Mejia, L. M., Phelps, S., Polissar, P., Rosenthal, Y., Zhang, H. & Ziveri, P. (2019). Upregulation of phytoplankton carbon concentrating mechanisms during low CO<sub>2</sub> glacial periods and implications for the phytoplankton pCO<sub>2</sub> proxy. *Quaternary Science Reviews*, 208, 1-20.
- Straume, E. O., Gaina, C., Medvedev, S., & Nisancioglu, K. H. (2020). Global cenozoic paleobathymetry with a focus on the northern hemisphere oceanic gateways. *Gondwana Research*, 86, 126-143. <https://doi.org/10.1016/j.gr.2020.05.011>
- Super, J. R., Thomas, E., Pagani, M., Huber, M., O'Brien, C., & Hull, P. M. (2018). North Atlantic temperature and pCO<sub>2</sub> coupling in the early-middle Miocene. *Geology*, 46(6), 519–522. <https://doi.org/10.1130/G40228.1>
- Super, J. R., Thomas, E., Pagani, M., Huber, M., O'Brien, C. L., & Hull, P. M. (2020). Miocene Evolution of North Atlantic Sea Surface Temperature. *Paleoceanography and Paleoclimatology*, 35(5). <https://doi.org/10.1029/2019PA003748>
- Talwani, M., Udintsev, G. & White, S. M. (1976). *Initial Reports of the Deep Sea Drilling Project, Vol. 38*. Dublin, Ireland to Amsterdam, The Netherlands. US Government Printing Office.
- Tanhua, T., Jones, E. P., Jeansson, E., Jutterström, S., Smethie Jr, W. M., Wallace, D. W., & Anderson, L. G. (2009). Ventilation of the Arctic Ocean: Mean ages and inventories of

## *Bibliography*

- anthropogenic CO<sub>2</sub> and CFC-11. *Journal of Geophysical Research: Oceans*, 114(C1).
- Terai, C. R., Zelinka, M. & Klein, S. A. (2016). Constraining the low-cloud optical depth feedback at middle and high latitudes using satellite observations. *J. Geophys. Res. Atmos.* 121, 9696–9716.
- Thiede, J., & Myhre, A. M. (1996). The palaeoceanographic history of the North Atlantic–Arctic gateways: synthesis of the Leg 151 drilling results. In *Proceedings of the Ocean Drilling Program, Scientific Results (Vol. 151, pp. 645-658)*. Ocean Drilling Program College Station, TX.
- Thompson, B., Nilsson, J., Nycander, J., Jakobsson, M., & Döös, K. (2010). Ventilation of the Miocene Arctic Ocean: An idealized model study. *Paleoceanography*, 25(4). <https://doi.org/10.1029/2009PA001883>.
- Thompson, B., Jakobsson, M., Nilsson, J., Nycander, J., & Döös, K. (2012). A model study of the first ventilated regime of the Arctic Ocean during the early Miocene. *Polar Research*, 31(1), 10859. <https://doi.org/10.3402/polar.v31i0.10859>
- USEPA (United States Environmental Protection Agency) (2016). Climate Change Indicators: Sea Surface Temperature. <https://www.epa.gov/climate-indicators/climate-change-indicators-sea-surface-temperature#ref8>. Accessed 11 November 2020
- Utescher, T., & Mosbrugger, V. (2007). Eocene vegetation patterns reconstructed from plant diversity - A global perspective. *Palaeogeography, Palaeoclimatology, Palaeoecology*, 247, 243-271. <https://doi.org/10.1016/j.palaeo.2006.10.022>
- Valcke, S. (2013). The OASIS3 coupler: A European climate modelling community software. *Geoscientific Model Development*, 6(2), 373–388. <https://doi.org/10.5194/gmd-6-373-2013>
- Valdes, P. J., Sellwood, B. W., & Price, G. D. (1996). The concept of Cretaceous equability. *Palaeoclim.: Data Model.*, 1, 139-158.
- Via, R. K., & Thomas, D. J. (2006). Evolution of Atlantic thermohaline circulation: Early Oligocene onset of deep-water production in the North Atlantic. *Geology*, 34(6), 441-444. <https://doi.org/10.1130/G22545.1>
- von der Heydt, A., & Dijkstra, H. A. (2006). Effect of ocean gateways on the global ocean circulation in the late Oligocene and early Miocene. *Paleoceanography*, 21, PA1011. <https://doi.org/10.1029/2005PA001149>
- von Appen, W. J., Schauer, U., Somavilla, R., Bauerfeind, E., & Beszczynska-Möller, A. (2015). Exchange of warming deep waters across Fram Strait. *Deep Sea Research Part I: Oceanographic Research Papers*, 103, 86-100.

- Vorrath, M.-E., Müller, J., Rebolledo, L., Cárdenas, P., Shi, X., Esper, O., Opel, T., Geibert, W., Muñoz, P., Haas, C., Kuhn, G., Lange, C. B., Lohmann, G., and Mollenhauer, G. (2020). Sea ice dynamics in the Bransfield Strait, Antarctic Peninsula, during the past 240 years: a multi-proxy intercomparison study, *Clim. Past*, 16, 2459–2483, <https://doi.org/10.5194/cp-16-2459-2020>
- Waddell, L. M. & Moore, T. C. (2008). Salinity of the Eocene Arctic Ocean from oxygen isotope analysis of fish bone carbonate. *Paleoceanography*, 23(1). <https://doi.org/10.1029/2007PA001451>
- Webb, S. D. (2006). The great american biotic interchange: patterns and processes1. *Annals of the Missouri Botanical Garden*, 93(2), 245-257.
- Wei, W., & Lohmann, G. (2012). Simulated Atlantic multidecadal oscillation during the Holocene. *Journal of Climate*, 25(20), 6989-7002. <https://doi.org/10.1175/JCLI-D-11-00667.1>
- Weller, P., & Stein, R. (2008). Paleogene biomarker records from the central Arctic Ocean (Integrated Ocean Drilling Program Expedition 302): Organic carbon sources, anoxia, and sea surface temperature. *Paleoceanography*, 23(1). <https://doi.org/10.1029/2007PA001472>
- Woodruff, F., & Savin, S. M. (1989). Miocene deepwater oceanography. *Paleoceanography*, 4(1), 87-140. <https://doi.org/10.1029/PA004i001p00087>.
- Wright, J. D., & Miller, K. G. (1996). Control of North Atlantic deep water circulation by the Greenland-Scotland Ridge. *Paleoceanography*, 11(2), 157-170. <https://doi.org/10.1029/95PA03696>
- Zachos, J., Pagani, M., Sloan, L., Thomas, E. & Billups, K. (2001) Trends, rhythms, and aberrations in global climate 65 Ma to present. *Science* 292(5517):686-93. <https://doi.org/10.1126/science.1059412>
- Zachos, J. C., Dickens, G. R., & Zeebe, R. E. (2008). An early Cenozoic perspective on greenhouse warming and carbon-cycle dynamics. *nature*, 451(7176), 279-283. <https://doi.org/10.1038/nature06588>
- Zelinka, M. D., Klein, S. A. & Hartmann, D. L. (2012). Computing and partitioning cloud feedbacks using cloud property histograms. Part II: attribution to changes in cloud amount, altitude, and optical depth. *J. Clim.* 25, 3736–3754.
- Zhang, X., Lohmann, G., Knorr, G., & Xu, X. (2013). Different ocean states and transient characteristics in Last Glacial Maximum simulations and implications for deglaciation. *Climate of the Past*, 9(5), 2319-2333. <https://doi.org/10.5194/cp-9-2319-2013>

## *Bibliography*

- Zhu, J., & Poulsen, C. J. (2019). Quantifying the cloud particle-size feedback in an Earth System Model. *Geophysical Research Letters*, 46(19), 10910–10917. <https://doi.org/10.1029/2019GL083829>
- Zhu, J., Poulsen, C. J., & Tierney, J. E. (2019). Simulation of Eocene extreme warmth and high climate sensitivity through cloud feedbacks. *Science Advances*, 5(9), eaax1874. <https://doi.org/10.1126/sciadv.aax1874>

## Author Contributions

Author (A. H.) contributions of the following studies that have been either published (Hossain et al., 2020; 2021; Lohmann et al., 2022) or submitted (Hossain et al., 2022) are as follows:

1. Hossain, A., Knorr, G., Lohmann, G., Stürz, M., & Jokat, W., (2020). Simulated thermohaline fingerprints in response to different Greenland-Scotland Ridge and Fram Strait subsidence histories. *Paleoceanography and Paleoclimatology*, 35(7), p.e2019PA003842. <https://doi.org/10.1029/2019PA003842>
  - *Contributions: Conceptualization, Formal analysis, Investigation, Methodology, Software, Validation, Visualization, Writing - original draft*
2. Hossain, A., Knorr, G., Jokat, W., & Lohmann, G. (2021). Opening of the Fram Strait led to the establishment of a modern-like three-layer stratification in the Arctic Ocean during the Miocene. *arktos*, 1-12. <https://doi.org/10.1007/s41063-020-00079-8>
  - *Contributions: Conceptualization, Formal analysis, Investigation, Methodology, Software, Validation, Visualization, Writing - original draft*
3. Hossain, A., Knorr, G., Jokat, W., Lohmann, G., Hochmuth, K., Gierz, P., & Gohl, K. (2022). The impact of different atmospheric CO<sub>2</sub> concentrations on large scale Miocene temperature signatures. *Paleoceanography and Paleoclimatology*, in revision.
  - *Contributions: Conceptualization, Formal analysis, Investigation, Methodology, Software, Validation, Visualization, Writing - original draft*
4. Lohmann, G., Knorr, G., Hossain, A. & Stepanek, C. (2022). Effects of CO<sub>2</sub> and ocean mixing on Miocene and Pliocene temperature gradients, *Paleoceanography and Paleoclimatology*, 35(7), <https://doi.org/10.1029/2020PA003953>.
  - *Contributions: Methodology, Software, Visualization*

\*Author contribution is written according to CRediT (Contributor Roles Taxonomy; <https://casrai.org/credit/>)

